Understanding Freezing Behavior in Nano-porous Materials: Free Energy Simulation Studies and Experiment

A Dissertation

Presented to the Faculty of the Graduate School

of Cornell University

in Partial Fulfillment of the Requirements for the Degree of

Doctor of Philosophy

by

Ravi Radhakrishnan

August 2000

Understanding Freezing Behavior in Nano-porous Materials: Free Energy Simulation Studies and Experiment

Ravi Radhakrishnan, Ph.D.

Cornell University 2000

Understanding phase behavior in confined systems has a tremendous potential in improving the efficiency of a variety of separation processes that use porous materials like activated carbons, controlled glasses, silica xerogels & aerogels, carbon aerogels and zeolites. The effects of the reduced dimensionality and enhanced energetic interactions due to the porous surface have important consequences that can only be captured by molecular level modeling. Novel phase transitions can result (capillary condensation in quasi-one-dimensional systems and orientational ordering transitions in quasi-two-dimensional systems) that often are the cause of the breakdown of macroscopic equations like Kelvin and Gibbs-Thomson equations based on classical thermodynamics. In this work, the focus on a free energy method based on Landau theory which we developed and applications of this theory to understand the breakdown of the macroscopic equations, developing global phase diagrams, and characterizing hexatic phases. The results of our experimental studies are also described, that provide supporting evidence for our modeling efforts.

Biographical Sketch

Born in an academic family in southern India, I was interested in research since the days I can't even remember. I found myself (rather fortunately for me) studying chemical engineering in the Indian Institute of Technology at Madras. During my freshman year I was struck by the realization that I am no longer the know-all person in high school, that the world is full of physical (and chemical) phenomena that I hardly knew about. At the beginning of my Junior year, I started to develop an intense fascination for statistical mechanics and in my mind decided to quit chemical engineering and take up physics. It was a phase where I was imbibing the contents of many books on statistical physics, when I came across the book "Molecular Thermodynamics of Fluid Phase Equilibria" by John Prausnitz. This was a turning point for me, I decided to stick with chemical engineering. Under the tutelage of my undergraduate advisor M. S. Ananth, I became aware of the avenues of current research involving statistical mechanics in chemical engineering and towards the end of my senior year I found myself an opportunity to take up graduate studies at Cornell. I had only heard good things about the molecular modeling and condensed matter group at Cornell and decided to accept the offer. What happened in the five years hence forth is the story of my Thesis.

This work is dedicated to my father, who has been a great source of inspiration, strength and guidance.

Acknowledgements

It is more than just traditional for me to start by thanking my advisor Keith. E. Gubbins, for his invaluable guidance and support. To say the least, my association with him was fruitful beyond my satisfaction. Our intellectual discussions varied over a panorama of subjects ranging from phase transitions in confined fluids to the spiders in Australia, in a variety of places including the out-door cafes in Heidelberg, Germany and the trains in southern India. An association that I'll never forget in my life is with Malgorzata-Sliwinska Bartkowiak, under whose tutelage I picked up the necessary skills to be an experimentalist. My acknowledgments would not be complete without mentioning the critiques from the other members of my Thesis committee, Carl P. Franck and Paulette Clancy. Their timely suggestions and advice on the importance of "laboratory experience" proved to be greatly beneficial for me personally, and essential towards the completion of my Thesis. I have progressed considerably, on the aspects of academic training, maturity and independence by being involved with various other people. It is my pleasure to thank Lev Gelb, Katsumi Kaneko, Minoru Miyahara, Michael Maddox, Kendall Thomson, Prabhu Valivetti and Heath Turner for all their help and advice. This work was supported by grants from the National Science Foundation, Department of Energy, and the Maria Sklowdowska fund.

Table of Contents

List of Tables

List of Figures

Chapter 1

Introduction

Molecules confined within narrow pores, with pore widths of a few molecular diameters, can exhibit a wide range of physical behavior. The introduction of wall forces, and the competition between fluid-wall and fluid-fluid forces, can lead to interesting surface-driven phase changes. These include new kinds of phase transitions not found in the bulk phase, e.g. layering, wetting and commensurate-incommensurate transitions, as well as shifts in transitions (e.g. freezing, gas-liquid, liquid-liquid) that are familiar from bulk behavior. In such confined systems the confined phase is usually termed the *adsorbate*, and the porous material the *adsorbent*.

1.1 Porous materials

Some examples of nano-porous materials are given in Table 1.1, together with approximate pore shapes and sizes. It is convenient to divide these into those with crystalline or regular structures, and those that are amorphous. For crystalline (e.g.

Table 1.1: Nano-porous Materials [1]

Material	Surface	Pore Shape	Pore Width/nm
A. Crystalline, Regular			
Aluminosilicates	O, Al, Si	Cylinder, cage	0.3-1.0
Aluminophosphate	O, Al, P	Cylinder	0.8-1.3
MCM-41	O, Al, Si	Cylinder	1.5-10
Carbon nanotube	C	Cylinder	2-10
B. Amorphous			
Porous glass	O, Si	Cylinder	4-1$\times 10^4$
Silicas, oxides	O, Si, etc.	Cylinder	1.0 up
Silica aerogel	O, Si	Void	5-50
Pillared Clay	O, Si, Al	Slit+pillars	> 0.5
Microporous BN	B, N, H	Slit	< 1
Activated C fiber	C	Slit	0.6-1.3
Activated C aerogel	C	Slit+void	1.5-30

aluminosilicates, aluminophosphates) or regular (e.g. carbon buckytubes) materials, X-ray or neutron diffraction can be employed to determine the atomic structures, and hence the pore geometry and dimensions. Such information provides the coordinates of the solid atoms, and this structural information greatly facilitates the interpretation of experiments carried out on these materials. In addition, modeling of confinement effects in such materials is greatly simplified. Even in these materials some structural uncertainties usually remain. The location of water molecules and ions in the framework structure may be unknown. Ab initio calculations, and in some cases classical simulations, can help in determining the likely location of such molecules. In addition, defects in the lattice or pore structure can sometimes lead to large effects on adsorption, particularly if the pore structure consists of straight cylindrical pores that are not interconnected (as in some aluminosilicates and many aluminophosphates). In such cases, a very small percentage of lattice defects can block large amounts of pore volume. At the present time the small pore zeolites, conventional aluminosilicates and aluminophosphates [3], can be prepared in a highly crystalline form. The larger pore materials, MCM-41 [4] and carbon nano-tubes [5] are difficult to prepare in a pure and completely uniform state. MCM-41 (Mobil Catalyst Material 41)is a large pore aluminosilicate prepared by a liquid crystal templating process; the pore size can be controlled by varying the chain length of the liquid crystal molecules. A problem with MCM-41 is that ordered pore domains are usually very small. This situation is improved upon in a second generation of ordered mesoporous materials, prepared by a sol-gel synthesis of silicates in lyotropic liquid crystal media [6]. Such mesoporous silicas have large domains and can be extended using amphiphilic block copolymers as templates [7, 8].

Amorphous nano-porous materials vary considerably in their micro-structure and degree of regularity, and are in general very difficult to characterize completely. For example, controlled pore glass and the related Vycor glasses [9] have pore cross sections that are approximately circular, and are thought of as having roughly cylindrical pores. They are prepared by a spinodal decomposition process that involves quenching a liquid mixture of oxides into the two-liquid-phase region; the pore size is determined by the time at which the quenched mixture is kept at an intermediate temperature, before the final quench to room temperature. Such glasses have a narrow distribution of pore sizes, and have been widely used in experimental studies. The interpretation of such experimental results has often relied on models in which the pore structure is represented by a collection of straight, cylindrical, non-connected pores having a range of diameters. However, electron micrographs of these glasses show a networked structure with winding pores, and simple straight cylinder models of these materials do not capture some important confinement effects.

Silica and many porous oxides are made by sol-gel processes [10]. Silica gel is usually formed in an aqueous medium, and the solvent is subsequently removed. In the case of *xerogels*, the structure is compressed and the porosity reduced by the surface tension forces as the liquid medium is removed. *Aerogels* are gels in which the liquid phase has been replaced by a gas in such a way as to avoid the shrinkage that would normally occur if the gel were directly dried; thus, they are characterized by very high porosity. Carbon aerogels are prepared by supercritical drying, followed by pyrolysis, of an organic gel such as resorcinol-formaldehyde gel [11, 12]. They are mesoporous and may contain some micropores [13, 14]. Silica aerogels [10] can be prepared by replacing the water by alcohol, heating the gel to a temperature above the critical temperature of the alcohol (to avoid the tension associated with a

gas-liquid meniscus, and consequent compression of the gel), followed by removal of the alcohol vapor. Porous materials fabricated by sol-gel processes generally consist of roughly spherical solid particles separated by void space. Models consisting of a random array of spheres to represent the solid have been used to study such materials.

Activated carbons [15, 16, 17, 18, 19] can take a variety of forms. They are usually prepared by heating organic material (e.g. wood, coal, polymers, vegetable matter) to a high temperature in the presence of an oxidizing agent (often steam). Such carbons have been modeled using a collection of slit-shaped pores of varying widths, with the pore surfaces modeled as graphite basal planes. Variations on this include wedge shaped pores, and blocks of graphite with sections randomly removed [20, 21]. Carbon nanotubes can be prepared as regular straight carbon tubes; the diameter and number of graphite sheets in the walls can be controlled in the manufacturing process.

Experimental and theoretical work on phase transitions inside pores are beset with significant difficulties. On the experimental side, it is difficult to describe the adsorbed material, and one must attempt to infer its molecular structure from a range of experimental techniques. With the exception of the crystalline materials, one of the greatest difficulties is in determining the morphology of the material. Often the distribution of pore sizes and shapes is poorly known, and little is known of connectivity and surface chemistry. In such situations any interpretation of experimental results is speculative. In equilibrium experiments it is often difficult to know if true thermodynamic equilibrium has been achieved. Metastable states are a considerably greater problem in these systems than in bulk materials. In some cases,

such as freezing and liquid-liquid separation in amorphous materials, it is likely that equilibrium is never attained in any reasonable time. Other common difficulties in the experiments include (a) the possibility that the surfaces and pore structure may change with temperature or pressure, and (b) trace amounts of impurities in the adsorbate may preferentially adsorb on the pore walls, leading to spurious results.

In theoretical and simulation work the problems are somewhat different. In contrast to the experiments, the molecular structure of the adsorbate is completely known. However, in trying to simulate amorphous systems, the lack of knowledge of the morphology of the porous material is often the greatest problem. Two possible approaches to this problem are: (i) attempt to build a model that looks as much as possible like the real material by studying electron micrographs and other laboratory measures, (ii) try to mimic by simulation the manufacturing process used to make the real material. Other complications that arise in modeling are: (a) metastable states arise frequently, as in the experiments. However, in theory and simulation we can calculate free energies, and thus determine which of several different states of the system is the true equilibrium one, and the point at which true phase equilibrium exists. (b) Usually the pore walls are assumed to be rigid and don't change with the state conditions of the bulk fluid. This requirement can be relaxed, as in clay swelling, for example. (c) Vibration of solid atoms is usually neglected, but will be important for some properties. (d) The intermolecular potentials (fluid-fluid and fluid-solid) are uncertain. The fluid-fluid potentials are often assumed to be the same as those for the bulk fluid, i.e. the external field from the walls is assumed to have a negligible influence on these. In the case of the fluid-solid interactions, the importance of electrostatic, induction, and 3-body and higher-body interactions is often unknown. In addition to its use to model real systems, simulation and theory

can also be used to study the behavior of adsorbates confined in hypothetical porous materials that do not necessarily correspond to real materials. Such simulations offer the possibility of systematic investigations not possible in the laboratory, since the simulator can vary the pore geometry, connectivity and surface chemistry at will.

1.2 Phase behavior in confined spaces

Considerable insight into liquid-gas transitions in pores (capillary condensation, wetting and layering transitions) has been gained [22]. Important issues still remain to be resolved for solid-fluid transitions in confined systems [23]. Recently there has been growing interest in the study of fluid-solid transitions in porous materials. Improved understanding of confinement effects on freezing are essential in areas relating to lubrication, adhesion, fabrication of nanomaterials and nanotribology. In addition, these studies can provide insight into mechanisms involved in frost heaving and distribution of pollutants in soil. Freezing in porous media has also been widely employed in the characterization of porous materials using the method of thermoporometry [24].

There have been numerous experimental studies on freezing of simple fluids in silica based pores [25, 26, 27, 28, 29, 30, 31, 32, 33, 34, 35, 36, 37, 38, 39]. Freezing of oxygen in sol-gel glasses was studied by Warnock et al. [25] by a sub-pico second optical technique; the freezing temperature in the confined system was always depressed as compared to the bulk; the shift was larger for smaller pores, and as large as 10 K for the smallest (20 nm) pore. Unruh et al. [31] examined the melting behavior of indium metal in porous silica glasses by differential scanning calorime-

try (DSC) measurements, and reported a large depression in melting point due to confinement. The simplest way to understand the freezing point shift is through the Gibbs-Thomson equation. This determines the freezing temperature, T_f, as the point at which the chemical potential of the solid core inside the pore equals that of the surrounding fluid (see e.g. Evans and Marconi [40]).

$$\frac{\Delta T_f}{T_{fb}} = -2\frac{(\gamma_{ws} - \gamma_{wl})\nu}{H\lambda_{fb}} = -\frac{\Delta\phi}{\lambda_{fb}} \tag{1.1}$$

where T_{fb} is the bulk freezing temperature, γ_{ws} and γ_{wl} are the corresponding wall-solid and wall-fluid surface tensions, ν is the molar volume of the liquid, λ_{fb} is the latent heat of melting in the bulk system and $\Delta\phi$ represents the difference between the total wall-solid potential energy and the wall-solid potential energy that would exist if the wall were made up of the adsorbed solid itself. This type of classical thermodynamic argument breaks down for small pores, as the concept of surface tension is not well defined in the limit of small and highly inhomogeneous systems.

Unruh et. al. [31], Molz et. al. [30] reported latent heat measurements λ_{fp}, using DSC in the confined systems. The magnitude of λ_{fp} in the above studies was much less than the latent heat in the bulk. The difference was attributed to the premise that, in a pore the confined crystalline phase may not be homogeneous, i.e., there may be amorphous regions coexisting with crystalline regions. Such speculations can only be tested if the fluid structure of the confined phases are studied, in addition to thermodynamic properties such as freezing points and latent heats.

There have been experimental reports that investigated the structure of the confined phases through NMR and X-ray diffraction techniques. Overloop and Van Gervan [38] studied freezing of water in porous silica using NMR, and they suggest that

in the confined solid phase up to 3 molecular layers adjacent to the pore wall (which they term "bound water") have a structure that is different from the crystal phase and from that of the free liquid. The rest of the water molecules in the pore interior were in the form of cubic ice (I_c) and the freezing temperatures were consistent with the Gibbs-Thomson equation. Morishige and Nabuoka [36] used x-ray diffraction to study water in siliceous MCM-41 having a range of pore sizes, and also confirmed the existence of a disordered layer of water molecules near the pore wall, with the inner region being the I_c phase. Morishige and Kawano [37] also studied water in Vycor glass and found evidence for both the cubic I_c phase as well as the ordinary hexagonal (I_h) phase. Baker and co-workers [41] studied the nucleation of ice in sol-gel silicas and MCM-41 and found that the crystal structure depends strongly on the conditions and nature of the porous material, showing characteristics of both I_h and I_c forms. Morishige and Kawano [37] have reviewed other experimental studies of the freezing/melting behavior of water in porous silicas and glasses.

In a recent study, Booth and Strange [39] examined the melting of cyclohexane in porous silica using the NMR technique. The melting temperature was below the bulk melting point, and in the confined solid phase there were two distinct components of the transverse relaxation time. The short component (15-30 μs, comparable to the crystal phase in the bulk) was attributed to the crystal phase in the interior of the pore, and the long component was attributed to a liquid-like contact layer (the layer adjacent to the pore walls). Further lowering of temperature led to the freezing of the surface (contact) layer as well.

The effect of confinement on the triple point of CO_2 was examined by Duffy et. al. [32] using positronium annihilation spectroscopy. The authors found that the

confinement of CO_2 in Vycor glass shifts the liquid-solid transition to a considerably lower, and the gas-liquid transition to a considerably higher temperature, than in the bulk. The triple point is reduced both in pressure and temperature from that of the bulk. Recently, Morishige and Kawano [42] employed x-ray diffraction to study freezing of Kr in MCM-41 under isothermal conditions, by varying the pressure, and found that the confined triple point is not a single state point in the P-T diagram, but a region in the P-T plane. The authors attributed the diffuse triple point region for the confined system to heterogeneity of pore sizes, but speculated that the diffuse triple point region is due to coexistence of molecular clusters of different phases. Brown et. al. [43] reported studies of the microscopic structure of confined solid CO_2 adsorbed in porous Vycor glass using x-ray diffraction. Their study concluded that the confined CO_2 solidifies into crystallites, with a structure that is consistent with the *Pa3* structure (an fcc lattice with molecules oriented along the diagonals of the cubic lattice) of bulk CO_2. The average crystallite size of the solid phase of the confined CO_2 was comparable to the pore dimensions in Vycor, indicating that the solidification occurs separately in each of the pores. However, a significant amount of disorder was observed in the arrangement of the molecules which could not be accounted for with the Debye-Waller effect.

In view of this large body of experimental evidence for a decrease in the freezing temperature due to confinement, it is tempting to assume that a decrease always occurs. However, an opposing trend in the freezing point shift was reported by Klein and Kumacheva [44]. These authors studied freezing of cyclohexane between parallel mica surfaces (slit shaped geometry) and observed a significant *increase* of about 17 K in the melting temperature on confinement for a 4.0 nm pore. Similar phenomenon have been observed for linear alkanes confined between mica sur-

faces [45, 46]. Such an increase is consistent with the Gibbs-Thomson equation if one recognizes that the direction of the freezing point shift depends on whether the pore wall favors the confined solid phase or the confined fluid phase. If the wall-solid surface tension γ_{ws}, is greater than the wall-fluid surface tension γ_{wl}, then the shift $\Delta T_m = T_{m,bulk} - T_{m,pore}$ is predicted to be positive, otherwise it is negative. In a subsequent molecular simulation study of freezing of simple fluids in slit pores, Miyahara and Gubbins [47] showed that T_f was strongly affected by the strength of the attractive forces between the fluid molecules and the pore walls. For repulsive or weakly attractive potentials, T_f decreased. For strongly attracting walls such as carbons, an *increase* in T_f was observed. Moreover, the increase in T_f was predicted to be larger for slit than cylindrical pores [48]. More recently, Castro *et. al.* [49] studied freezing of methane and other liquid alkanes on a graphite substrate by incoherent elastic neutron scattering. They found that the layer nearest to the graphite substrate melts at a temperature 10% higher than the bulk melting point of methane.

The elevation in the freezing temperature in confined systems remain controversial, as has been contradicting reports on the nature of the shift in the freezing temperature of cyclohexane between parallel mica surfaces in a surface force apparatus [50]. In the simulation studies of Miyahara and Gubbins [47] and Maddox and Gubbins [48] the freezing and melting displayed large hysteresis loops in the average density of the fluid adsorbed as a function of temperature, and thus the location of the equilibrium freezing/melting point could be estimated only to the accuracy of the width of the hysteresis loops. The nature of the transition was also not clear from the adsorption behavior. The nature of the transition was unclear, and the continuous nature of the freezing curves suggested that the phase transition

could be continuous. A study of phase transitions can seldom be complete without calculating free energies.

In an attempt to address this problem, Dominguez *et al.* [51] used thermodynamic integration [52] to calculate the free energy of the solid and fluid phases in the pore. This method involves a numerical integration of the Gibbs free energy starting from a known reference phase (the Einstein crystal for the solid phase and the ideal gas for the liquid phase) to the state point of interest. For slit pores with weakly attractive walls Dominguez *et. al.* [51] were able to use thermodynamic integration to evaluate the free energy of the confined phases. They were thus able to show that the freezing transition was first order, and to locate the true equilibrium melting point. These results were consistent with that obtained by Miyahara and Gubbins [47]. The free energy study in Ref. [51] was limited to confined systems with repulsive or weakly attractive wall-fluid potentials. For the more ubiquitous case of a wall-fluid potential that is moderately or strongly attractive, this method breaks down. This is because the adsorbed molecules adjacent to the pore-wall (the contact layer) freeze before the adsorbed molecules in the interior of the pore (this issue is addressed in detain in chapters 2 & 5). This makes it impossible to find a reversible path from the ideal gas phase to the fluid phase, since any such path runs into a first order transition corresponding to the freezing of the contact layer. [1]

In order to circumvent the problems involved in the thermodynamic integration method, we have developed a novel approach involving the calculation the Landau free energy as a function of a suitable order parameter, using the grand canonical

[1] The fluid phase referred to here, is characterized by a frozen contact layer but is liquid-like in the interior of the pore.

Monte Carlo simulation method. The grand free energy for each phase can be obtained by one-dimensional integration of the Landau free energy over the order parameter. Using this approach important questions regarding melting and freezing in pores are addressed regarding the nature of the phase transition: first order vs. continuous, the direction of shift in the melting temperature T_m, nature and origin of hysteresis, dimensionality cross-over due to increasing confinement, structural changes of the condensed phases in the restricted pore geometries, effect on latent heats, etc. The focus of this thesis will be on the effects of the geometric confinement and enhanced energetic interaction due to the presence of the pore walls, on the freezing behavior of the confined fluid phase. There is a considerable shift in the phase diagram of a fluid due to confinement effects. In addition, novel phases manifest solely due to the presence of the pore walls. In the following chapters the Landau free energy methodology and several applications of freezing transitions in confined systems are described.

Chapter 2

A new free energy formalism to study freezing in slit-pores

This chapter deals molecular simulation study of freezing transitions for simple fluids in narrow slit-pores. A major stumbling block in previous studies of freezing in pores has been the lack of any method for calculating the free energy difference between the confined solid and liquid phases. Conventional thermodynamic integration methods often fail for confined systems, due to the difficulty in choosing a suitable path of integration. A novel approach involving the calculation the Landau free energy as a function of a suitable order parameter, using the grand canonical Monte Carlo simulation method is described. The grand free energy for each phase can be obtained by one-dimensional integration of the Landau free energy over the order parameter. These calculations are carried out for two types of wall-fluid interaction, a hard wall and a strongly attractive wall modeled on carbon. The grand free energy results for both cases clearly indicate a first order fluid to solid transition. In addition, the angular structure function in the individual molecular layers provide strong evidence of a transition from a two-dimensional liquid phase to a

hexatic phase. This is followed by a transition from the hexatic to a crystal phase. This chapter is organized as follows: in section 2.1, we discuss the various potential models and simulation methods and also describe the formulation of the free energy method used. Sections 2.3 & 2.4 outline the free energy calculation. We investigate the quasi-two-dimensional nature of the fluid phase in the case of a graphite pore in section 2.5. Finally in section 2.6, we point out some areas for future work along with our conclusions.

2.1 Simulation methodology

The interaction between the adsorbed fluid molecules is modeled using the Lennard-Jones (12,6) potential with size and energy parameters chosen to describe methane. Two types of pores, (1) a purely repulsive and smooth hard wall pore, and (2) a graphite pore, are chosen to study the effect of a purely repulsive and a highly attractive fluid-wall potential on the freezing point of methane.

Our model of the repulsive pore is characterized by a pore width H, which is defined to be the distance between the planes through the nuclei of the atoms in the first atomic layer of each of the opposing walls. The repulsive wall can be thought of as being composed of a continuum of hard sphere atoms. The hard sphere diameter in our model is chosen to be the same as the Lennard-Jones size parameter, $\sigma_{fw} = 0.361$ nm, that characterizes the methane-graphite interaction. To model the graphite pore, we use the integrated 10-4-3 Steele potential [53, 54] given by,

$$\phi_{fw}(z) = 2\pi\rho_w\epsilon_{fw}\sigma_{fw}^2\Delta\left[\frac{2}{5}\left(\frac{\sigma_{fw}}{z}\right)^{10} - \left(\frac{\sigma_{fw}}{z}\right)^{4} - \left(\frac{\sigma_{fw}^4}{3\Delta(z+0.61\Delta)^3}\right)\right] \qquad (2.1)$$

The potential parameters for methane and for the graphite wall were taken from Steele [53, 54],

$$\sigma_{ff} = 0.381 \text{ nm}, \qquad \epsilon_{ff}/k_B = 148.1 \text{ K}$$
$$\sigma_{ww} = 0.340 \text{ nm}, \qquad \epsilon_{ww}/k_B = 28.0 \text{ K}$$
$$\rho_w = 114 \text{ nm}^{-3}, \qquad \Delta = 0.335 \text{ nm}$$
$$\sigma_{fw} = (\sigma_{ff} + \sigma_{ww})/2, \quad \epsilon_{fw} = (\epsilon_{ff}\epsilon_{ww})^{1/2}$$

Here, the σ's and ϵ's are the size and energy parameters in the Lennard-Jones (LJ) potential, the subscripts f and w denote fluid and wall respectively, z is the coordinate perpendicular to the pore walls and k_B is the Boltzmann's constant. For a given pore width H, the total potential energy from both walls is given by,

$$\phi_{pore}(z) = \phi_{fw}(z) + \phi_{fw}(H - z) \tag{2.2}$$

We expect the approximation of a structureless graphite wall to be a good one here, since the diameter of the LJ molecule (0.381 nm) is much larger than the C-C bond length in graphite (0.14 nm), so that methane molecules only feel a mild corrugation in the fluid-wall potential in passing along the surface. This has been confirmed by simulations of monolayers of methane on structured, planar carbon walls [55], where wall structure had only a minor effect for temperatures down to 60 K. This argument was further tested in Ref. [47], where it was found that the structure of methane was practically identical when confined between smooth and structured graphite pore walls, for both the fluid as well as the solid phase.

The simulation runs were all performed in the grand canonical ensemble as described in Ref. [56], fixing the chemical potential μ, the volume V of the pore and the temperature T. The pore width in the simulation was typically around $7.5\sigma_{ff}$,

and the rectilinear simulation cell was $10\sigma_{ff}$ by $10\sigma_{ff}$ in the plane parallel to the pore walls, consistent with a cutoff of $5\sigma_{ff}$ for the fluid-fluid interaction. The system typically had up to 700 particles, and periodic boundary conditions were employed in the plane parallel to the pore walls. The simulation was setup such that insertion, deletion and displacement moves were attempted with equal probability, and the displacement step was adjusted to have a 50% probability of acceptance. Thermodynamic properties were averaged over 40-100 million individual Monte Carlo steps. The length of the simulation was adjusted such that a minimum of ten times the average number of particles in the system would be inserted and deleted during a single simulation run.

2.1.1 The Landau free energy formalism

In the Landau theory of phase transitions [57, 58], the model system is characterized by an order parameter Φ, which is generically a density variable that takes on distinct values in different phases of the system. The behavior of Φ as a function of the state variables in the thermodynamic limit determines the nature of the phase transition. In particular, the probability $P[\Phi]$ of observing the system having an order parameter value between Φ and $\Phi + \delta\Phi$ assumes a bi-modal distribution when there is two-phase coexistence. As the state conditions are varied, the relative behavior of the two peaks with respect to each other provides information on which phase is more stable in the thermodynamic sense. The probability distribution function $P[\Phi]$ is calculated during a simulation run by collecting statistics of the number of occurrences of a particular value of Φ in the form of a histogram. For the general case of a spatially varying order parameter $\Phi(\vec{x})$, the probability $P[\tilde{\Phi}]$

is defined as,

$$P[\tilde{\Phi}] \;=\; \frac{1}{\Xi}\sum_{N=1}^{\infty}\frac{\exp\left(\beta\mu N\right)}{N!\lambda^{3N}}\int D_N[\Phi(\vec{x})]\,\delta(\tilde{\Phi}-\Phi)\,\exp(-\beta H_N) \tag{2.3}$$

Ξ is the partition function in the grand canonical ensemble, N the number of molecules in the system, $\beta = 1/k_BT$, λ is the de Broglie wavelength and H_N is the Hamiltonian of the system. The path integral notation $D_N[\Phi(\tilde{\vec{x}})]$ should be interpreted as [58],

$$\int D_N[\Phi(\vec{x})] \;\equiv\; \lim_{v_o\to 0}\,\Pi_\alpha \int d\Phi_\alpha \;=\; \int_{\vec{r}^N} d\vec{r}^N \tag{2.4}$$

Equation (2.4) defines the path integral in terms of a trace over a discrete number of sites α, and v_o represents the volume per site. The Landau free energy $\Lambda[\tilde{\Phi}]$ is then defined as,

$$\exp(-\beta\Lambda[\tilde{\Phi}) \;=\; \sum_{N=1}^{\infty}\frac{\exp\left(\beta\mu N\right)}{N!\lambda^{3N}}\int D_N[\Phi(\vec{x})]\,\delta(\tilde{\Phi}-\Phi)\,\exp(-\beta H_N) \tag{2.5}$$

and can be interpreted as the free energy corresponding to a restricted partition function in order parameter space. From this definition it follows that,

$$\Lambda[\Phi] \;=\; -k_BT\,\ln(P[\Phi]) \;+\; Constant \tag{2.6}$$

For a particular phase, for instance phase A, the grand free energy Ω_A is related to the Landau free energy by

$$\exp(-\beta\Omega_A) \;=\; \int_{\Phi_{min,A}}^{\Phi_{max,A}} d\Phi\,\exp(-\beta\Lambda[\Phi]) \tag{2.7}$$

The grand free energy at a particular temperature can be calculated by numerically integrating over the order parameter range $(\Phi_{min,A}, \Phi_{max,A})$ that corresponds to the particular phase A in consideration. More complete details of the method for confined systems are given elsewhere. [59, 60]

2.1.2 Umbrella sampling

To overcome the difficulty of collecting reliable statistics on the probability distribution function we used umbrella sampling [61]. To calculate $P[\Phi]$, the order parameter space is divided into ten windows. As a first estimate, an approximate probability distribution $P_1[\Phi]$ was calculated separately in each of the windows, by collecting statistics in the form of a histogram in Φ without the use of any weighting function in the umbrella sampling. A successive set of simulations were then performed in each of the windows by using a weighting function $w\{\Phi\} = (P_1[\Phi])^{-1}$, in addition to the usual acceptance criteria for the probabilities in the GCMC simulation [60].

This process can be interpreted as performing the simulation in a new ensemble, $\Psi(T, V, \mu, h)$, which is related to the Λ-ensemble $\Lambda(T, V, \mu, \Phi)$, by the Legendre transformation

$$\Psi(T, V, \mu, h) = \Lambda(T, V, \mu, \Phi) - h\Phi \tag{2.8}$$

where the term $-h\Phi \equiv w\{\Phi\}$ is the weighting function in the umbrella sampling. Thus, using the weighting function in the acceptance criteria of the GCMC simulation is like applying an external field h that is conjugate to the order parameter Φ. At the coexistence condition, it is this field that forces the system to move from one stable minimum to the other. For this method to work successfully, it is important to choose an appropriate order parameter Φ which responds to changes in h; Φ should act as a conjugate variable to h [60]. It is equally important to ensure that the choice of $w\{\Phi\}$ causes the regions of Φ that are thermodynamically unstable in the Λ-ensemble, to be thermodynamically stable in the Ψ-ensemble. These two conditions ensure ergodicity and the collection of reliable statistics, respectively. The Landau free energy $\Lambda[\Phi]$ is recovered from the Ψ-ensemble using equation (2.8).

2.2 Order parameter

In order to study solid-liquid phase transitions, the order parameter should be sensitive to the degree of crystalline order in the system. We followed the previous work on bulk fluids [60, 59] in using an order parameter that measures the orientational order (a measure of the rotational symmetry of the crystal). Our calculations of the adsorption vs. temperature, and of the radial distribution function, showed that the behavior of methane was qualitatively different in the hard wall pore and in the graphite pore. We used these results as a basis to choose a suitable order parameter.

2.2.1 Hard wall pore

The adsorption curve and the three-dimensional pair correlation functions were calculated for methane confined in a hard wall pore of width $7.5\sigma_{ff}$ using standard GCMC simulations. The chemical potential was maintained at a value corresponding to a pressure of 100 atm.; a LJ equation of state from the literature [62] was used to relate the chemical potential to the pressure. This high pressure is necessary to study hard wall systems because the methane would evaporate inside such pores under normal pressures [47]. These results indicated that the structure of the fluid and solid phases were similar to the bulk three-dimensional structure, but the transition itself was occurring at a much lower temperature than for bulk methane; the freezing of Lennard-Jones methane in the bulk occurs at $T = 101K$ [63],[64]. Thus, three dimensional bond orientational order parameters introduced by Steinhardt *et al.* [65] (see also Refs. [59, 60]) are employed. These order parameters are defined as follows: each nearest neighbor bond has a particular orientation in space with respect to a reference axis, which can be described by the spherical coordinates (θ, ϕ). Nearest neighbors were identified as those particles that were less than a cut-

off distance r_{nn} away from a given particle. We used a cutoff distance $r_{nn} = 1.3\ \sigma_{ff}$, corresponding to the first minimum of $g(r)$ in a fcc crystal at bulk coexistence [1]. One can then define the global order parameter $\overline{Q}_{lm}$ [66],

$$\overline{Q}_{lm} \ = \ \frac{1}{N_b} \sum_{i=1}^{N_b} Y_{lm}(\theta_i, \phi_i) \tag{2.9}$$

where the index i runs over the total number of nearest neighbor bonds N_b and the Y_{lm}'s denote the spherical harmonics. In order that the order parameter does not depend on the overall orientation of the crystal in the simulation cell, rotationally isotropic combinations of the $\overline{Q}_{lm}$'s are defined as [66],

$$Q_l \ \equiv \ \left(\frac{4\pi}{2l+1} \sum_{m=-l}^{+l} \left| \overline{Q}_{lm} \right|^2 \right)^{1/2} \tag{2.10}$$

and,

$$W_l \ = \ \frac{1}{\left(\sum_m \left| \overline{Q}_{lm} \right|^2 \right)^{3/2}} \sum_{m_1, m_2} \begin{pmatrix} l & l & l \\ m_1 & m_2 & -m_1 - m_2 \end{pmatrix} \overline{Q}_{lm_1} \overline{Q}_{lm_2} \overline{Q}_{l(-m_1-m_2)} \tag{2.11}$$

The matrix in equation (2.11) is a representation of the Wigner $3J$ symbols defined in Ref. [67]. The value of the order parameters for some common crystal types are given in Table 2.1. From the positions of the first five peaks in the pair correlation function of the solid phase (at $r/\sigma_{ff} = 1, \sqrt{2}, \sqrt{3}, 2, \& \sqrt{5}$), it was evident that the crystal structure could either be a simple cubic lattice or a face centered cubic lattice. The calculation of the order parameters showed that,

$$Q_6 = 0.505, \qquad Q_4 = 0.159$$

$$W_6 = -0.0128, \quad W_4 = -0.151,$$

[1] We note that the Landau free energy formalism is independent of any arbitrariness involved in the definition of the order parameter such as choosing of the nearest neighbor cutoff distance r_{nn}.

Table 2.1: Bond orientational order parameters in 3-d crystals

Crystal	Q_4	Q_6	W_4	W_6	$\Phi = Q_6 - 3W_4$
f.c.c.	0.191	0.571	-0.159	-0.013	1.052
h.c.p.	0.097	0.485	0.134	-0.012	0.082
b.c.c.	0.036	0.511	0.159	0.013	0.033
s.c.	0.764	0.354	0.159	0.013	-0.124
Icosahedral	0	0.663	0	-0.170	0.663
Liquid	0	0	0	0	0

confirming that the crystal structure was a face centered cubic lattice. We therefore followed Lyndenbell *et. al.* [60], and used the combination $\Phi = Q_6 - 3W_4$ as the order parameter for the Landau free energy calculation. The quantity Q_6 alone is a good order parameter in terms of being able to distinguish the fluid phase from a solid phase, but it is the quantity Φ that responds to the external field in the umbrella sampling method.

2.2.2 Graphite pore

For methane adsorbed in the graphite pore ($H = 7.5\sigma_{ff}$), the adsorption curve was calculated along a path such that, for each temperature, the value of the chemical potential corresponded to the pressure at which there is two-phase (gas-liquid for temperatures above the triple point and gas-solid line below the triple point) coexistence in the bulk fluid [63],[64]. This path was chosen so that our calculations could be verified in a real experiment, without having to depend on an accurate LJ equation of state [47]. In figure 2.1 the density profile along the z direction (the direction

perpendicular to the pore walls) is shown. In contrast to the behavior for hard wall confinement, distinct layering occurs for the whole range of temperatures for which freezing and melting occur. The order in each of the individual layers is studied by calculating the in-plane, two-dimensional pair correlation functions within each layer (see figure 2.2). The plots in figure 2.2(b) indicate that the contact layers (the two layers adjacent to the pore walls) freeze at a temperature higher than the rest of the layers. The large value (about 4.5) of the first peak in $g(r)$ for the contact layer, a first minimum of zero, and the split second and third peaks, all show evidence of a solid phase in this layer. These results are consistent with those obtained by Miyahara and Gubbins [47] and by Dominguez *et al.* [51] for similar systems. Miyahara and Gubbins also verified the Hansen-Verlet criterion [68] for freezing by calculating the structure factor. This criterion is based on the value of the first peak in the structure factor, $S(k_o)$, and states that in the solid phase $S(k_o) \geq 2.7$ in three dimensions and $S(k_o) \geq 4.4$ in two dimensions. In order to capture the layer-by-layer freezing behavior, we chose to use a two-dimensional order parameter previously introduced by Mermin [69, 70],

$$\Phi_j = \left| \frac{1}{N_b} \sum_{i=1}^{N_b} \exp(i6\theta_i) \right| = \left| \langle \exp(i6\theta_i) \rangle_j \right| \tag{2.12}$$

Φ_j measures the hexagonal crystalline bond order within each layer j. The overall order parameter Φ is an average of the hexagonal order in all the layers.

$$\Phi = \left(\sum_{j=1}^{N_{layers}} \Phi_j \right) / N_{layers} \tag{2.13}$$

For molecules with isotropic interaction potential the only two-dimensional closed packed structure is the hexagonal crystal. The quantity Φ is invariant under rotation about the z axis. We expect $\Phi = 0$ when all the layers have the structure of a two-dimensional liquid (figure 2.2(a)), $\Phi = 1$ in the solid phase (figure 2.2(c)) and

$0 < \Phi < 1$ for the phase in figure 2.2(b).

2.3 Results for the hard wall pore

The variation of adsorption with temperature for LJ methane confined in the hard wall pore of width $H = 7.5\sigma_{ff}$ indicated that freezing occurred at a temperature $T \simeq 40K$, and melting occurred at a temperature $T \simeq 80K$. Thus, a pronounced hysteresis loop occurs, spanning about $40K$. The Landau free energy, $\Lambda[\Phi]$, is shown in figure 2.3 for two different temperatures, $T = 60K$ and $T = 45K$; it has a double well structure, with the broad minimum centered around $\Phi = 0$ corresponding to the liquid phase and the second minimum centered around $\Phi = 0.95$ corresponding to the face centered cubic solid phase (ideally, $\Phi_{fcc} = 1.052$). The high temperature curve shows the liquid phase to be more stable, while the low temperature curve shows the crystal phase to be the most stable. The Landau free energy curves in figure 2.3 are determined up to an arbitrary constant. The grand free energy for each phase is calculated from the Landau free energy using equation (2.7), by evaluating the integral numerically over the order parameter range characterizing the particular phase. This calculation determines the relative free energy difference between the liquid and solid phases at a particular temperature. To relate the grand free energy of a particular phase at two different temperatures, we numerically integrate

$$\left[\frac{\partial\Omega}{\partial\mu}\right]_{T,V} = -N \tag{2.14}$$

to obtain Ω as a function of μ at constant temperature, and

$$\left[\frac{\partial(\Omega/T)}{\partial(1/T)}\right]_{\mu,V,A} = U - N\mu \tag{2.15}$$

to obtain Ω as a function of T at constant chemical potential. In equation (2.15), U is the total internal energy of the system. A suitable reversible path of integration can

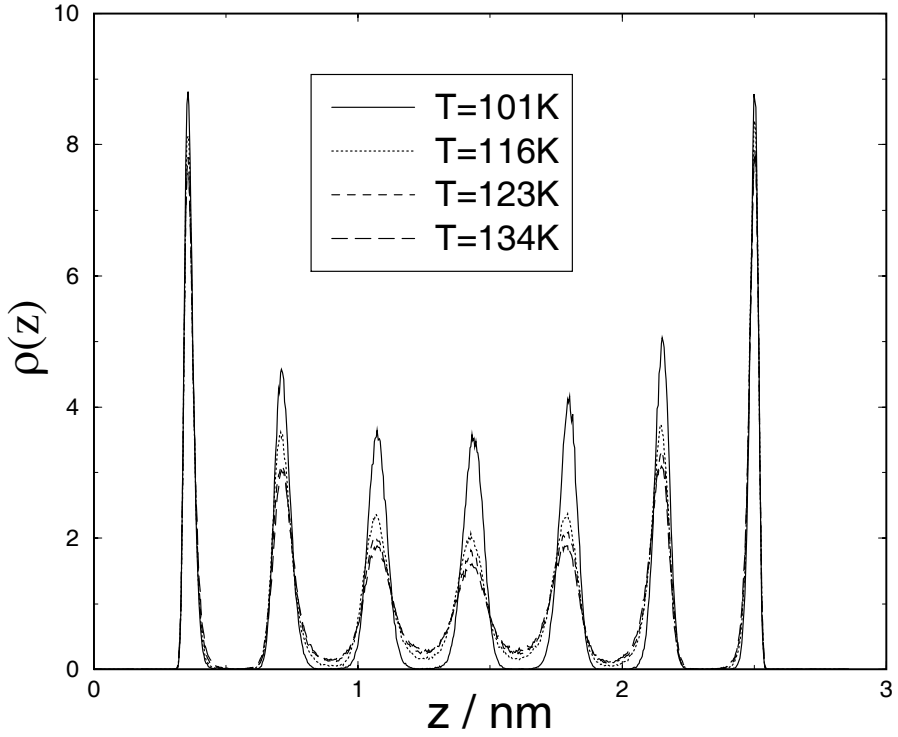

Figure 2.1: Density profile of methane in the graphite pore along the direction perpendicular to the pore walls for four different temperatures showing distinct layering. The solid curve for $T = 101K$ is for the crystalline methane and is not symmetric about the center of the pore along the z axis because of defects in the two-dimensional crystal phase in the second and third layers. The profiles for the other temperatures correspond to a fluid phase and are symmetric.

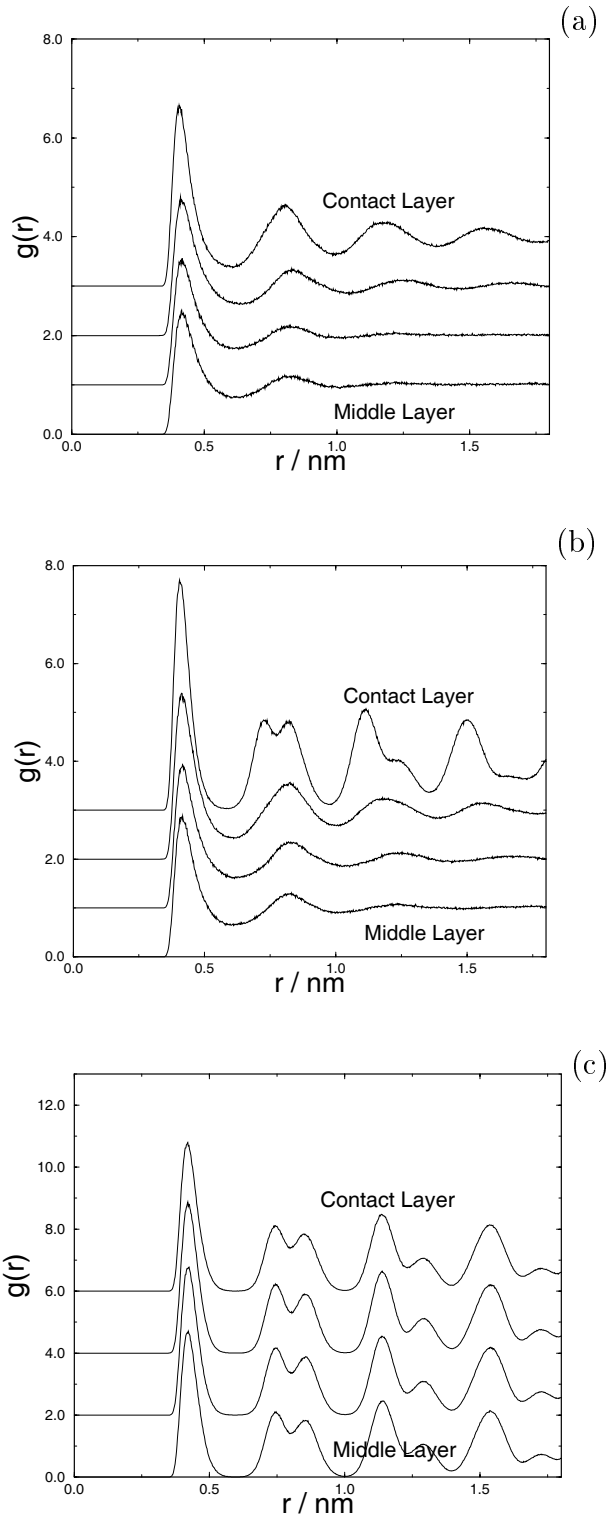

Figure 2.2: The two-dimensional, in-plane pair correlation function for each of the layers for the $H = 7.5\sigma_{ff}$ graphite pore: (a) $T = 130K$, corresponding to Phase A, (b) at $T = 123K$, corresponding to Phase B, (c) at $T = 101K$ corresponding to Phase C.

always be chosen either along the melting or the freezing branch of the adsorption curve. The grand free energy for the liquid and the crystal phase as a function of temperature is shown in figure 2.4. The crossover of the liquid and solid branches at different slopes clearly establishes the transition as first order, and also determines the transition point at $T = 48K$, which should be compared to the bulk transition of $T = 101K$ for LJ methane. The free energy surface formed by the locus of points representing the stable thermodynamic phase is convex upwards, as required by the thermodynamic stability criterion (e.g. [71]). The free energy calculation in figure 2.4 is consistent with that obtained by Dominguez *et al.* [51] for the hard wall case using the method of Frenkel and Ladd [52], and is presented here just to establish the validity of the Landau free energy method, before applying it to the more interesting case of confinement in an attractive fluid-wall potential.

We note that the true equilibrium freezing temperature of 48 K is lower than that inferred for a system of $H = 7.5\ \sigma_{ff}$ from the work of Miyahara and Gubbins [47]; in that work a sharp rise in the density of the confined material occurred at about 70 K, on cooling. However, we note that the *effective* pore width for the present system is less than that used in [47], since the hard sphere diameter of the wall molecules was chosen to be σ_{fw} of methane-carbon interaction in our study, whereas in [47] it was $0.84\sigma_{fw}$. Thus the effective pore width, $W = H - \sigma_{fw}$ in the present work, is less than that of Ref. [47] by $0.32\ \sigma_{fw}$. This decrease in W is believed to be responsible for the difference in freezing temperatures.

2.4 Results for the graphite pore

The Landau free energy as a function of the average hexagonal bond order Φ as defined in equations (2.12,2.13) is shown in figure 2.5 for four different temperatures

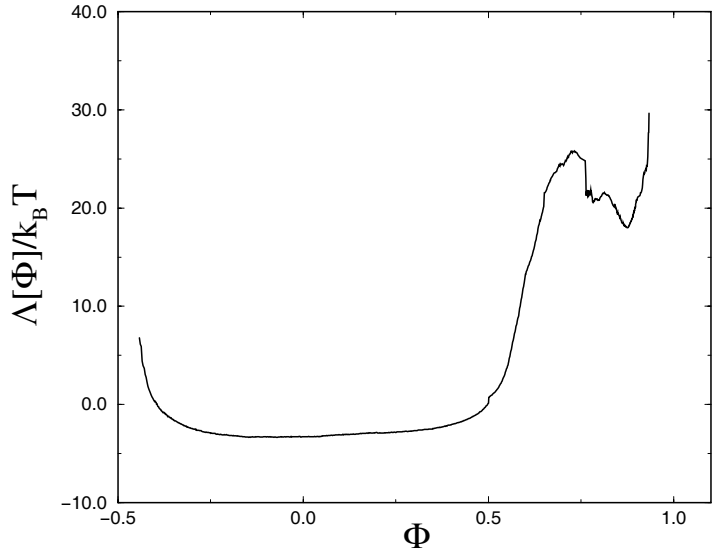

(a)

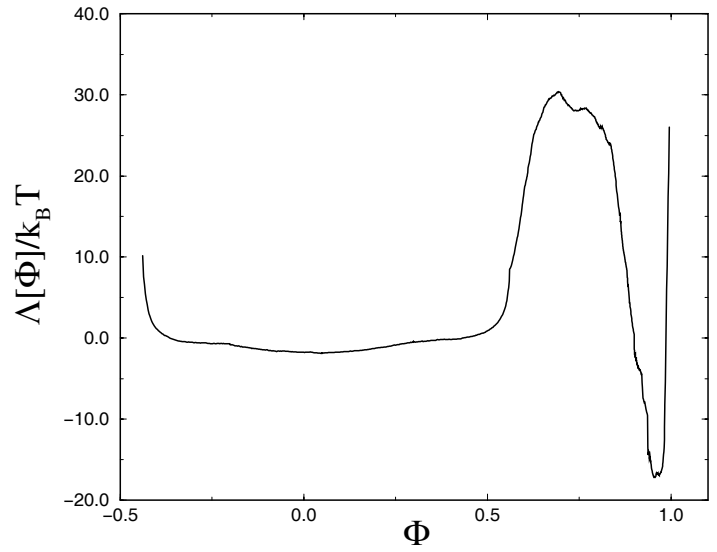

(b)

Figure 2.3: The Landau free energy as a function of the order parameter $\Phi = Q_6 - 3W_4$ for methane confined in a hard wall pore of $H = 7.5\sigma_{ff}$ at (a)$T = 60K$ and (b) $T = 45K$.

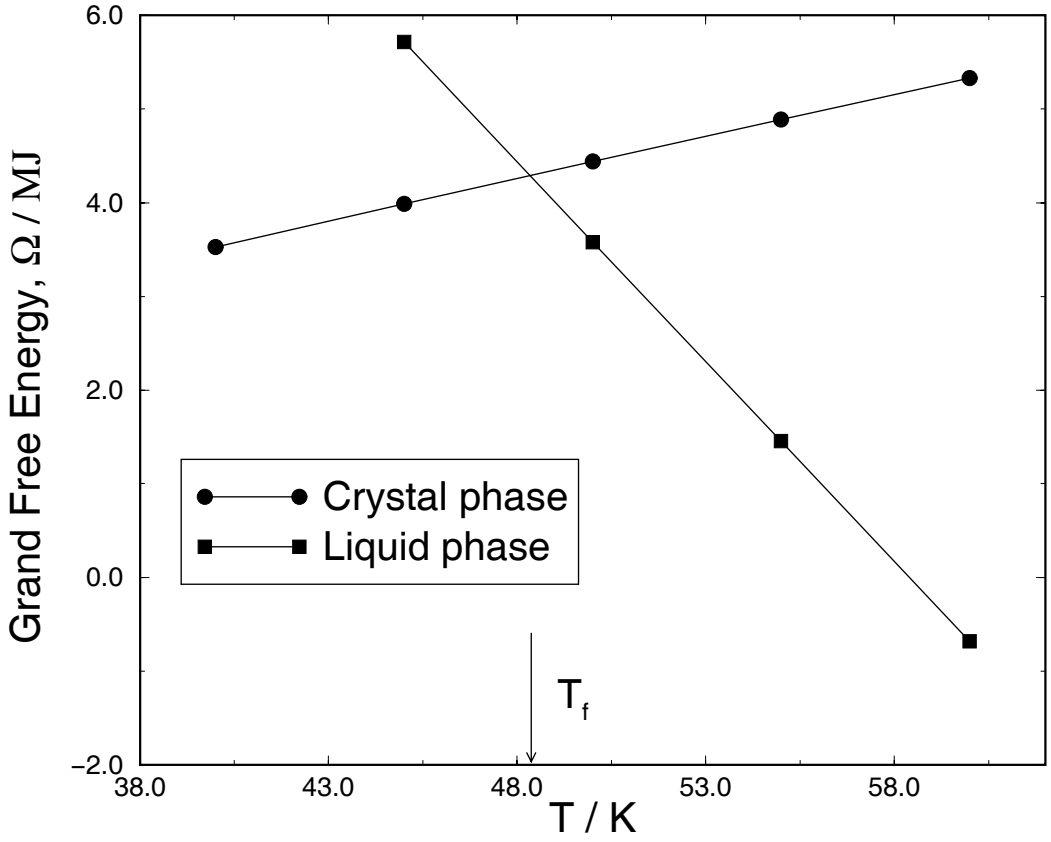

Figure 2.4: The grand free energy of the liquid and the crystal phases as a function of temperature for the hard wall system. The cross over point near $T_f = 48K$ determines the thermodynamic transition temperature.

Table 2.2: Thermodynamic stability of phases

Most stable phase	Temperature range
Phase A	$T \geq 124K$
Phase B	$114K \leq T \leq 124K$
Phase C	$T \leq 114K$

for methane confined in the graphite pore of pore width $7.5\sigma_{ff}$. Unlike the hard wall confinement case (or the bulk behavior), this system is characterized by three phases A, B and C corresponding to the three minima in figure 2.5. The structure of the three phases has already been shown in figure 2.2. In phase A, all the layers have an isotropic liquid-like structure; phase B is characterized by frozen contact layers, with the rest of the layers having an isotropic structure; and in Phase C, all the layers are frozen. The relative stability of the three phases as a function of temperature can be pictured qualitatively from the positions of the minima in the Landau free energy curves. The freezing point of the contact layers and that of the inner layers were determined exactly by calculating the grand free energy, which depends on the positions as well as the width of each minimum. This calculation is depicted in figure 2.6 for the three phases A, B and C. The plot indicates two first order transitions, one at $T = 124K$ corresponding to the freezing of the contact layers and the other at $T = 114K$ corresponding to the freezing point of the inner layers (see Table 2.2).

The equilibrium freezing temperature found here, 114 K, is somewhat lower than the freezing temperature of 118 K found in Ref. [47] by observing the rise in adsorbate density as the system is cooled. Although the model and pore width used in the two cases are identical, we note that in [47] the ideal gas equation of state

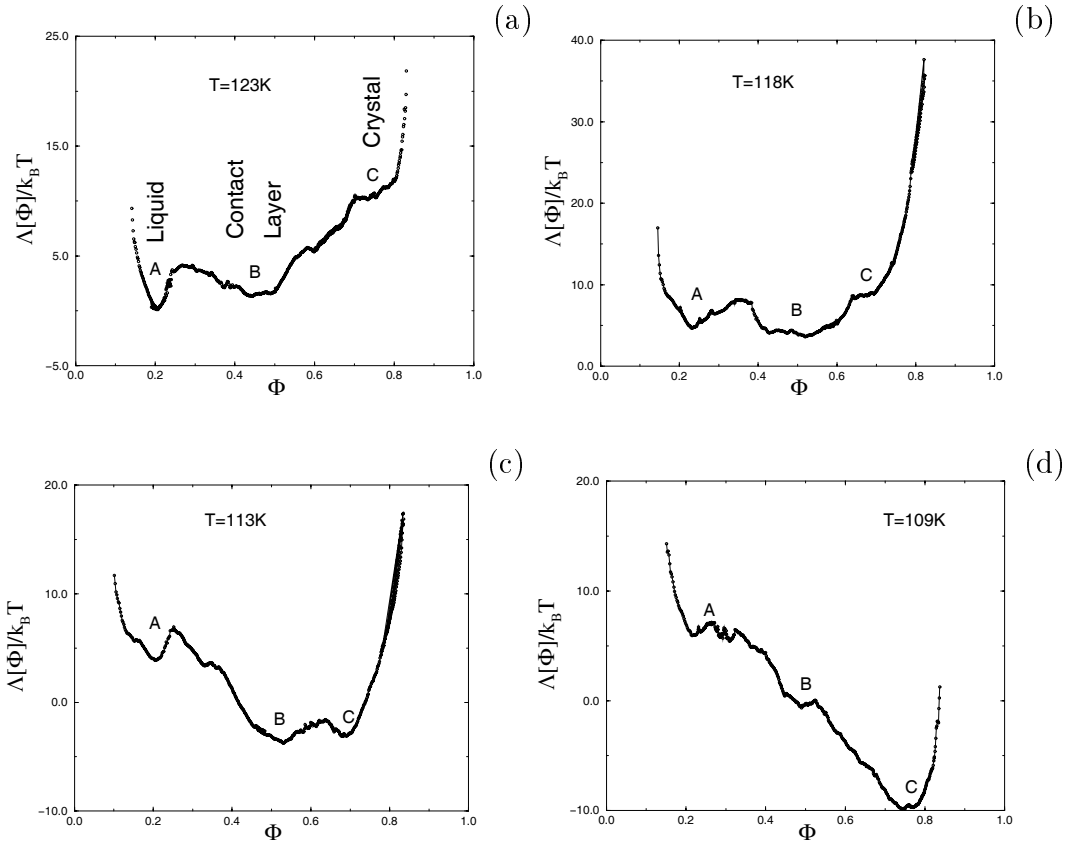

Figure 2.5: The Landau free energy as a function of the order parameter, for methane confined in a graphite pore of pore width $7.5\sigma_{ff}$ at (a) $T = 123K$, (b) $T = 118K$, (c) $T = 113K$, (d) $T = 109K$.

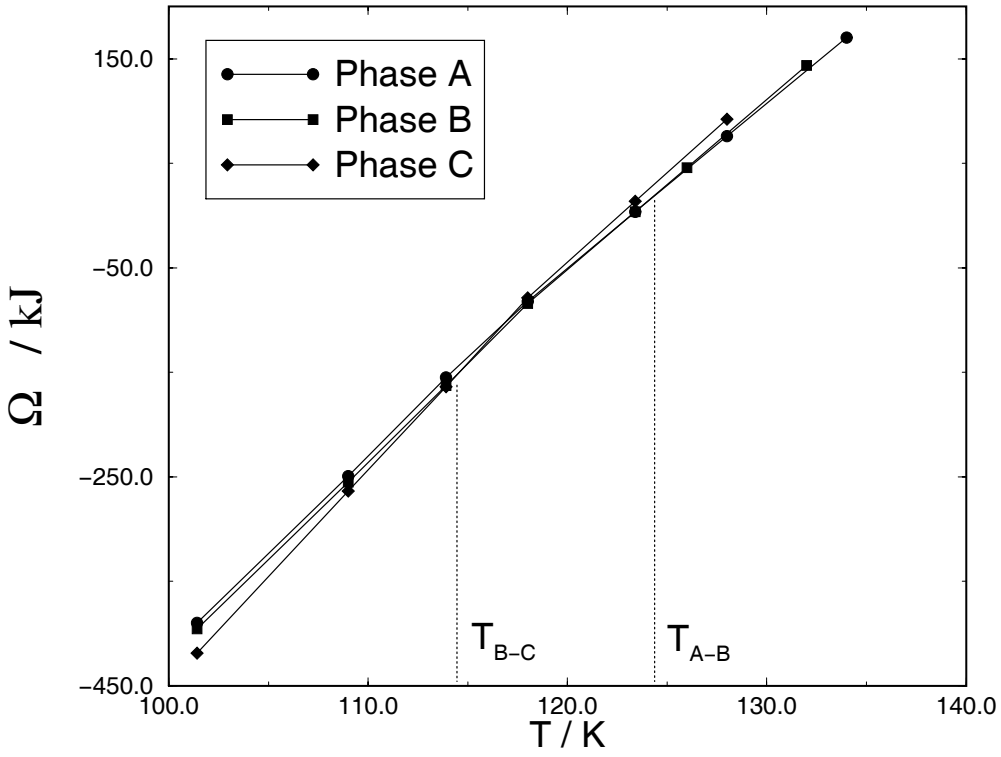

Figure 2.6: The grand free energy of the three phases A, B and C, as a function of temperature for the graphite pore. The cross over points $T_{A\text{-}B}$ and $T_{B\text{-}C}$ correspond to the two first order phase transitions.

was used to relate the chemical potential and pressure of the coexisting bulk gas. In the present case, the virial equation of state was used instead; this modification yielded chemical potentials that were up to 10 % different from the ideal gas values. Although the difference is small, we note that, because of the small difference in the slope of the grand free energy vs. T curves shown in figure 2.6 for the three phases, such a change can affect the calculated melting/freezing temperature significantly. Thus, we believe the freezing temperature determined here is more accurate than that inferred in Ref. [47].

As far as we are aware, this is the first calculation of the free energies and the thermodynamic freezing points in confined systems with a generic fluid-wall po-

tential. Comparing the grand free energy results for the hard wall pore and the graphite pore (figure 2.4 and figure 2.6), we conclude that the freezing transition in the graphite pore case is a weak first order transition, as compared to the strong transition in the hard pore case. This is indicated by the magnitude of the discontinuity in the slope of the free energy curve at the transition point, which is a measure of the first order jump in the heat capacity. The nature of the fluid phases A and B, and the reason for the freezing transition being weakly first order, are discussed in section 2.5.

2.5 Quasi-two-dimensional behavior

Care is needed in interpreting the isotropic two-dimensional pair correlation functions corresponding to all the layers in figure 2.2(a) and the inner layers in figure 2.2(b). Although the plots of the isotropic pair correlation functions are reminiscent of those of a two-dimensional liquid, a closer look at the third peaks of the $g(r)$ functions in figure 2.2(a) reveals that the contact and the second layers have extended positional correlations compared to the inner layers. Secondly, the value taken by the order parameter Φ in phase A is about 0.24 (figure 2.5) as compared to the expected value close to zero if all the layers were liquid. Similarly the value of Φ in phase B is 0.5, which is much larger than the expected value of 2/7 if the contact layers are frozen ($\Phi_1 = \Phi_7 = 1$), and the inner layers are assumed to to have the structure of a liquid ($\Phi_i = 0$, $i = 2\,\text{to}\,6$). Such intermediate values for Φ suggest the occurrence of an intermediate phase with bond-orientational order.

Two-dimensional systems have a special significance for phase transitions in which continuous symmetry is broken (such as freezing transitions). The Mermin-Wagner

theorem [72] states that long range order (LRO) cannot exist in such systems. The two-dimensional XY model of spins falls into this category, and Kosterlitz and Thouless [73] showed that there can still be a continuous phase transition from the disordered phase (where the two point correlation function decays exponentially) to a quasi-long range ordered (QLRO) phase (where the two point correlation function decays algebraically). The QLRO phase is characterized by bound pairs of vortices (topological defects) with opposite sense. The Kosterlitz-Thouless (KT) transition describes the unbinding of a dilute gas of vortex-pairs through a renormalization-group treatment. The existence of the isolated vortex spin states causes the system to be disordered. The KT transition is accompanied by a non-universal peak in the specific heat above the transition temperature, associated with the entropy liberated by the unbinding of the vortex pairs.

Halperin and Nelson proposed a mechanism for melting of a crystal in two dimensions [70] which involved two KT-like transitions. The first is a transition between the crystal phase (having positional QLRO and orientational LRO) and a hexatic phase (having positional disorder and orientational QLRO); the second transition is between the hexatic phase and the liquid phase (having positional and orientational disorder). The crystal to hexatic transition occurs through the unbinding of dislocation pairs, and the hexatic to liquid transition involves the unbinding of disclination pairs. In two dimensions, the only close packed structure for circular disks with isotropic interaction is the hexagonal lattice. A disclination is then characterized by a local configuration in which a molecule has five or seven nearest neighbors instead of the usual six. A disclination pair is a bound state of a five and a seven nearest neighbor configuration. A dislocation can be viewed as a pair of disclination pairs. A complete review of the mechanism of two dimensional melting is given in Ref. [74].

The hexatic phase was first observed experimentally in liquid crystals. In between the smectic-A phase and the crystal-B phase, a hex-B phase exists that possesses long range orientational order. This was detected in an electron diffraction experiment on liquid crystalline thin films [75], in which the intensity pattern displayed a sixfold symmetry of diffuse spots indicating positional disorder but long range orientational order. The intensity pattern for a smectic-A phase is a uniform ring and that of the crystal-B phase has six Bragg peaks corresponding to a two-dimensional hexagonal lattice. These layered liquid-crystalline systems are quasi-two-dimensional because of the additional interaction of molecules between layers. It is believed that this inter-layer interaction causes the crystal phase to have true long range positional and orientational order, and the hexatic phase to have true long range orientational order (and positional QLRO), and therefore the hexatic to crystal transition is first order, unlike the strictly two-dimensional case [76]. The nature of layer by layer freezing in a free standing film of smectic-A phase with four molecular layers was investigated by Chao *et al.* [77]. The transitions were probed using heat capacity and shear modulus measurements as well as electron diffraction patterns. Specific heat peaks were observed for the liquid-hexatic transitions but not for the hexatic-crystal transitions because most of the entropy change occurs in the former transition. However the shear modulus increased from zero continuously as the hexatic-crystal transition occurred. These measurements, together with the diffraction patterns, revealed that both the liquid-hexatic and the hexatic-crystal transitions in the two edge layers occurred at higher temperatures compared to those in the two inner layers.

The spontaneous ordering of the adsorbed molecules in the graphite pore into distinct two-dimensional layers (figure 2.1) is analogous to the structure of a smectic-A

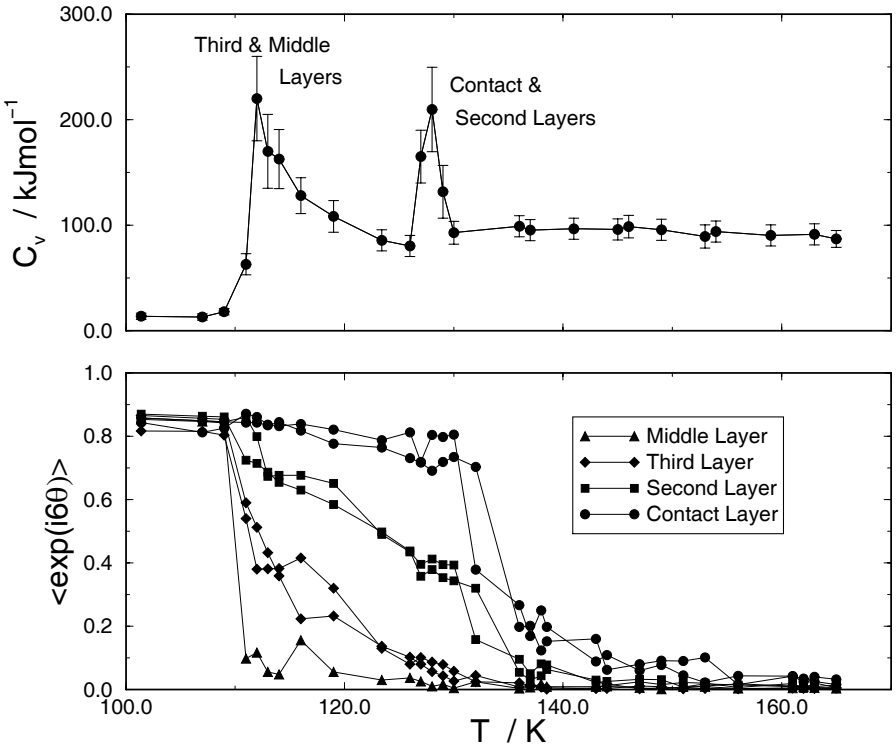

Figure 2.7: Heat capacity of the whole system and the order parameter in the individual layers as a function of temperature as the system is cooled, for the graphite pore. These plots are not expected to be reversible during the heating sequence because of strong hysteresis effects.

phase in liquid crystals. Thus the nature of the freezing transitions in the individual layers of methane can be studied along the same lines as freezing in the free standing liquid crystalline films. In figure 2.7 we show the heat capacity of the whole system and the order parameter in the individual layers as a function of temperature as the system is cooled. The i^{th} layer is a liquid for the range of temperatures for which $\Phi_i = 0$ and is a solid when $\Phi_i \simeq 0.85$. The first peak in the specific heat that occurs close to $T = 127K$ indicates a liquid to hexatic phase transition in the contact and second layers, as seen from the continuous increase in the order parameter value in these layers. Similarly, the second peak in the specific heat at $T = 114K$ indicates a liquid to hexatic transition in the third and the middle layers. The hexatic to crystal transition is expected to produce a discontinuity in the specific heat, which is probably too small to be seen in figure 2.7 for the same reason as in the case of the liquid crystalline film [77]. The structure factor $I(k_x, k_y)$ (equivalent to the intensity pattern in the electron diffraction experiment) was also calculated to support the interpretation of the above trends. Figure 2.8 shows the in plane structure factor for the contact and the third layers at four different temperatures. The intensity patterns in the form of a uniform ring suggests a liquid structure at $T = 160K$. The structure factor at $T = 128K$ (figure 2.8(b)) shows a six fold symmetry in the intensity pattern in the contact layers supporting the onset of the hexatic transition in the contact layer, as indicated by the specific heat peak at that temperature. The third and the middle layers however, have the intensity pattern of a liquid (figure 2.9(b)). The structure at $T = 111K$ (figures 2.8(c) & 2.9(c)) is consistent with the existence of a hexatic phase in the second, third and the middle layers and a solid phase in the contact layers (as indicated by the highly peaked structure of the intensity pattern). Finally, the structure factor at $T = 101K$ (figures 2.8(d) & 2.9(d)) shows all the

layers having the structure of a hexagonal crystal. In the structure factor plots, the difference between the hexatic and the crystal phase patterns can be seen from the height and the width of the peaks in the intensity pattern. The reason for the crystal phase pattern having peaks of finite width is the finite size of the simulation cell. The structure factor patterns are consistent with the specific heat behavior in figure 2.7. In addition, the defect structures in these phases were analyzed using snapshots of molecular configurations. The molecular positions in the crystal phase correspond to a defect free hexagonal crystal (figure 2.10(a)). The hexatic phase configurations (figure 2.10(b)) show bound disclination pairs; there is also sufficient orientational order in the system. A snapshot of the liquid phase clearly indicates positional disorder and the presence of free disclinations (figure 2.10(c)). The defect structures in these snapshots are consistent with the Halperin-Nelson theory of 2-d melting. Together, these results provide strong evidence of a liquid to a hexatic to a crystal transition in the individual layers of methane. However, we note that they do not provide concrete proof of the existence of the hexatic phase, because of the relatively small size of our system. This would require a careful calculation of the free energy in the hexatic phases and a systematic finite size scaling analysis which we have not attempted here [78, 79]. For our purpose, this study provides sufficient insight into the nature of the fluid phases in figures 2.2(a) & 2.2(b) and the reason for the weakly first order nature of the freezing transition.

2.6 Conclusions

We have used the Landau free energy formalism to calculate the grand free energy of the fluid and crystalline states as a function of temperature, for LJ methane confined in slit-shaped pores. The free energy difference between the ordered and the

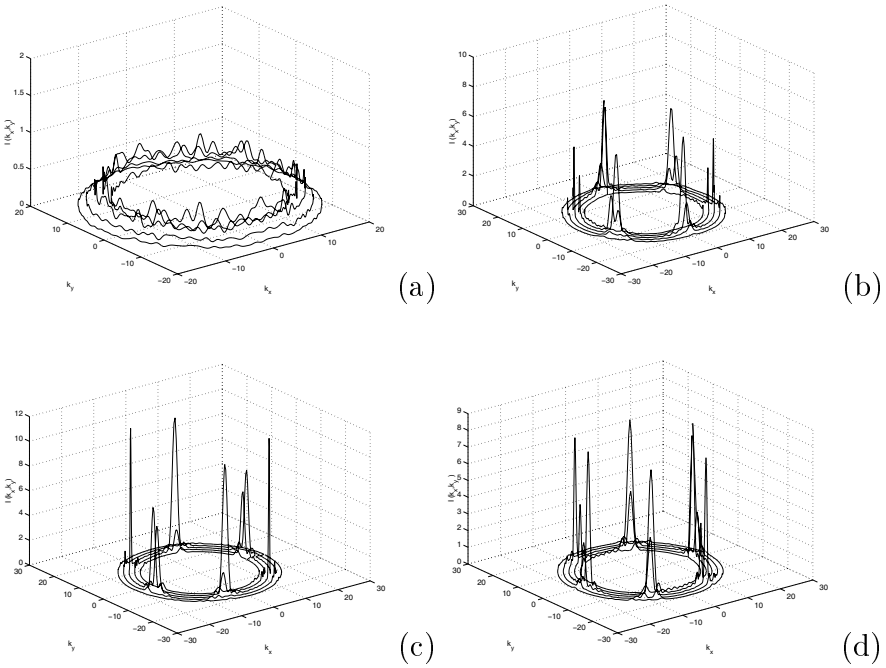

Figure 2.8: The structure factor $I(k_x, k_y)$ (k_x, k_y being measured in nm^{-1}) for the first or contact layer in the graphite pore at (a) $T = 160K$, (b) $T = 128K$, (c) $T = 111K$, (d) $T = 101K$.

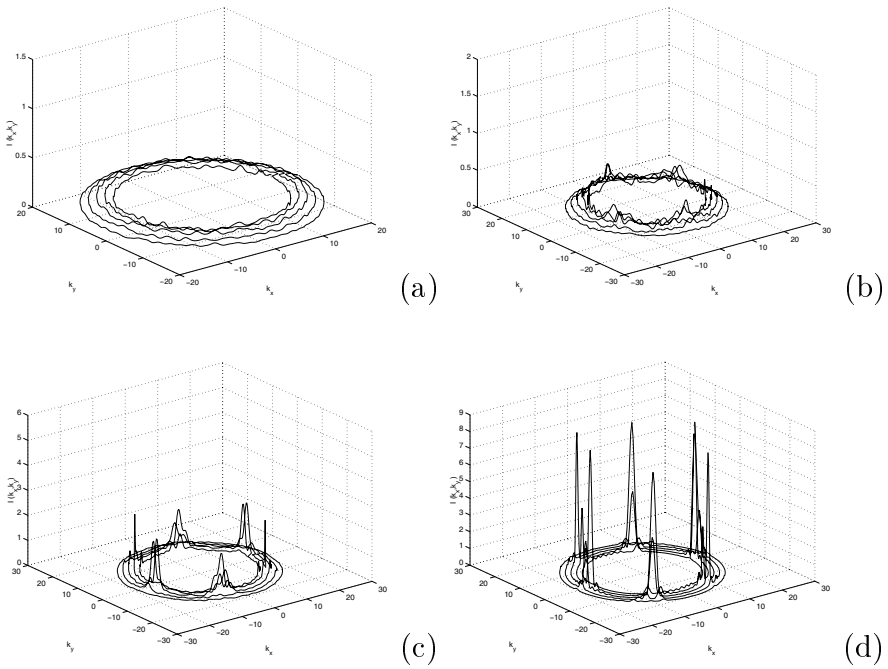

Figure 2.9: The structure factor $I(k_x, k_y)$ (k_x, k_y being measured in nm^{-1}) for the third layer in the graphite pore at (a) $T = 160K$, (b) $T = 128K$, (c) $T = 111K$, (d) $T = 101K$.

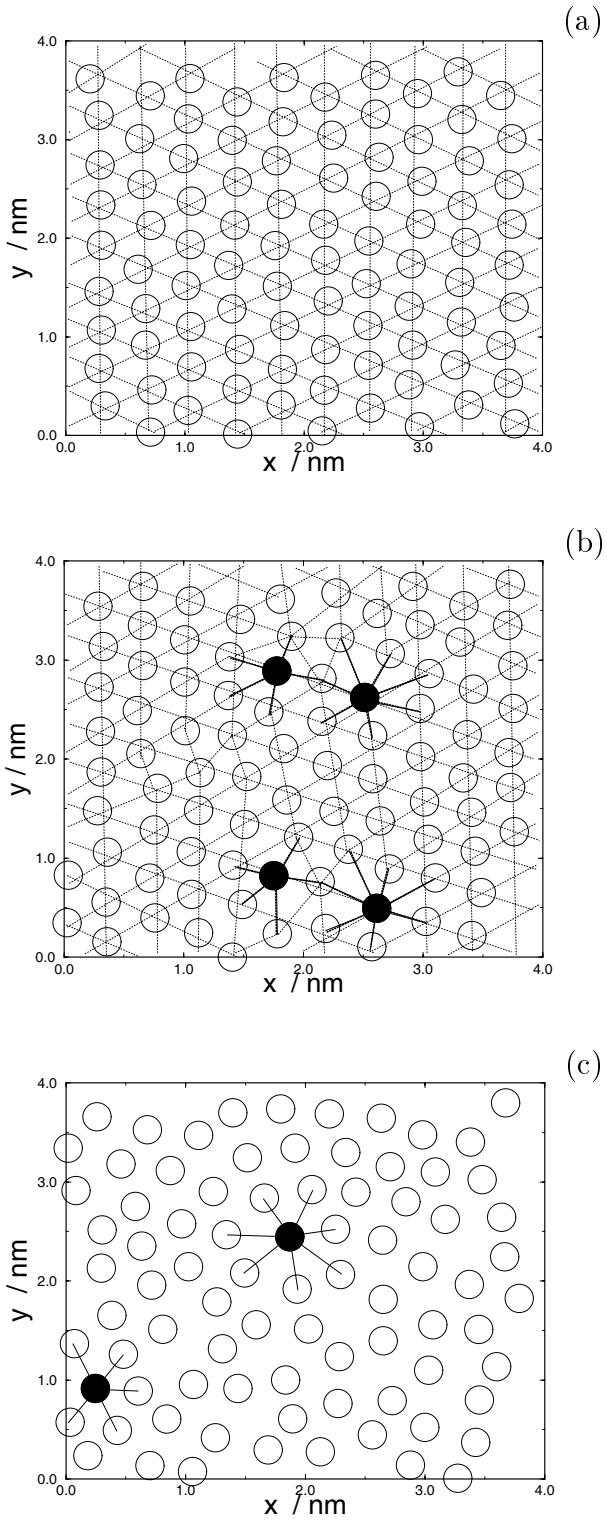

Figure 2.10: Snapshots of molecular configurations in the contact layer showing the defect structures in the (a) Crystal phase ($T = 101K$), (b) hexatic phase ($T = 128K$), (c)liquid phase ($T = 160K$).

disordered state is directly calculated, thereby eliminating the need to numerically integrate the free energy, starting from a well characterized reference phase. Thus, unlike the methods that involve thermodynamic integration, this method is not limited to repulsive or weakly attractive fluid-wall potentials. In addition to the free energy, this method provides quantitative information on the energy barrier to nucleation, although this is a quantity sensitive to system size effects and needs careful interpretation. However, the free energy difference is only a weak function of system size, and is estimated to an accuracy of $1k_BT$, as shown by Lyndenbell *et al.* [60]. Our free energy results clearly indicate a first order fluid to crystal transition for methane confined in both hard wall and graphite pores. They also confirm the sensitivity of the shift in the freezing point to the nature of the fluid-wall potential [47], by calculating the exact temperatures at which the transitions occur. The exact location of the equilibrium transition temperature by free energy calculation is an improvement over methods that use the jump in the density to locate the freezing/melting points in terms of accuracy, as it is independent of the width of the hysteresis loops.

Methane confined in graphite shows strong evidence of a quasi-two-dimensional behavior, and our results indicate the occurrence of an intermediate hexatic phase between the fluid and crystal phases. The specific heat and structure factor calculations, and the analysis of defect structures, support the Halperin-Nelson theory of two-dimensional melting. These results also provide an explanation for the weak first order nature of the freezing transition, as most of the entropy change is believed to occur in the fluid-hexatic transition. A rigorous proof to the existence of the hexatic phase would involve a careful analysis of system size effects, which we have not attempted. The fluid-hexatic transition could be studied in more detail using

the Landau free energy method by choosing a more appropriate order parameter. It may also be possible to directly observe the hexatic phase experimentally, using electron diffraction or equivalent techniques on fluids confined in graphite pores.

The extension of the free energy method to fluids confined in model cylindrical pores and other, more realistic, pore models that include poly-dispersity and pore networks would be of great practical interest. Such calculations would enable direct comparison with experimental data on freezing and melting in pores to be made. The key to such a study is finding a suitable order parameter that distinguishes between the ordered and disordered phases.

Chapter 3

Freezing of Simple Fluids in Activated Carbon Fibers

This chapter describes an application of the Landau free energy formalism (described in chapter 2), that deals with the study the freezing of CCl_4 in microporous activated carbon fibers (ACF), using Monte Carlo simulation and differential scanning calorimetry (DSC). Micro-porous activated carbon fibers are well characterized porous materials, having slit–shaped pores due to the voids formed between graphitic basal planes. They serve as highly attractive adsorbents for simple non-polar molecules, the adsorbent-adsorbate interaction being mostly dispersive (of the van der Vaals type). Recent molecular simulation studies have predicted an *upward shift* in the freezing temperature ($\Delta T_f = T_{f,pore} - T_{f,bulk} > 0$) for simple fluids confined in such highly attractive carbon slit pores. Our DSC experiments verify these predictions about the *increase* in T_f. The results also indicate significant deviation from the prediction of ΔT_f based on the Gibbs-Thomson equation (simple capillary theory). The Landau free energy method is employed to calculate the exact freezing temperature in these confined systems using molecular simulation, in order to

address the failure of the simple capillary theory.

3.1 Experimental Method

Pitch-based activated carbon fibers of different pore widths (P5, P10 and P20, see Table 3.1) in the micropore region were used as adsorbent materials. The pore width H reported throughout this paper is the distance between the planes through the carbon nuclei in the first atomic layer of each of the opposing walls. The micropore volume, specific surface area and the average slit pore width were determined by high resolution N_2 adsorption measurements at 77 K [80]. CCl_4 was adsorbed on dry ACF samples at 303 K from a gas phase at the saturated vapor pressure. The DSC scans were performed at temperature scanning rates of 5.0-1.0 $Kmin^{-1}$ using a MAC Science, DSC3100 calorimeter. The freezing and melting temperatures were measured by identifying the peak positions in the DSC scan relative to the background, and the enthalpies of the phase change were calculated from the peak areas.

3.2 Simulation Method

Potential Models

The interaction between the adsorbed fluid molecules is modeled using the Lennard-Jones (12,6) potential with size and energy parameters chosen to describe CCl_4. The LJ parameters were fitted to the bulk properties at solid-liquid coexistence, and are:

$$\sigma_{ff} = 0.514 \text{ nm}, \quad \epsilon_{ff}/k_B = 366 \text{ K}$$

The above parameters predict the correct melting temperature (T_m) and liquid

Table 3.1: Summary of Pore Widths

Pore Type	H/nm experiment	H/nm simulation	No. of layers
Micropores:			
-	-	0.94	1
P5	1.09	-	1-2
P10	1.20	-	1-2
P20	1.44	1.44	2
-	1.74	1.74	3
-	-	1.93	3
Mesopores:			
-	-	2.44	4
-	-	2.93	5
-	-	3.87	7
-	-	7.25	14

Table 3.2: Physical Properties of CCl_4

Property	Real CCl_4	LJ-CCl_4
T_m (at 1 atm.)	251.8 K	252 K
ρ_l	1.59 g/cc	1.55 g/cc
crystal type	Rhombohedral	fcc
λ_f	16.1 J/g	21.3 J/g

density (ρ_l) at coexistence, at a pressure of 1 atm.. However, these parameters fail to predict the correct crystal structure; the LJ crystal is fcc, while real CCl_4 freezes into a rhombohedral phase. As a result, the latent heat of melting, λ_f, is not given accurately by this model. The properties of real CCl_4 and LJ-CCl_4 are compared in Table 3.2.

We model activated carbon fibers as regular slit-like graphite pores. For the fluid-wall interaction, we use the integrated "10-4-3" Steele potential [53, 54] that corresponds to a smooth wall (equation 2.1). The potential parameters for the graphite wall were taken from refs. [53, 54]. For a given pore width H, the total potential energy from both walls is given by equation (2.2)

Characterization methods based on nitrogen adsorption have been used to determine the pore size distribution in pitch-based activated carbon fibers [80]. The maximum deviation in the pore width was within 10% of the mean pore width. Since the porous matrix is formed from the interstecies created by re-orientation of

the basal graphitic planes during the activation process [17], a regular slit shaped geometry is a reasonable first approximation in modeling these porous materials. We expect the approximation of a structureless graphite wall to be a good one in our present study, since the diameter of the LJ CCl_4 molecule (0.514 nm) is much larger than the C-C bond length in graphite (0.14 nm), so that the CCl_4 molecules only feel a mild corrugation in the fluid-wall potential in passing along the surface. This has been confirmed by simulations of monolayers of methane on structured, planar carbon walls [55], where wall structure had only a minor effect for temperatures down to 60 K, and by Miyahara and Gubbins [47], where it was found that the structure of methane was practically identical when confined between smooth and structured graphite pore walls, for both the fluid as well as the solid phase.

The simulation runs were performed in the grand canonical ensemble as described in ref. [56], fixing the chemical potential μ, the volume V of the pore and the temperature T. The pore width in the simulation was varied from 2 σ_{ff} to 15 σ_{ff} accommodating single adsorbed layers to up to 14 confined layers of CCl_4 (see Table 3.1), and the rectilinear simulation cell was $10\sigma_{ff}$ by $10\sigma_{ff}$ in the plane parallel to the pore walls, consistent with a cutoff of $5\sigma_{ff}$ for the fluid-fluid interaction. The system typically had between 200 to 1200 particles, and periodic boundary conditions were employed in the plane parallel to the pore walls. The simulation was setup such that insertion, deletion and displacement moves were attempted with equal probability, and the displacement step was adjusted to have a 50% probability of acceptance. Thermodynamic properties were averaged over 100-500 million individual Monte Carlo steps. The length of the simulation was adjusted such that a minimum of fifty times the average number of particles in the system would be inserted and deleted during a single simulation run.

The free energy formalism used here (see chapter 2) is quite general; it is not necessary to assume any type of crystalline structure in advance. Thus, for the sake of generality and simplicity, a rectilinear simulation cell was chosen as opposed to a geometry that is consistent with a particular structure of the confined solid phase. In order to avoid artifacts in the phase behavior due to small system size and incommensurable nature of the crystalline phase at the edges of the simulation cell, we performed a system size scaling study, and chose cell dimension to be large enough for the edge effects to be negligible (see Appendix) [81]. The conclusion of this system size study is similar to that of a similar system size study for bulk systems by Lynden-Bell et. al. [60]. We have used a free energy method that relies on the calculation of the Landau free energy as a function of an effective bond orientational order parameter Φ, using GCMC simulations described in chapter 2.

3.3 Experimental results

In figure 3.1 is shown the evolution in the DSC patterns of different CCl_4-ACF samples obtained during melting and freezing runs. The positions of the peaks in the DSC spectrum were found to be independent of the temperature scanning rate in the range 1.0 to 5 Kmin.$^{-1}$. The scan for bulk CCl_4 is shown as a reference; three "exothermic" peaks at 242 K, 228 K and 218 K are observed during the freezing run, and correspond to liquid to metastable fcc-solid phase, fcc to rhombohedral phase and rhombohedral to monoclinic phase respectively. The observed transitions are systematically shifted by 10 K compared to the values found in the literature because of supercooling achieved during the freezing run. Freezing/melting in the confined system occurs at 299 K; the peak positions in each of the DSC scans for melting and freezing runs corresponding to CCl_4 confined in ACF's (P5, P10 and P20) show

an *upward* temperature shift of 57 K. Unlike the prediction by the Gibbs-Thomson equation, the freezing temperature is found to be independent of pore width in the micropore regime (H = 1.0-1.4 nm); see figure 3.7. The enthalpies of freezing for the confined system, calculated from the peak areas were reproducible to within 1.0 %, and were much less than that of the bulk [80]. A similar trend in the shift in freezing temperature was also observed for the case of benzene confined in ACF fibers [82]. The nature of the solid phase cannot be determined by DSC experiments alone. However, the peaks corresponding to the solid-solid transitions that take place in the bulk are absent in the confined system.

3.4 Results from the simulation

The adsorption of CCl_4 in the carbon slit pores of various pore widths was calculated as a function of temperature, as the system was cooled. The chemical potential of CCl_4 in the GCMC simulation was always maintained at a value corresponding to an external bulk pressure of 1 atm.. A Lennard-Jones equation of state was used to relate the chemical potential to the pressure [62]. For a pore width H = 1.44 nm (modeled after P20 ACF), the adsorption curve is shown in figure 3.2 along with pair correlation functions at three different temperatures. The confined phase is characterized by two layers (see Table 3.1). The $g(r)$ plots represent the in-plane two-dimensional pair correlation functions within each layer. A sharp increase in the adsorption is seen to occur on cooling from 380 K to 360 K, and the corresponding pair correlation functions (at 410 K and 360 K) show that this jump is not due to a freezing transition, as the structure of the fluid remains isotropic even at 360 K. However, comparing the rates of decay of $g(r)$ with r, the positional correlations at 360 K are longer ranged than those at 410 K. Since the system is close to the

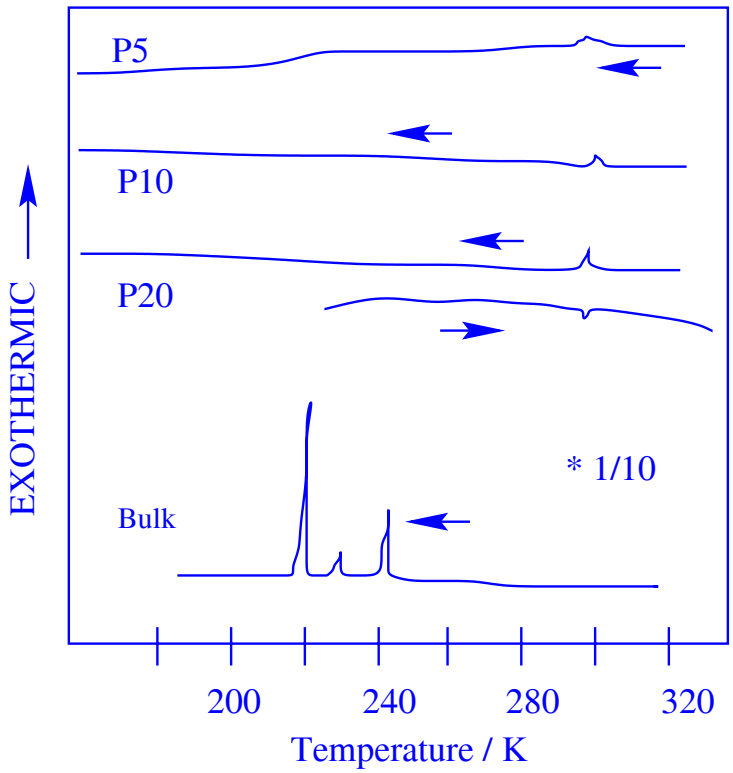

Figure 3.1: DSC scans for freezing of CCl_4 in the bulk and melting/freezing of CCl_4 confined in ACF's, after subtraction of background signal. Each scan is shifted in vertical scale for the sake of clarity. The scale for the bulk is reduced by a factor of ten. The arrows represent the direction of the temperature scan, i.e., freezing or melting; DSC scan corresponding to a melting run is shown only for the case of P20 ACF.

two-dimensional limit, there is the possibility of an orientationaly ordered phase intervening between the disordered liquid phase and the positionally ordered crystal phase; such a phase could cause the jump in the adsorption curve (see chapters 2 & 6). The pair correlation function at 340 K represents a 2-d hexagonal crystal phase.

In figure 3.3 is shown the heat capacity of the system as well as the order parameter Φ as a function of temperature. The peak in the heat capacity occurs simultaneously with a jump in the orientational order parameter Φ, in a temperature range where the positional correlations show no long range order (the $g(r)$ functions remain isotropic). The heat capacity peak and the jump in the orientational order parameter are reminiscent of the non universal behavior predicted by the transition from the liquid to an orientationaly ordered phase (see chapters 2 & 6) that occurs at the same temperature at which the jump in the adsorption curve is seen. Further evidence of such a transition was provided by studying the defect structures; isolated and bound disclination pairs were observed in the snapshots of the simulation [83].

The Landau free energy was calculated as a function of the average hexagonal bond order Φ for different temperatures for CCl_4 confined in the graphite pore of width, $H = 1.44$ nm. Each Landau free energy curve at a particular temperature possessed three minima, corresponding to three phases in the system; a liquid phase "L" with $\Phi \approx 0$ and $g(r)$ similar to figure 3.2 (b), an orientationaly ordered hexatic phase "I" with $0 < \Phi < 0.85$ and $g(r)$ similar to figure 3.2 (c) and a hexagonal crystal phase "C" with $\Phi \approx 0.85$ and $g(r)$ similar to figure 3.2 (d). The grand free energy was calculated from the Landau free energy curves using equation (2.7). The grand free energy Ω as a function of temperature for the three phases is shown in figure 3.4. The weak cross-over of the "L" and the "I" branches represents a transition to the

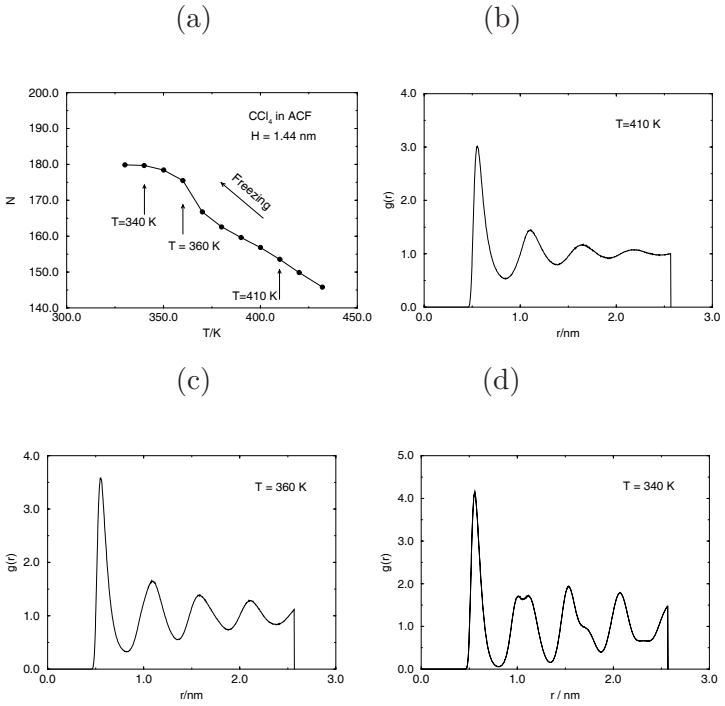

Figure 3.2: Molecular simulation results showing amount of adsorption during a freezing run and structure of confined LJ CCl_4 in a graphite pore of width H = 1.44 nm. Bulk gas phase is at 1 atm. pressure. The confined phase has two molecular layers of CCl_4. The pair correlation functions in (b) and (c) represent an isotropic fluid-like phase, while the $g(r)$ in (d) corresponds to a hexagonal crystal.

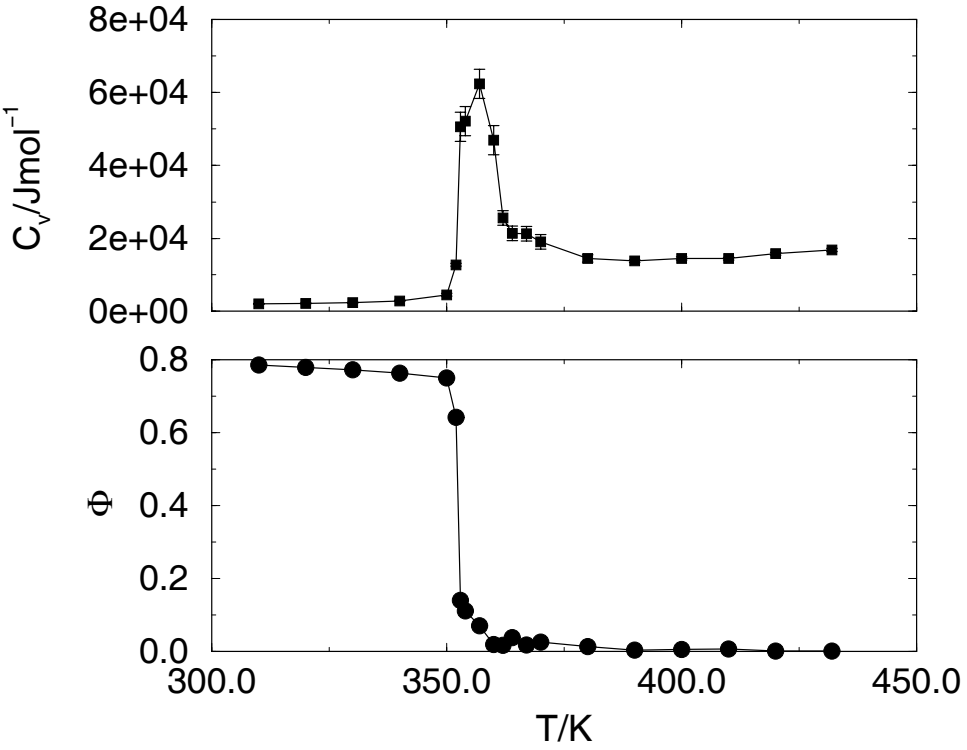

Figure 3.3: Heat capacity of the whole system and the order parameter Φ as a function of temperature as the system is cooled, for the LJ CCl_4 in a graphite pore of width $H = 1.44$ nm. For this pore width the pore only contains two layers ($j = 1, 2$) and the average order parameter Φ is equal to Φ_j.

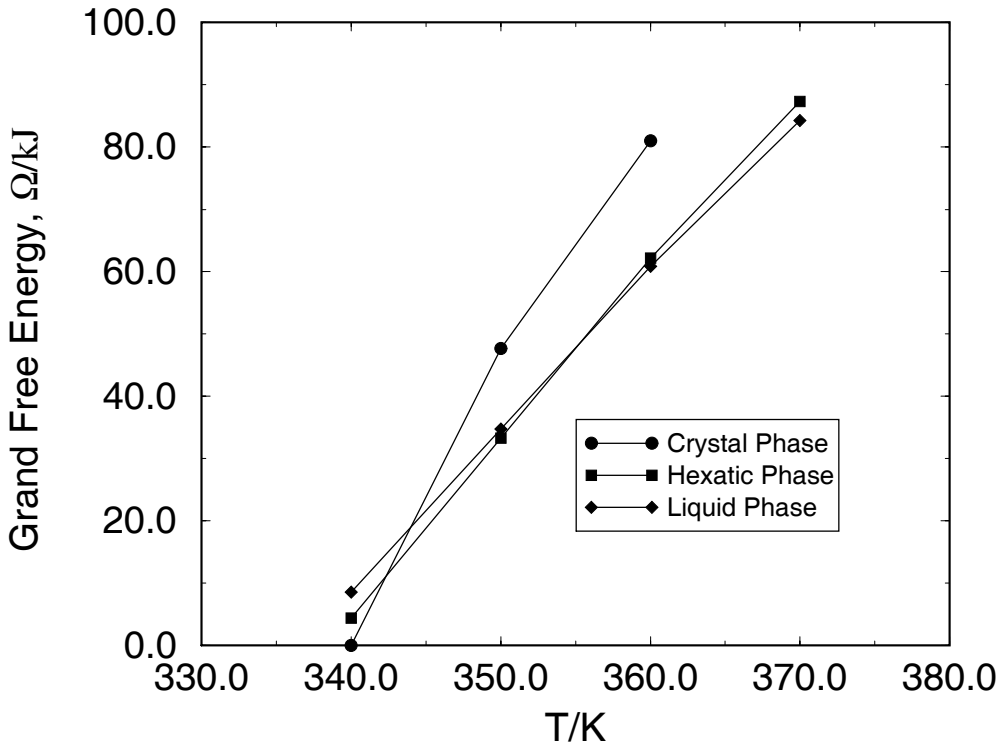

Figure 3.4: The grand free energy of the three phases L, I and C, as a function of temperature for LJ CCl_4 in a graphite pore of width $H = 1.44$ nm. The cross-over points correspond to first order phase transitions.

hexatic phase at $T = 355$ K (see appendix). The freezing transition occurs at $T = 342$ K.

The Landau free energy calculation was repeated for the different pore sizes described in Table 3.1. For pore widths that accommodate one to three confined CCl_4 layers, it was found that all the layers froze in unison at the freezing temperature, and that this temperature was much higher than the bulk freezing temperature of LJ CCl_4. For pore widths that accommodate four or more layers of adsorbate, an orientationaly ordered phase was again observed [83]. However, for these larger pore widths, it was found that the contact layers froze at a higher temperature than the inner layers which in turn froze at a temperature above the bulk freezing

temperature. The Landau free energy formulation provided the means to calculate both transition temperatures. Each Landau free energy curve at a particular temperature showed a triple-well structure (with three minima), corresponding to (1) a phase with isotropic fluid structure within each layer, (2) a phase with frozen contact layer (the inner layers being fluid-like) and (3) a phase with all the layers having the structure of a 2-d hexagonal crystal. The cross-over of the grand free energy functions for each phase gave the thermodynamic freezing temperature of the contact layers and the inner layers. The effects of system size on the free energy results are discussed in appendix. The freezing temperatures of the contact and the inner layers are summarized in Table 3.3 for the various pore widths used in this study.

The parameter d in Table 3.3, represents the inter-layer distance (average distance between the confined layers of CCl_4), which depends on the pore width H; for a given H, d is the same for the liquid and solid phases. For the bulk crystal in the simulation (fcc lattice), $d = \sqrt{2}\sigma_{ff}/\sqrt{3}$. The ease with which the fluid freezes in the pore and the extent of the hysteresis loops depend crucially on the inter-layer separation d, refs. [47, 83, 84]. For $d/\sigma_{ff} \geq 0.95$ the fluid freezes into a defect free crystal in our simulations, with hysteresis loops observed during adsorption and desorption spanning 2-10 K. The defects in the crystal structure increase in the range $0.90 \leq d/\sigma_{ff} \leq 0.95$, with the extent of hysteresis loops increasing to about 10-30 K and the thermodynamic freezing temperature of the inner layers decrease as d decreases. For $d \leq 0.90$, the inner layers of the confined fluid *do not* undergo a freezing transition. Figure 3.5 shows the freezing temperature as a function of pore width for different values of d. The thermodynamic freezing temperature is not a smooth function of pore width and shows oscillatory behavior because of its

Table 3.3: Freezing Temperatures of Confined CCl_4

Pore Width	No. of layers	T_f/K (contact layers)	T_f/K (inner layers)	d/σ_{ff}
0.94	1	410.0	-	0.95
1.44	2	342.0	-	0.95
1.74	3	335.0	-	0.84
1.93	3	333.0	333.0	0.95
2.44	4	320.0	305.0	0.95
2.76	5	310.0	273.0	0.90
2.93	5	310.0	280.0	0.95
3.68	7	300.0	248.0	0.90
3.87	7	300.0	260.0	0.95
7.25	14	290.0	254.0	0.95
bulk	∞	-	250.0	0.82

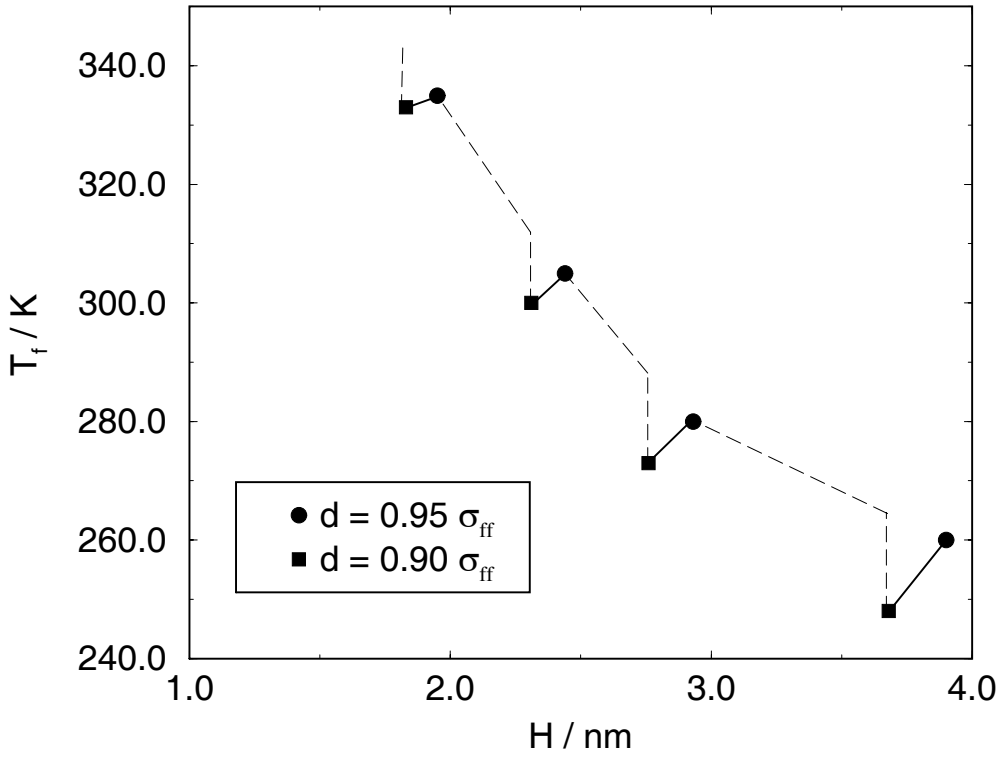

Figure 3.5: The thermodynamic freezing temperature of the inner layers calculated using the Landau free energy method for different pore widths and different values of d.

crucial dependence on d. There are windows of pore widths where the fluid does not freeze because of the lower bound in the value of $d = 0.90\sigma_{ff}$ that supports freezing. However, we find that the freezing temperatures of the contact layers are only weakly dependent on d (see Table 3.3). Thus in our study we have chosen pore widths that have different number of confined layers but all having the same inter-layer separation. The variation of the freezing temperature of the contact and the inner layers as a function of pore width is shown in figure 3.6.

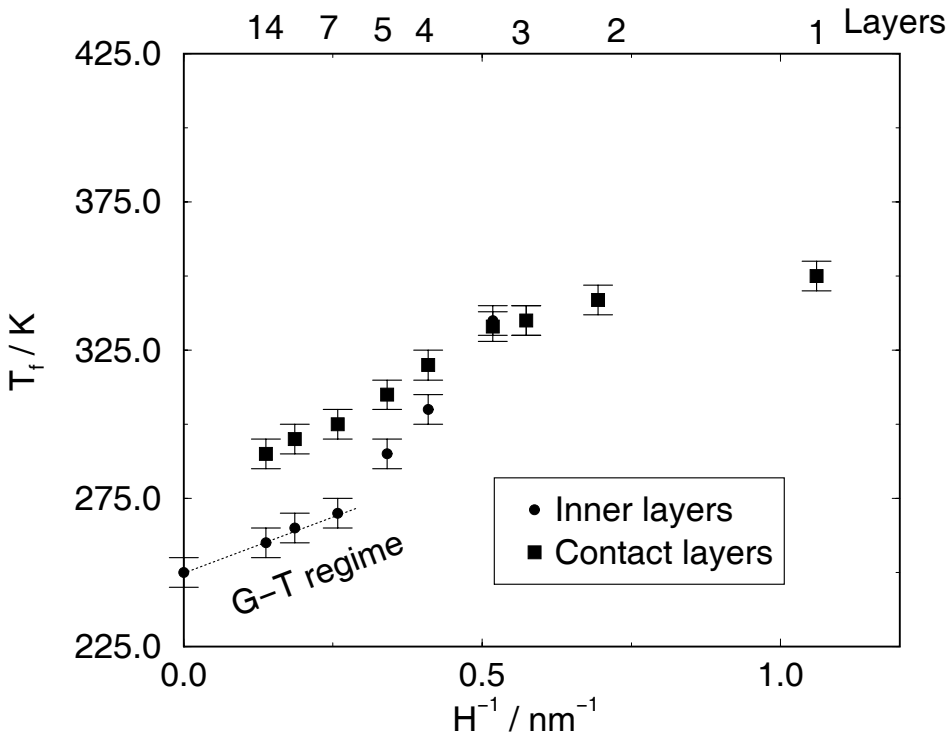

Figure 3.6: Freezing of the contact and the inner layers of LJ CCl_4 as a function of pore width. The dashed line represents the region in which a linear equation is valid, consistent with the Gibbs-Thomson equation. The freezing temperatures are determined using the Landau free energy method.

3.5 Discussion and Conclusions

The Landau free energy formalism was used to calculate the grand free energy of the fluid and crystalline states as a function of temperature, for LJ CCl_4 confined in slit-shaped pores. The free energy difference between the ordered and the disordered state is directly calculated, thereby eliminating the need to numerically integrate the free energy, starting from a well characterized reference phase. Thus, unlike the methods that involve thermodynamic integration, this method is not limited to repulsive or weakly attractive fluid-wall potentials. In addition to the free energy, a quantitative estimate of the free energy barrier to nucleation is obtained, although such a quantity is sensitive to system size effects. However, the absolute value of the free energy difference is only a weak function of system size, and is estimated to an accuracy of $1k_BT$, as shown by Lynden-Bell et. al. [60]. The exact location of the equilibrium transition temperature by free energy calculation is an improvement over methods that use the jump in the density to locate the freezing/melting points in terms of accuracy, as it is independent of the width of the hysteresis loops, thereby allowing a direct consistency check with the Gibbs-Thomson equation, equation (1.1). A direct comparison with equation (1.1) would involve calculation of surface tensions in the simulation, which we have not attempted in this study. The behavior of ΔT vs. $1/H$ in figure 3.7 is linear in the mesopore range, down to a pore width of 2.44 nm, below which there is a cross over to a "plateau" regime (in the micropore range). The plateau regime spans pore widths that can accommodate 2-3 layers of CCl_4. For pore widths that support only a single layer of CCl_4 a sharp increase in the freezing temperature is seen. The linear regime in the mesoporous range is consistent with the Gibbs-Thomson equation. The deviation from linearity (in the micropore region) is also expected, as the Gibbs-Thomson equation breaks down in

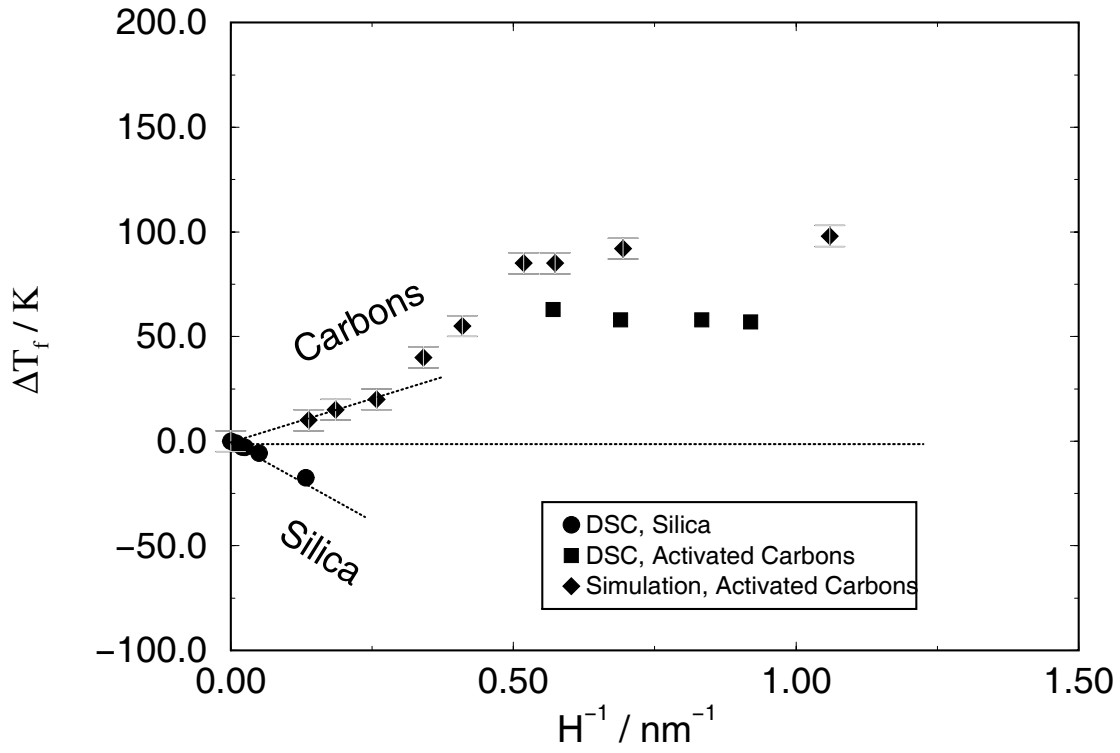

Figure 3.7: Comparison of the freezing temperatures from simulation and experiment. The results for activated carbons are from this study. The DSC results for silica are reproduced from [2].

this limit, for reasons that are discussed below.

There are either two or three condensed phases of confined CCl_4, depending on the pore width. For pore widths that accommodate four or more layers, there are three phases; Phase A corresponds to all layers having a liquid-like structure; phase B corresponds to the contact layers (the layers adjacent to the two pore walls) being frozen and the rest of the layers being fluid-like; phase C corresponds to all the layers being frozen. Thus, the contact layers freeze at a higher temperature than the inner layers. For pore widths that accommodate three layers or less, there are just two condensed phases, liquid and crystal, i.e., the contact layers freeze at the same temperature as the inner layers. It is evident from figure 3.6 that the Gibbs-

Thomson equation is valid when the effect of the contact layers are negligible on the inner layers, i.e., for pores that accommodate seven molecular layers of CCl_4 or more. When the number of inner layers are comparable with the number of contact layers, a deviation from linear behavior (G-T regime) is observed, followed by a cross-over to the plateau regime. It is also evident from figure 3.6 that the freezing temperature in the plateau regime is determined by the freezing of the contact layers. This region is spanned by pore widths that accommodate two to three layers of CCl_4. Based on energetic considerations alone, it is reasonable to assume that the contact layer freezing temperature is approximately independent of H in this limit; the depths of the potential well in which the contact layers are confined are approximately equal for all pore widths that support more than one layer. As the number of inner layers increase, the effective fluid-fluid potential between layers as well as entropic effects have to be taken into consideration, which is why there is a deviation from the plateau regime; the deviation from the plateau regime is observed for the contact layers as well as the inner layers.

The comparison of the DSC results and the simulation (figure 3.7) shows that the simplified model of spherical LJ CCl_4 and regular slit shaped graphite pore with smooth walls captures the plateau in the $\Delta T(H)$ function; however it overestimates the shift in the freezing temperature. In this regime, ΔT_f is 60 K in the experiments (figure 3.1) and is about 90 K in the simulation. We note that the DSC experiments were at done at a constant pressure equal to the saturated pressure of CCl_4 at 303 K (0.15atm.), while the pressure in the simulations was set at 1 atm. This difference in the pressure is expected to have a very small effect on the freezing temperature [47] (the solid-fluid co-existence line in the P-T phase diagrams have a slope nearly equal to infinity). We recalculated the freezing temperatures in our

simulations for the pressure used in the DSC experiments and found the difference to be less than 2%. It is difficult to see the cross-over behavior in experiments, due to the lack of availability of well characterized graphitic pores in the mesopore region. The overestimation of the freezing temperature shift in the simulation is a reflection of the simplicity of the model used. It is easier for spherical molecules in slit pores to freeze when compared to five-site LJ tetrahedral molecules (a more realistic representation of CCl_4) in a real activated carbon. The confined crystal phase has perfect in-plane bond orientational order within each layer and, in addition requires that the phase of the complex order parameter Φ_j within each layer j be the same. It is intuitively clear that both the in-plane ordering and the phase ordering of the layers are easier with spheres compared to tetrahedrons. More realistic fluid-fluid potential models based on site-site LJ interactions [85, 86] could lead to an improvement in the prediction of the simulation results.

Another simplifying assumption in our simulation is the slit shaped geometry to represent the ACF. The electron micrograph of graphitic pores points to the need to include important features like networking, polydispersity, surface corrugation and irregularities and pore bottlenecks that are ignored in our model [1]; these features are bound to deter the freezing transition in real porous materials. The typical pore size distribution in activated carbon fibers is about 10% around the mean pore size of the sample, and there is a distribution of parallel slit shaped pores and pores having a wedge geometry. In addition, the presence of active sites (for example, NH_2, $CH = O$ and CH_3OH) on the adsorbent surface have a strong influence on the freezing of confined fluids, causing a depression in the freezing temperature [87]. The absence of some of these features in our simulations could possibly account for the over estimation of the shift in the freezing temperature.

Kaneko et. al. have reported the enthalpy change on freezing in ACF based on the DSC scans that are much lower than the enthalpy change in the bulk [80]. Based on our simulation results there can be more than one reason for freezing in confined systems being weakly first order. Thus, the enthalpy change in the transition from the orientationaly ordered phase to the crystal phase can be considerably reduced when compared with the bulk. The heat capacity plot in figure 3.3 shows a peak corresponding to the orientational ordering (hexatic phase) of the confined liquid. It is clear that most of the entropy change occurs during this transition, and as a result, the orientationaly ordered fluid to crystal phase is weakly first order. Iiyama et. al. [88, 89] employed X-ray diffraction to study the structure of confined CCl_4 in ACF. The authors found extended positional correlations in the confined liquid phase providing indirect experimental evidence of the possibility of an orientationaly ordered phase. The orientational ordering transition is not captured in the DSC scans in figure 3.1, possibly because the real porous material has corrugations in the fluid-wall potential, due to the crystal structure of graphite, that makes it periodic. This periodicity in the wall potential exerts a hexatic field, that favors the formation of the orientationaly ordered phase, so that such a transition actually occurs at a higher temperature in real materials as compared to simulations that use a smooth wall potential. One possibility is that such a peak is present at temperatures higher than the DSC scans in figure 3.1. However, it is also possible that this orientational ordering occurs at a temperature higher than the layering transition temperature, in which case such a peak would be totally absent.

Polydispersity in the real porous material can also account for the low values of the observed enthalpy change. The pore size distribution could be such that a large fraction of the pores have a pore width such that the inter layer distance in the

confined phase is less than the lower bound for d that supports freezing. Thus only a small fraction of the pores actually support a crystal phase which may cause an under-estimation of the value of the enthalpy of freezing. Curry et. al. [90] studied the freezing of simple fluids in a corrugated pore model that consisted of a slit pore with rectangular grooves carved out of one of the surfaces. Over a range of groove depths, the confined phase consisted of fluid and solid portions in equilibrium, i.e., fluid filled nano-capillaries separated by solid strips, supporting the above theory. Experiments that measure the structure factor in the confined phase using X-ray scattering could shed more light on this speculation. If this is indeed the case one would observe significant liquid-like structure even below the freezing temperature of the confined CCl_4.

3.6 Appendix

The free energy results suggest that the orientational ordering transition is weakly first order (crossing over of the free energy curves for "L" and "I" phases). In order to show that this transition remains first order in the thermodynamic limit, a finite size scaling analysis is required. A continuous transition can look like a weakly first order transition in a finite system. The reason for this is that there is always a non-zero probability of observing the unstable phase because of interface and boundary effects in a finite system, that is proportional to

$$\exp\left(-\beta N\ \delta f\right), \tag{3.1}$$

where δf is the difference in intrinsic free energy between the two phases. In the thermodynamic limit, this probability vanishes. The system size scaling study for the model used here [81], showed that the structure of the hexatic phase (phase "I")

was sensitive to the linear dimensions of the simulation cell parallel to the plane of the pore walls, L_{cell}, for $L_{cell} < 15\sigma_{ff}$. However according to the Landau free energy results, the location of the thermodynamic freezing temperature was independent of system size for $L_{cell} \geq 10\sigma_{ff}$. The absolute free energy differences between phases were independent of system size; however, the height of the nucleation barrier showed a strong dependence on system size. The snapshots of molecular configurations in the confined crystalline phase, showed no evidence of defect structures at the simulation cell boundaries [83]; thus a cell size of $L_{cell} = 10\sigma_{ff}$ is large enough not to introduce artifacts in the freezing behavior due to finite system size.

Chapter 4

Experimental Studies of Melting and Freezing

This chapter primarily deals with experimental measurements. The experimental studies are for carbon tetrachloride and nitrobenzene in controlled pore glass (CPG) and VYCOR. Differential scanning calorimetry (DSC) was used to determine the melting point in the porous materials. Dielectric spectroscopy (DS) was also used to determine melting points. Measurements by the two methods were in excellent agreement. The melting point was found to be depressed relative to the bulk value for both fluids. With the exception of smallest pores, the melting point depression was proportional to the reciprocal of the pore diameter, in agreement with the Gibbs-Thomson equation. Structural information about the different confined phases was obtained by measuring the dielectric relaxation times using dielectric spectroscopy.

The DSC and DS experiments were performed at the A. Mickiewicz University at Poznan, Poland. The CCl_4 and nitrobenzene samples were reagent grade chemicals and were twice distilled (nitrobenzene at reduced pressure) prior to use in the

experiment. Nitrobenzene was further dried over Al_2O_3, centrifuged, and stored in the absence of light to avoid contamination by photochemical reactions. The conductivities of the purified CCl_4 and nitrobenzene samples were found to be less than 10^{-16} ohm^{-1}m^{-1} and 10^{-10} ohm^{-1}m^{-1} respectively. The porous silica samples used were the commercially available Controlled Pore Glass (CPG) from CPG Inc., with a pore size distribution of about 5% around the mean pore diameter. Different CPG samples having average pore diameters ranging from 50 nm to 7.5 nm were used. We have also studied confinement in a Vycor glass from Corning Inc., having a mean pore size of 4.0 nm. The pore samples were kept under vacuum prior to and during the introduction of the fluid.

4.1 Differential Scanning Calorimetry

A Perkin-Elmer DSC7 (differential scanning calorimeter) was used to determine the melting temperatures and latent heats of fusion, by measuring the heat released in the melting of nitrobenzene. Dupont thermal analyser was used for the measurements involving CCl_4. The temperature scale of the two DSC machines were calibrated to the melting temperatures of pure nitrobenzene and CCl_4 respectively. The background of each raw DSC spectrum was subtracted, based on a second-order polynomial fit to the measured heat flow away from the signals of interest. The melting temperatures were determined from the position of the peaks of the heat flow signals and the latent heats were determined based on the scaled area under these signals. The melting temperature was reproducible to within 0.5 ^{o}C for larger pores ($\geq$ 25 nm); uncertainties were larger for the smaller pores. These uncertainties are a result of the width of the DSC peaks, which derives in part from variations in pore size, and geometry, and from the existence of metastable states.

The latent heats were reproducible to within an accuracy of 5%.

4.2 Dielectric Spectroscopy

The permittivity of a medium, $\epsilon^* = \epsilon' - i\epsilon''$, is in general a complex quantity whose real part ϵ' is associated with the increase in capacitance due to the introduction of the dielectric. The imaginary component ϵ'' is associated with mechanisms that contribute to energy dissipation in the system; these include small but non-zero conductivity of the dielectric and viscous damping of the rotational motion of the dipolar molecules in alternating fields. The latter effect is frequency dependent. The relative permittivity κ^* is given by the ratio of the permittivity of the medium to that of free space.

$$\kappa^* = \kappa' - i\kappa'' = \frac{\epsilon^*}{\epsilon_o} \tag{4.1}$$

The real part of the relative permittivity, $\kappa' = \epsilon'/\epsilon_o$ is also known as the dielectric constant. The experimental setup consisted of a parallel plate capacitor of empty capacitance $C_o = 4.2$ pF. The temperature was controlled to an accuracy of 0.1 ^{o}C by a Pt100 platinum resistor using an external K30 Modingen cryostat. The capacitance, C, and the tangent loss, $\tan(\delta)$, of the capacitor filled with nitrobenzene between the plates were measured using a Solartron 1260 gain impedance analyzer, in the frequency range 1 Hz - 10 MHz, for various temperatures [91]. For a given capacitor, the capacitance, C, is proportional to ϵ', the permittivity of the dielectric medium between the capacitor plates. The relative permittivity of nitrobenzene as a function of temperature was calculated using

$$\kappa' = \frac{C}{C_o}\,;\, \kappa'' = \frac{\tan(\delta)}{\kappa'}. \tag{4.2}$$

For the case of nitrobenzene in porous silica, the sample was introduced between the capacitor plates as a suspension of 200 μm mesh porous silica particles in pure nitrobenzene.

The dielectric constant is a natural choice of order parameter to study freezing of dipolar liquids, because of the large change in the orientational polarizability between the liquid and solid phases. The melting point was taken to be the temperature at which there was a large increase in the permittivity, as the solid phase was heated. The frequency range chosen for measurements corresponds to the typical dielectric relaxation times in the solid phase. The dielectric relaxation time was calculated by fitting the dispersion spectrum of the complex permittivity near resonance to the Debye model of orientational relaxation. The Debye dispersion relation is given by [92, 93]

$$\kappa^* - \kappa'_\infty = \frac{\kappa'_s - \kappa'_\infty}{1 + (\omega\tau)} \tag{4.3}$$

where ω is the frequency of the applied potential and τ is the orientational (rotational) relaxation time of a dipolar molecule. The subscript s refers to static permittivity (low frequency limit, when the dipoles have sufficient time to be in phase with the applied field). The subscript ∞ refers to the optical permittivity (high frequency limit) and is a measure of the induced component of the permittivity.

4.3 Results from DSC

In figure 4.1 is shown the evolution in the DSC patterns of several different CCl_4-CPG samples obtained during melting runs. The results were found to be independent of the heating rate in the range 0.5 to 5 ^{o}C/min. The relatively large minimum at

$-21.2\ ^{o}$C that is independent of pore size corresponds to the melting of the bulk CCl_4 in which the porous particles are suspended. In addition, a second minimum that is dependent on the pore size is also observed. This signal corresponds to the melting of the CCl_4 in the pores, and shifts to lower temperatures as the pore size is reduced. The third minimum (at $t = -44\ ^{o}$C) that is also independent of pore width corresponds to a solid-solid phase transition (monoclinic to rhombohedral structure at $-46\ ^{o}$C [94]) in the bulk CCl_4. In some cases (figures 4.1(a,c)), a fourth minimum occurs that may be due to such a solid-solid transition in the pore (this peak is seen as a shoulder in the solid-solid peak below $t = -44\ ^{o}$C); however DSC results alone are inconclusive in this regard. The size dependence of the melting temperature of the confined CCl_4 is shown in figure 4.2. The linear relationship between the shift in the pore melting temperature and the inverse pore diameter is consistent with the Gibbs-Thomson equation down to the smallest pore size studied ($H = 7.5$ nm). A direct test would however involve the independent measurement of the wall-fluid and the wall-solid interfacial tensions, which we have not attempted.

DSC scans corresponding to melting of nitrobenzene are shown in figure 4.3. The qualitative behavior is the same as in the case of CCl_4. The melting point of the bulk is $-5.6\ ^{o}$C (monoclinic crystal phase to liquid [95]). The melting point in the pore is always depressed and the magnitude of the shift increases with decreasing pore size. As the pore size become smaller the pore melting peak broadens, and becomes increasingly asymmetric. Since the signals corresponding to the confined nitrobenzene are better resolved and separated from the bulk signal than for the case of CCl_4, we calculated the latent heat of melting for the bulk and confined solids. The amounts of nitrobenzene partitioned between the bulk and the pore were determined by requiring the bulk signal to give the correct bulk latent heat.

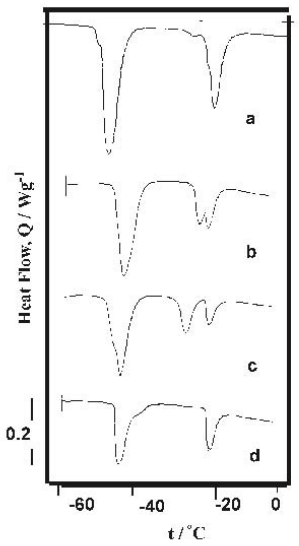

Figure 4.1: Representative DSC scans for melting of CCl_4 in CPG, after subtraction of background signal. Results are for mean pore sizes of (a) 100 nm (the second minimum occurs as a shoulder in the main peak at -21.2 ^{o}C); (b) 40 nm; (c) 20 nm; (d) 7.5 nm (the second minimum occurs as a shoulder in the solid-solid peak at -44.0 ^{o}C). The x-axis measures temperature in degree Celsius and the y-axis measures the heat flow in W/g. Each scan is shifted in vertical scale for the sake of clarity.

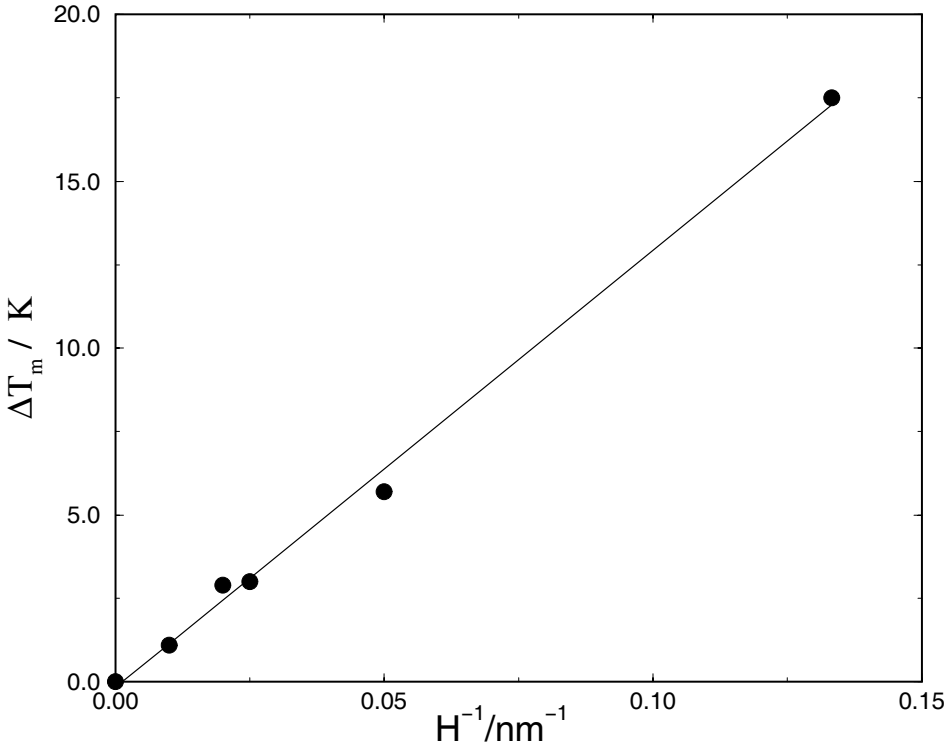

Figure 4.2: Shift in the melting temperature $\Delta T_m = T_{m,bulk} - T_{m,pore}$ as a function of $1/H$ for CCl_4 in CPG. The straight line fit is consistent with the Gibbs-Thomson equation, that is valid in the large pore limit.

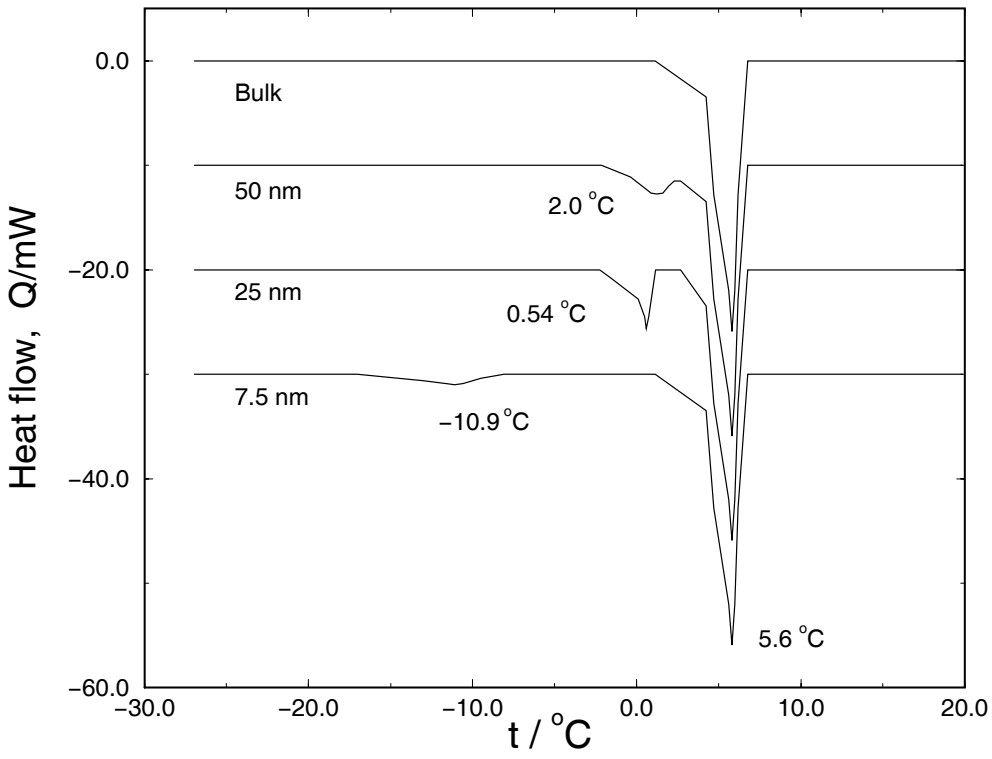

Figure 4.3: Representative DSC scans for melting of nitrobenzene in CPG, after subtraction of background signal. Results are for mean pore sizes of (a) bulk; (b) 50 nm; (c) 25 nm; (d) 7.5 nm. Each scan is shifted in vertical scale for the sake of clarity.

The values of the melting temperature t_m and the latent heat of melting λ_m are summarized in table 4.1. One possible explanation of the decrease in the latent heat values with decreasing pore size is that the crystal structure of the confined solid phase becomes increasingly disorganized as the pore size decreases.

4.4 Results from dielectric spectroscopy

The capacitance C and tangent loss $\tan(\delta)$ were measured as a function of frequency and temperature for bulk nitrobenzene and for nitrobenzene adsorbed in CPG and Vycor glass of different pore sizes ranging from 50 nm to 4.0 nm. The behavior of

Table 4.1: Heats of Melting for Nitrobenzene

Pore size, H nm	Latent heat, λ_m J/g	t_m ^{o}C
Bulk	94.5	5.6
50	79.5	3.4
25	50.0	0.4
7.5	43.8	-16.0

κ' vs. T is shown in figure 4.4 for nitrobenzene in pores of different widths, calculated at a typical frequency of 1 MHz using equation (4.2). For pure, bulk nitrobenzene, there is a sharp increase in ϵ' at $t = 5.6$ ^{o}C, corresponding to the melting point of the pure substance. For nitrobenzene confined in CPG, the sample is introduced as a suspension of nitrobenzene filled CPG particles in pure nitrobenzene, between the capacitor plates. Thus capacitance measurement yields an effective relative permittivity of the suspension of CPG in pure nitrobenzene. Thus κ' shows two sudden changes. The increase that depends on pore size is attributed to melting in the pores, while that at 5.6 ^{o}C corresponds to the bulk melting. It is interesting to note that the signal corresponding to the melting in pores gets increasingly rounded as the pore size gets smaller, in much the same way as the broadening of the peaks in DSC. For smaller pore sizes (H = 7.5 nm and 4.0 nm) the increase in κ' is continuous. Both the melting and freezing signals are shown; the hysteresis loops grow wider with decreasing pore size. The rounding of the increase in κ' is expected to be smaller than the width of the peaks in the DSC scans, as the capacitance is measured at equilibrium. The shifts in the melting temperature are plotted against

the reciprocal pore width in figure 4.5 for nitrobenzene in CPG obtained using both DSC and DS measurements. The deviations from linearity, and hence from the Gibbs-Thomson equation are appreciable at pore widths as small as 4.0 nm.

The spectrum of the complex permittivity (κ', κ'' vs. ω) is fit to the dispersion relation (equation (4.3)), to determine the dielectric relaxation time τ, which gives valuable information about the structure of the condensed phase. The frequency range in this study is expected to encompass the resonant frequencies corresponding to the dielectric relaxation in the solid phases. To probe the liquid relaxation behavior would require a frequency range that is 4 to 5 orders of magnitude higher. The Debye dispersion relation can be expressed in normalized form [96], using the normalized variable z is given by $z = \ln(\omega\tau)$ according to which the κ' function shows a point of inflection and the κ'' function goes through a maximum at the value $z = 0$. Therefore, from a spectrum plot of κ', κ'' vs. $\log_{10}(\omega)$, the relaxation time can be calculated as the reciprocal of the frequency corresponding to a saddle point of the κ' function or a maximum of the κ'' function. An alternative graphical representation of the modified Debye dispersion equation is through the Cole-Cole plot [93], in the complex κ^* plane. From a plot of κ'' vs. κ', τ is given by the reciprocal of the frequency at which κ'' goes through a maximum.

The spectrum plot for nitrobenzene in a 7.5 nm CPG at $t = -21\ ^o$C is shown in figure 4.6(a). The solid and dashed curves fit the experimental data points accurately, indicating a Debye type relaxation with a single time scale. The relaxation time is estimated to be $\tau = 1.44$ ms. At a different temperature ($t = -4\ ^o$C), the behavior is significantly different (figure 4.6(b)). The double peak structure of the $\kappa''(\omega)$ and the double inflection in the $\kappa'(\omega)$ curve suggest two different dielectric relaxation times. There is a shorter relaxation time $\tau_1 = 43.6\ \mu$s, in addition to the

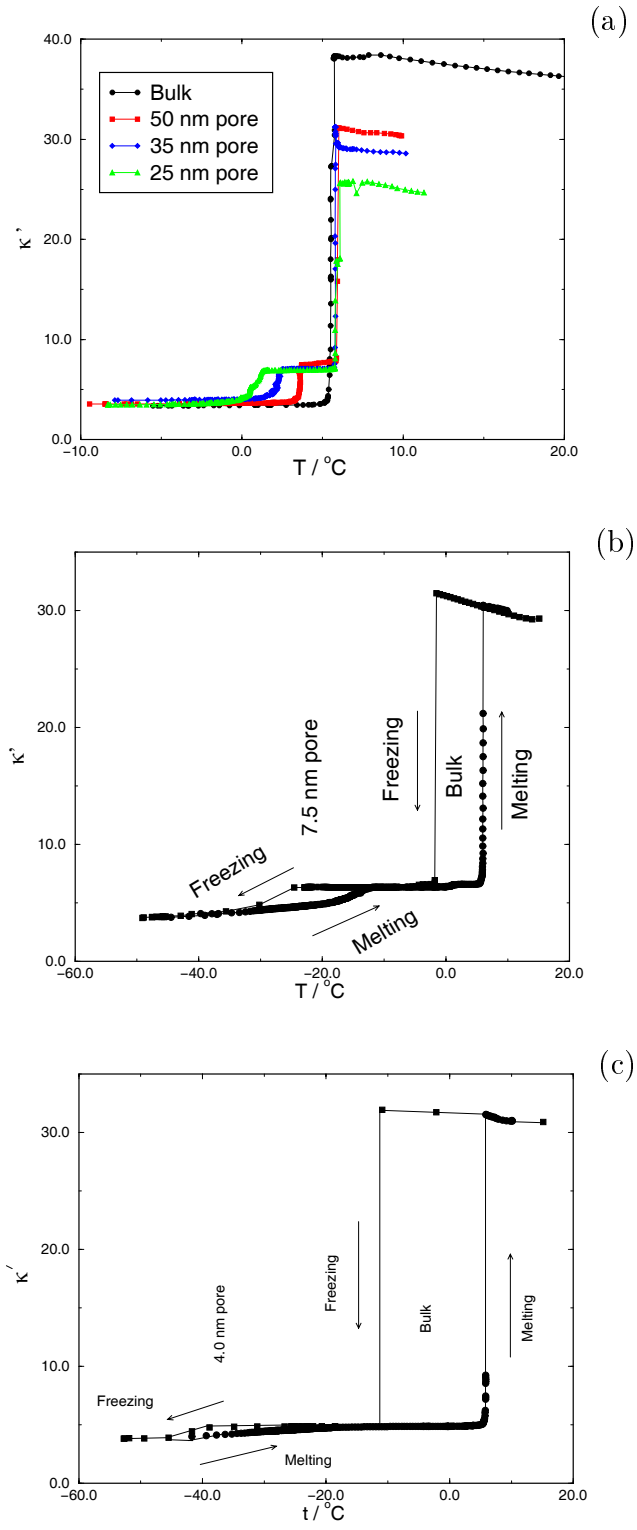

Figure 4.4: Relative permittivity, κ', as a function of temperature for different pore widths (equilibrium measurements during melting process). The measured permittivity is an effective value for the suspension of the porous silica glass in pure nitrobenzene. (plot (c) is for melting and freezing process

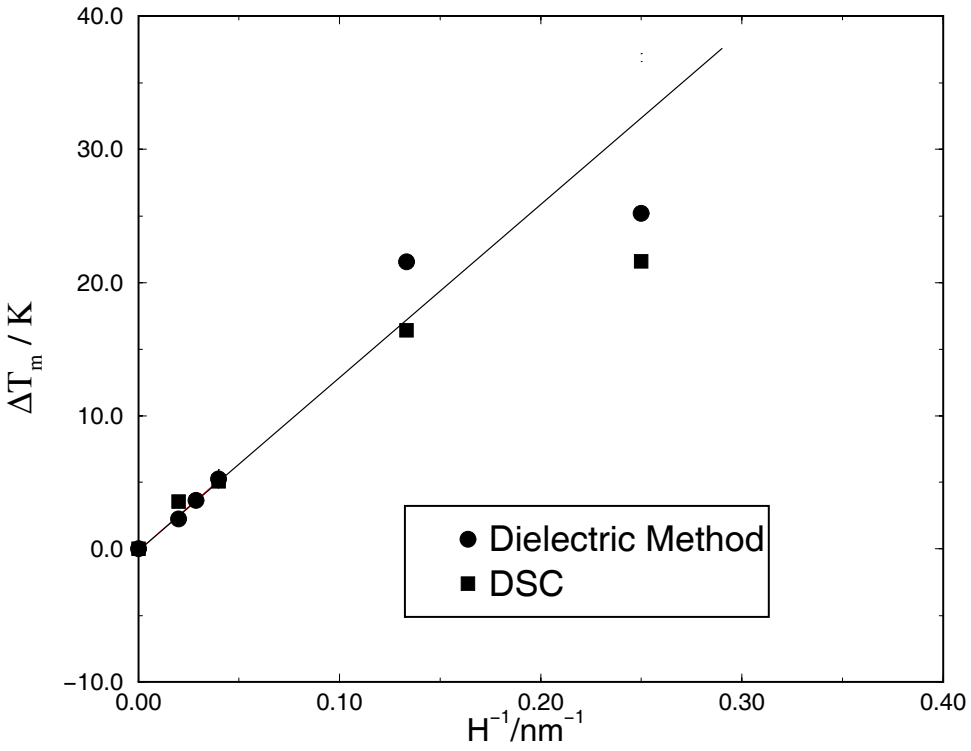

Figure 4.5: Shift in the melting temperature $\Delta T_m = T_{m,bulk} - T_{m,pore}$ as a function of $1/H$ for nitrobenzene in CPG. The DSC and the DS measurements are in good agreement. The straight line is a fit to the data for H values of 7.5 nm and above, and is consistent with the Gibbs-Thomson equation.

longer component $\tau_2 = 1.7$ ms.

4.5 Discussion and Conclusions

The simulation results and the Gibbs-Thomson equation suggest that the fluid-wall interaction for CCl_4 and nitrobenzene in CPG is less than the respective fluid-fluid interaction, and thus the freezing temperature is always depressed. For CCl_4 in CPG, this is a reasonable scenario if we realize that the fluid wall potential energy is proportional to $\rho_w \epsilon_{fw}$, (ρ_w being the density of substrate atoms in the pore and ϵ_{fw} being the fluid-wall energy parameter if we assume a LJ potential). The ratio of the fluid-wall potential energy to the potential energy that would exist if the wall was made up of the fluid molecules is then $\rho_w \epsilon_{fw} / \rho_s \epsilon_{ff}$. This ratio is about 0.5 for CCl_4 in CPG. A more accurate estimate would involve the LJ size parameters σ_{fw} and a geometrical factor that depends on H/σ_{fw}, H being the pore diameter. For nitrobenzene in CPG the situation is further complicated by the longer range dipolar interaction, which introduces a term in addition to the LJ interaction.

The permittivity measurements (the behavior of κ' with T) show that the melting transition in larger pores ($H \geq 25$ nm) is abrupt (e.g. figure 4.4(a)) and gets increasingly rounded in smaller pores ($H = 7.5$ *and* 4.0 nm), where it appears continuous (e.g. figure 4.4(b),4.4(c)). The free energy calculation in chapter 2 clearly shows that the freezing in such narrow pores is also first order. The presence of a discontinuity in the slope of the free energy curve at the transition point is a measure of the first order jump in the heat capacity. Thus, in the simulations, the hysteresis loops in the behavior of the density as a function of temperature is due to the existence of metastable states. Radhakrishnan and Gubbins [83] have studied

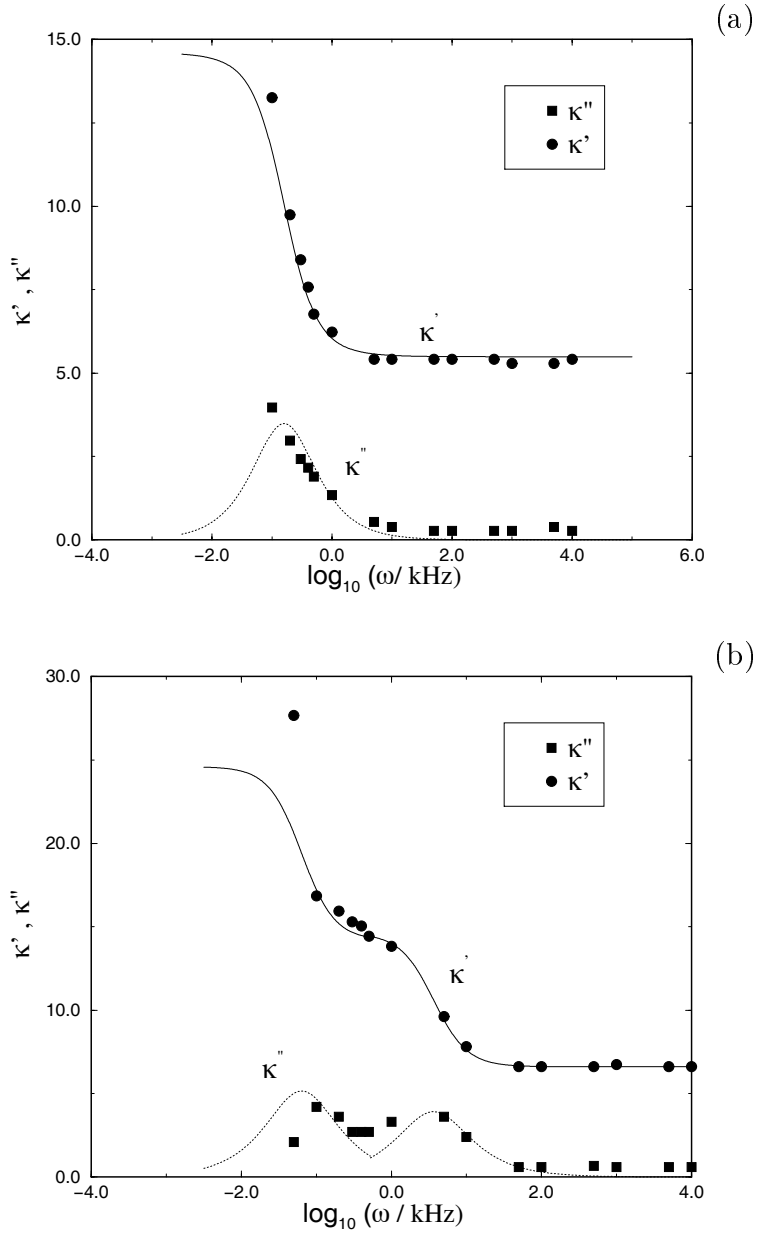

Figure 4.6: Spectrum plot for nitrobenzene in a 7.5 nm pore at (a) $t = -21\ ^{o}$C and (b) $t = -4\ ^{o}$C. The solid and the dashed curves are fits to the real and imaginary parts of equation (4.3) respectively.

the origin of these metastable states for methane confined in graphitic carbon. In a real experiment, however, slow diffusion and pore blocking can also contribute to the hysteresis behavior.

The typical dielectric relaxation time for a dipolar liquid in the bulk phase is 10^{-9} s. The relaxation time increases to 10^{-3} s when the liquid freezes to a crystal phase [91]. For dipolar molecules confined in nano-scale silica pores, the typical liquid phase relaxation time is slightly higher compared to the bulk phase, and is about 10^{-8} s [97, 98]. In addition, for a heterogeneous system there occurs a relaxation mechanism due to interfacial polarization when a slightly conducting liquid is enclosed in an insulating material. This effect, also called the Maxwell-Wagner-Sillars (MWS) polarization [99], is known to have a relaxation time of the order of 10^{-3} s [98, 100]. The CPG and Vycor samples used in this study were dielectrically neutral, in the sense that, in the temperature and frequency range of our measurements, the dielectric loss (proportional to κ'') of the empty pores were negligible compared to the liquid filled samples. Therefore, there is no background noise due to the motion of silica molecules. The dielectric relaxation component for nitrobenzene in CPG at $t = -23$ ^{o}C, with a relaxation time $\tau = 1.44$ ms (figure 4.6(a)), is attributed to the crystalline solid phases in the bulk and the pore. At $t = -4$ ^{o}C the bulk phase is still a crystalline solid, while the confined phase is a liquid. In this case (figure 4.6(b)), two distinct relaxation times appear, corresponding to two different relaxation mechanisms. The longer component relaxation, $\tau_2 = 1.7$ ms, is attributed to the bulk crystalline phase of nitrobenzene. The shorter relaxation component, $\tau_1 = 43.6$ μs, is too slow to represent the liquid phase relaxation in the pore. However, it is known that for dipolar liquids confined in nano-scale pores, the molecules in the contact layer show a slower relaxation behavior, on the order of

10^{-6} s [98, 100, 101]. Thus, the shorter relaxation component is consistent with such a behavior of the contact layer. The Landau free energy calculation for methane in graphite and the NMR study by Overloop and Van Gerven [38] dealing with water in porous silica also support the view that the molecules in the contact layer behave differently than the those in the pore interior.

We also observed two relaxation mechanisms for temperatures greater than $t = 5.6\ ^{o}$C, one corresponding to the relaxation of the molecules in the contact layer in the pores and the other (in the range of 10^{-3} s) arising because of MWS polarization. We note that in this study, we were unable to resolve the MWS relaxation component from the crystalline phase relaxation.

Chapter 5

Toward the development of a global phase diagram

Recently, Kaneko et. al. [80, 81] studied freezing of CCl_4 in activated carbon fibers using differential scanning calorimetry (DSC), and reported an elevation in T_f for the confined system, thus verifying the prediction made by simulations [47, 83]. The authors argued that, due to the high density of covalently bonded carbon atoms in graphite, the fluid-wall interaction is large and hence the observation is consistent with the previous simulation studies. In a different study, Sliwinska-Bartkowiak et al. [2] studied the effect of confining CCl_4 in silica-based pores (CPG and VYCOR) that have a rather weak fluid-wall interaction, and observed a depression of the melting temperature. These experimental studies provided an overall picture of the effect of the fluid-wall interaction on the melting of confined CCl_4, drawing a parallel with the simulation study of Miyahara and Gubbins [47]. In order to further elucidate the effect of the pore wall interaction it is necessary to understand the inhomogeneity of the fluid structure in the confined space. In the free energy study described in chapter 2, the presence of a thermodynamically stable intermediate

phase lying between the liquid phase and the solid phase was established in a rigorous manner. The study led to the conclusion that the contact layers (the layers closest to the pore walls) freeze at a higher temperature than the inner layers, and thus the intermediate phase has the structure such that the contact layers are crystalline while the inner layers are liquid-like. The effect of the freezing of the contact layers at an elevated temperature compared to the inner layers causes a significant deviation from the linear behavior predicted by the Gibbs-Thomson equation in the case of smaller pores [81] ($H < 5\sigma_{ff}$).

Sliwinska-Bartkowiak and co-workers attempted to characterize the melting/freezing transition for a dipolar fluid, nitrobenzene confined in controlled pore glass of different pore sizes, using DSC and dielectric relaxation spectroscopy [2] (see chapter 4). The depression in the melting temperature followed the Gibbs-Thomson equation for pore sizes larger than 7.5 nm; however, significant deviation was observed for a smaller pore width. The results from both experiments were in good agreement. The authors also made a quantitative estimate of the rotational relaxation time in the fluid and crystal phases by fitting the complex permittivity $\epsilon^* = \epsilon'(\omega) - i\epsilon''(\omega)$ measurements to the Debye dispersion equation. In addition to the liquid and crystal phase relaxation, a third relaxation component was observed, that supported the existence of a contact layer with dynamic properties that were more liquid like, and different from the inner layers as found in the previous studies.

The experimental studies involving x-ray diffraction as well as NMR methods, and the simulation studies involving free energies, establish the presence of a stable intermediate inhomogeneous confined phase that has important consequences for the nature of the phase transition, as well as the shift in the freezing temperatures.

The experiments done on silica based pores (weaker wall-fluid interaction) [2, 102] conclude that the contact layers freeze at a lower temperature than the inner layers while the simulation studies involved graphite pores (strong wall-fluid interaction) predict that the contact layers freeze at an elevated temperature compared to the inner layers.

In this chapter, our aim is to develop a global phase diagram, that incorporates the diverse freezing behavior described above, and consolidate our understanding of the freezing phenomenon in confined systems. We describe an other application of the Landau free energy method to study the effect of the fluid-wall interaction energy on the shift of the freezing temperature and on the fluid structure. Corresponding states theory is used to map out the global freezing behavior of a Lennard-Jones (LJ) fluid in model slit-shaped pores of varying fluid-wall interaction strengths. Using LJ parameters fitted to thermophysical property behavior, the qualitative freezing behavior for a variety of fluids and nano-porous materials is predicted using a global freezing diagram.

5.1 Simulation method

We performed Grand Canonical Monte Carlo (GCMC) simulations of Lennard-Jones methane adsorbed in slit shaped pores of width $H = 7.5\sigma_{ff}$, H being defined as the perpendicular distance between the planes passing through the nuclei of the first layer of molecules that make up the pore walls of the slit shaped pore. The interaction between the adsorbed fluid molecules is modeled using the Lennard-Jones (12,6) potential with size and energy parameters chosen to describe methane ($\sigma_{ff} = 0.381$ nm, $\epsilon_{ff}/k_B = 148.1$ K). The pore walls are modeled as a continuum of

LJ molecules using the"10-4-3" Steele potential [53, 54] (equation 2.1). For a given pore width, H, the total potential energy from both walls is given by equation (2.2). The strength of attraction of the pore walls relative to the fluid-fluid interaction is determined by the coefficient $\alpha = \frac{\rho_w \epsilon_{fw} \sigma_{fw}^2 \Delta}{\epsilon_{ff}}$ in equation 2.1. Throughout the study the fluid-fluid interaction was kept fixed and the parameters for the wall potential were varied. Six different sets of parameters were chosen for pore wall interaction that ranged from a purely repulsive wall to a strongly attractive wall; see table 5.1.

The simulation runs were performed in the grand canonical ensemble, fixing the chemical potential μ, the volume V of the pore and the temperature T. The dimensions of the rectilinear simulation cell were $10\sigma_{ff} \times 10\sigma_{ff} \times H$ for most part of the study, however we also performed a system size scaling study that involved system sizes as large as $40\sigma_{ff} \times 40\sigma_{ff} \times H$. The system typically contained up to 700 adsorbed molecules (up to 12000 molecules for the case of the largest system used in the system size scaling analysis). Periodic boundary conditions were employed in the two dimensions defining the plane of the pore walls. The simulation was set up such that insertion, deletion and displacement moves were attempted with equal probability, and the displacement step was adjusted to have a 50% probability of acceptance. Thermodynamic properties were averaged over 100-1000 million individual Monte Carlo steps. The length of the simulation was adjusted such that a minimum of fifty times the average number of particles in the system would be inserted and deleted during a single simulation run. We note that the geometry of the simulation box in our study is not commensurate with the crystal structure in the confined solid phase. However, it was ensured that the simulation box size was large enough to avoid any artifacts due to the incommensurability between the shape of the simulation box and the crystal structure [81]. We have used a free

energy method that relies on the calculation of the Landau free energy as a function of an effective bond orientational order parameter, Φ, using GCMC simulations as described in chapter 2.

5.2 Dielectric relaxation spectroscopy

The capacitance, C, and the tangent loss, $\tan(\delta)$, of the capacitor filled with nitrobenzene between the plates were measured in the frequency range, ω between 1 Hz - 10 MHz, for various temperatures [2]. For the case of nitrobenzene confined in activated carbon fibers (ACF), the sample was introduced between the capacitor plates as a suspension of porous particles in pure nitrobenzene. The contributions to the complex relative permittivity $\kappa^* = \kappa' - i\kappa''$ were determined. The electrodes were blocked using a dielectric (teflon) for samples containing the ACF, as the suspension was conducting. The Debye dispersion relation for an isolated dipole rotating in a viscous medium under alternating electric field was used to calculate the orientational relaxation time from the permittivity dispersion spectrum [2] (see chapter 4).

5.3 Results

The Landau free energy for the confined methane was calculated as a function of the order parameter Φ for different temperatures and different pore models. The different phases are identified by the different minima in the Landau free energy curves. Each phase is characterized by calculating the average value of the order parameter and the two-dimensional, in-plane pair correlation functions in each of the molecular layers by constraining the phase space trajectory such that only configurations whose

average value of the order parameter lie in the the range $\Phi_{min,phase}$ and $\Phi_{max,phase}$ of the particular phase in consideration, is sampled. The calculated averages and pair correlation functions are insensitive to the exact values of $\Phi_{min,phase}$ and $\Phi_{max,phase}$ chosen, as both of them will lie close to the corresponding local maximum in the Landau free energy function. The region around the local maximum in the Landau free energy corresponds to low probability configurations that have negligible contributions to the average value of the thermodynamic property in question.

The systems studied here are summarized in table 5.1. The Landau free energy functions are plotted for four different models of the pore walls in figure 5.1. The minimum that occurs at the values of order parameter near zero corresponds to the liquid phase. The minimum close to an order parameter value of 1.0 corresponds to the crystalline phase. For certain pore models an intermediate phase lies between the liquid and the crystalline phase. The temperature in each case is chosen such that the free energy difference between the intermediate phase and the liquid phase or the crystalline phase (which ever has a lower free energy) Δ_{min} is a minimum.

$$\Delta_{min} = \text{Min}\{\Omega_{int} - \Omega^*\}_T \tag{5.1}$$

$$\Omega^* = \Omega_{cry} \text{ if } \Omega_{cry} < \Omega_{liq}$$

$$\Omega^* = \Omega_{liq} \text{ if } \Omega_{liq} < \Omega_{cry}$$

In equation 5.1 "liq", "cry" and "int" refer to liquid, crystal and intermediate phases respectively and the function $\text{Min}\{f\}_T$ minimizes f with respect to T.

For repulsive and weakly attractive walls, the intermediate phase is at best metastable. For strongly attracting walls, the intermediate phase exists as a thermodynamically stable phase for a certain range of temperatures. The plot of Δ_{min}

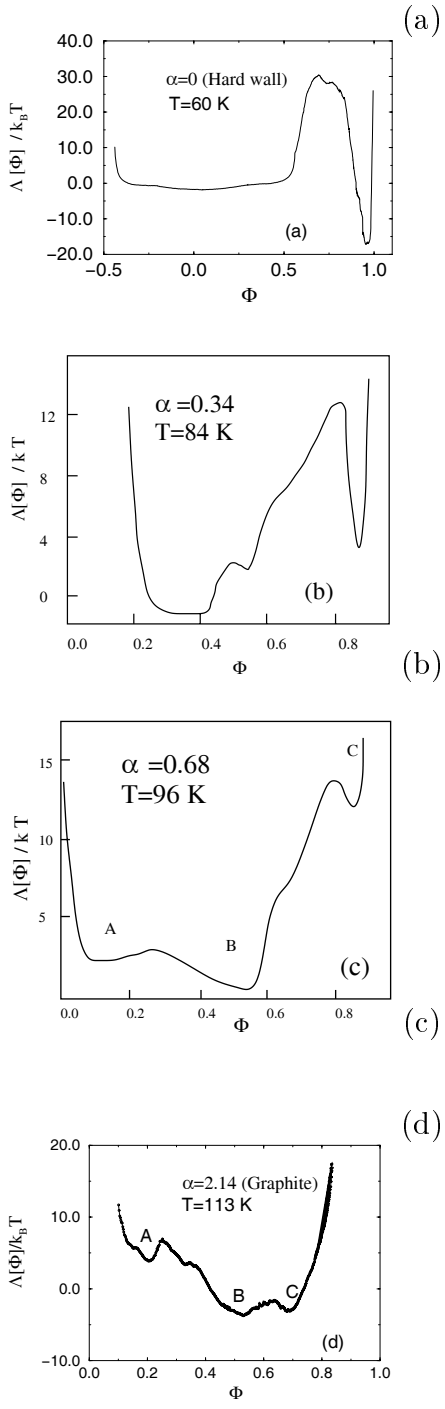

Figure 5.1: The Landau free energy as a function of the order parameter for LJ methane in different pore models with (a) $\alpha = 0$ at $T = 60$ K, (b) $\alpha = 0.34$ at $T = 84\ K$, (c) $\alpha = 0.68$ at $T = 96\ K$, (d) $\alpha = 2.14$ at $T = 113\ K$.

versus the relative strength of the fluid-wall to the fluid-fluid interaction α is shown in figure 5.2. For values of α less than 0.48, Δ_{min} is always positive, and thus only two thermodynamically stable phases exist, liquid and crystalline. For values greater than 0.48, three stable phases exist in the system. For the case of the purely repulsive pore, the disordered phase exists as a three dimensional liquid and the ordered phase is a fcc crystal. The increase in α value for the pore model induces layering in the system, distinct molecular layers forming parallel to the plane of the pore walls. In these cases the individual molecular layers exist as a quasi-two-dimensional liquid in the disordered phase and as two-dimensional hexagonal crystal in the crystalline phase. The intermediate phase is a partially ordered phase. In the case of a weakly attractive pore, the contact layers (i.e., the layers adjacent to the two pore walls) are liquid-like while the inner layers are crystalline (see figure 5.3(a)); thus the contact layers freeze at a lower temperature compared to the inner layers. For the case of a strongly attractive pore, the intermediate phase is characterized by crystalline contact layers and liquid-like inner layers; in this case the contact layers freeze at a higher temperature compared to the inner layers (figure 5.3(b)). The reversal of the freezing behavior of the contact layers occurs for α values between 0.85 and 1.15. The crossover of the branches of the grand free energy of the liquid, intermediate and the crystal phases determines the freezing temperature of the contact layers as well as the inner layers. The values of the freezing temperature as a function of the strength of the fluid-wall interaction parameter α are summarized in table 5.1. The bulk freezing temperature of LJ methane is 101.4 K. It is also observed that for weakly attractive pores ($\alpha < 0.85$) there is a depression in the freezing temperature and for strongly attractive pores ($\alpha > 1.15$) there is an elevation in the freezing temperature, when compared to the bulk.

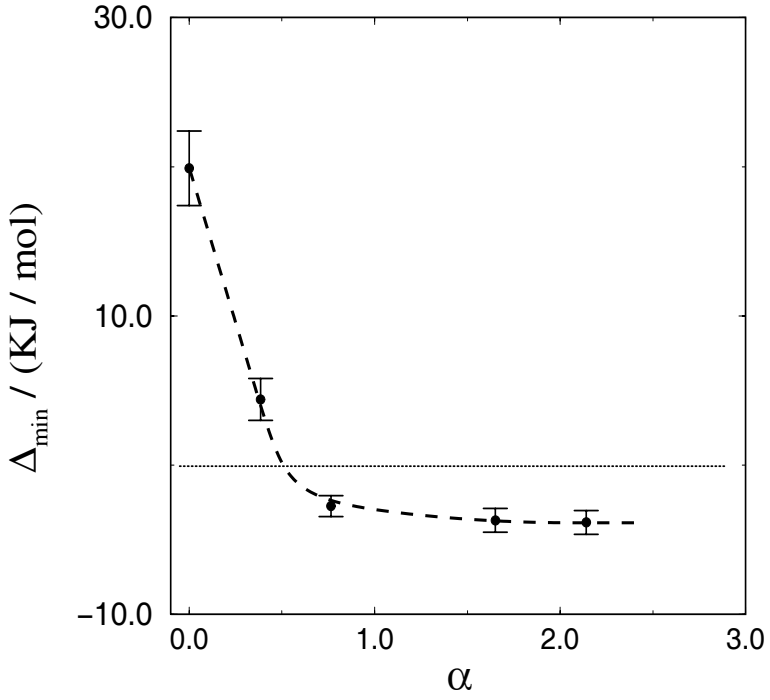

Figure 5.2: The plot shows Δ_{min} as a function of α. Regions with negative values of Δ_{min} correspond to the presence of a thermodynamically stable intermediate phase in the system

Table 5.1: Summary of Pore Models & Freezing Temperatures

Pore Wall Model	Wall Strength, α	T_f/K, contact layers	T_f/K, inner layers
Bulk	-	-	101.4
Model 1	0	-	48.0
Model 2	0.34	66.0	74.0
Model 3	0.68	78.0	86.0
Model 4	0.85	109.0	103.0
Model 5	1.65	120.0	109.0
Model 6	2.14	123.0	113.9

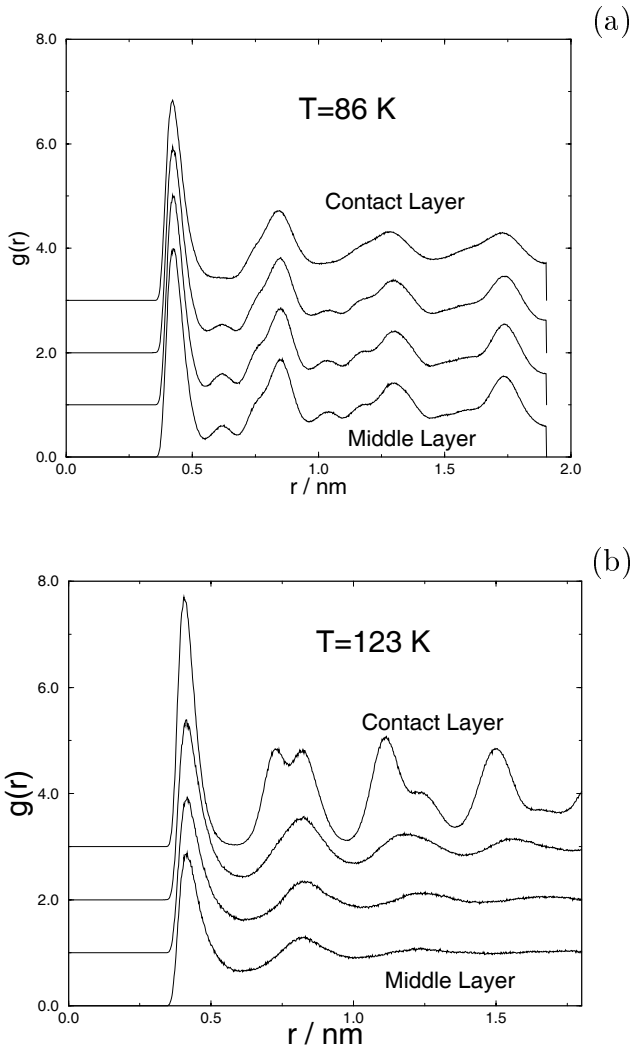

Figure 5.3: Plot shows 2-d, in-plane pair correlation functions in the molecular layers corresponding to the intermediate phase for LJ methane in a (a) weakly attractive pore ($\alpha = 0.68$, $T = 86$ K) and (b) strongly attractive pore ($\alpha = 2.14$, $T = 123$ K).

For a LJ fluid confined in a slit pore having a continuum "10-4-3" potential walls, the configurational partition function in the canonical ensemble $Q_{\text{config}}(N, V, T)$, is given by,

$$Q_{\text{config}} = \int_0^V d\vec{r}_i^{\,N} \exp\left(-\frac{1}{T^*} f(\vec{r}_i^{\,N}) - \frac{\alpha}{T^*} g(\vec{r}_i^{\,N})\right) \tag{5.2}$$

where the integration is over all $\vec{r}_i$, i.e., $\vec{r}_1, \vec{r}_2, \vec{r}_3$ etc., N is the number of molecules in the system, V is the volume of the system, $\vec{r}_i$ represents the spatial coordinates of molecule i, 'f' accounts for the fluid-fluid interaction and 'g' accounts for the fluid-wall interaction. Thus,

$$Q_{\text{config}} = Q_{\text{config}}[N, V^*, T^*, \alpha, \sigma_{ff}, \sigma_{fw}] \tag{5.3}$$

Typical fluid and pore systems have similar σ_{ff} and σ_{fw} values for small adsorbate molecules, and for a narrow range of these size parameters, g is a weak function of σ_{ff} and σ_{fw}. Thus, from the principle of corresponding states [103], to a good approximation for small adsorbates,

$$\Lambda^* \approx \Lambda^*[N, V^*, H^*, T^*, \alpha] \text{ and,} \tag{5.4}$$

$$T_f^* \approx T_f^*[H^*, \alpha]$$

For a LJ fluid confined in a model slit pore with "10-4-3" potential, equation 5.4 implies that the complete phase behavior including the freezing temperature is predictable from the knowledge of the Landau free energy as a function of the order parameter and temperature. The value of α together with results such as those in figure 5.1, in reduced variables, can be used to predict the freezing properties of the particular LJ system under consideration.

In order to predict the freezing properties of realistic fluid/pore systems, the respective fluid-fluid and fluid-wall interactions are approximated using the LJ potential and the slit pore model. The LJ parameters for the fluid are chosen to

Table 5.2: Potential energy parameters for fluid-fluid interactions

Fluid	LJ parameters σ_{ff}/nm, $\epsilon_{ff}/(k_B K)$	Property fitted
Simple fluids		
Ar	3.4, 119.8	2^{nd} Viral Coeff.
Kr	3.6, 171.0	2^{nd} Viral Coeff.
Xe	4.1, 222.0	2^{nd} Viral Coeff.
N_2	3.7, 96.0	2^{nd} Viral Coeff.
CH_4	3.8, 148.1	2^{nd} Viral Coeff.
CO_2	4.4, 192.0	2^{nd} Viral Coeff.
CCl_4	5.1, 366.0	Freezing point
Dipolar fluids		
HCl	3.3, 360.0	viscosity
HI	4.1, 324.0	viscosity
$C_6H_5NO_2$	5.7, 425.0	Freezing point
H-Bonding fluids		
NH_3	2.6, 711.0	2^{nd} Viral Coeff.
H_2O	3.2, 888.0	2^{nd} Viral Coeff.

reproduce thermophysical data (second virial coefficients or viscosity) of the bulk gas. The pore model parameters, $\sigma_{ww}, \epsilon_{ww}, \rho_w \& \Delta$, are chosen such that molecular simulation results of adsorption of LJ nitrogen matches the experimental results at 77 K. Based on the fitted potential parameters, the calculated value of α is used to predict the freezing temperatures of the contact layers as well as that of the inner layers, and also the structure of the confined fluid in various phases. Three different categories of fluids were chosen: simple fluids, dipolar fluids and hydrogen bonding fluids. The LJ parameters that represent the fluid-fluid interaction for these fluids are given in table 5.2. For dipolar and hydrogen bonding fluids the approximation of the fluid-fluid interaction by a LJ potential is a drastic one, however, the predicted freezing behavior is expected to be qualitatively correct. Two different models of slit pores are considered: a strongly attractive pore with interaction parameters chosen to model graphitic carbon pores, and a weakly attractive pore modeled on silica walls. The size parameter σ_{fw} to be used in the 10-4-3 potential is taken to be $(\sigma_{ff} + \sigma_{ww})/2$. For simple fluids, the energy parameter ϵ_{fw} is calculated as $(\epsilon_{ff}\epsilon_{ww})^{0.5}$, consistent with the Lorentz-Berthlot mixing rule. For dipolar and hydrogen bonded fluids, the LJ fluid-fluid parameters given in table 5.2 include, in some approximate, averaged fashion, the effects of direct electrostatic and induction interactions. The use of the ϵ_{ff} values given in table 5.2 in the Lorentz-Berthelot rule, $(\epsilon_{ff}\epsilon_{ww})^{0.5}$, to estimate ϵ_{fw} is therefore not appropriate. We expect direct electrostatic and induction interactions between such fluid molecules and the wall to be small, and we therefore neglect them. The LJ fluid-wall energy parameter is taken to be,

$$\epsilon_{fw} = (\epsilon_{ff}^{\text{dispersion}} \times \epsilon_{ww})^{1/2} \tag{5.5}$$

where $\epsilon_{ff}^{\text{dispersion}}$ is the LJ parameter value that represents only the dispersion

contribution. For HCl, HI, $C_6H_5NO_2$ and NH_3, the values of $\epsilon_{ff}^{\text{dispersion}}$ fitted to the Stockmayer potential [104] were used in equation 5.5, while for H_2O the value fitted to the SPC-E model was used. These values are given in table 5.3. Interaction parameters that characterize the pore walls are given in table 5.4.

The global freezing diagram for typical fluid/pore systems is given in figure 5.4. Each fluid is placed on the vertical axis depending on the porous material in which it is confined and the α value. The systems that lie in region 1 ($\alpha > 1.15$), show an elevation in the freezing point and are characterized by an intermediate phase with frozen contact layers and fluid-like inner layers. Systems with larger values of α have a larger elevation in freezing temperature. The systems that lie in region 2 ($0.5 < \alpha < 0.85$), show a depression in the freezing point behavior and have an intermediate phase with fluid-like contact layers and frozen inner layers. The systems that lie in region 3 ($\alpha \leq 0.5$) also show a depression in freezing point but they are characterized by an intermediate phase that is metastable. Thus, these systems have only two true thermodynamic phases (liquid and crystalline solid). In regions 2 and 3, smaller values of α lead to larger magnitude of the depression in the freezing temperature. The dashed line represents the boundary between regions 2 and 3. The boundary that separates regions 1 and 2 extends between the two dotted lines. Thus, systems falling in this boundary region can either show a depression or an elevation in the freezing temperature on confinement but the magnitude of the shift will be close to zero.

Table 5.3: Fluid-fluid interaction parameters used to calculate the fluid-wall interactions

Fluid	model	parameters
Simple fluids		σ_{ff}/nm, $\epsilon_{ff}^{\text{dispersive}}/(k_B K)$
Ar	LJ	3.4, 119.8
Kr	LJ	3.6, 171.0
Xe	LJ	4.1, 222.0
N_2	LJ	3.7, 96.0
CH_4	LJ	3.8, 148.1
CO_2	LJ	4.4, 192.0
CCl_4	LJ	5.1, 366.0
Dipolar fluids		σ_{ff}/nm, $\epsilon_{ff}^{\text{dispersive}}/(k_B K)$, μ/Debye
HCl	Stockmayer	3.3, 327.0, 1.03
HI	Stockmayer	4.1, 324.0, 0.1
$C_6H_5NO_2$	Stockmayer	5.7, 265.0, 4.2
H-Bonding fluids		
NH_3	Stockmayer	2.6, 320.0, 1.5
H_2O	SPC-E	3.2, 75.0, charges

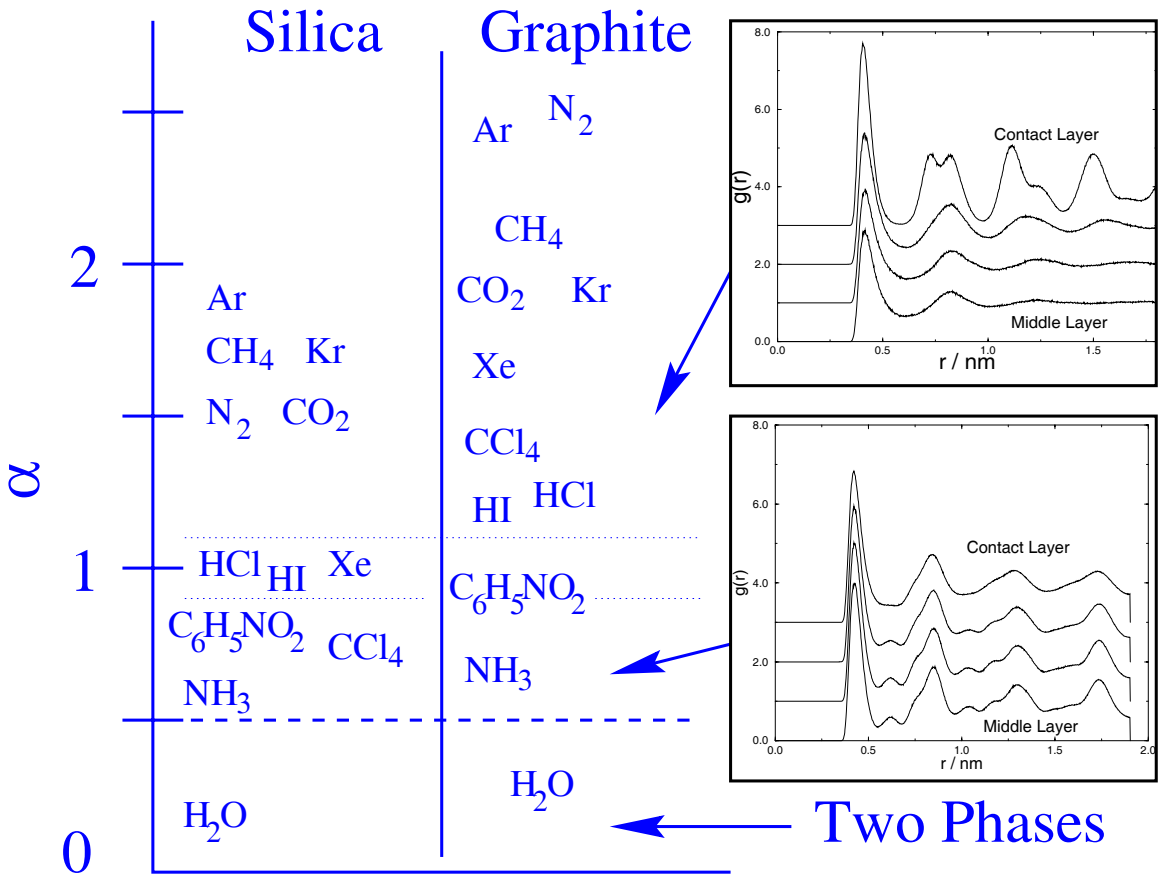

Figure 5.4: The figure represents the global freezing diagram for typical fluids confined in silica and graphite based pores. The different regions in the plot have different phase behavior. Fluid-pore systems that belong to region 1 ($\alpha > 1.15$) show an elevation in freezing temperature when compared to the bulk, while those in regions 2 ($0.5 < \alpha < 0.85$) and 3 ($\alpha \leq 0.5$) show a depression in freezing temperature. The pair correlation function plots show the fluid structure of the intermediate phase corresponding to the particular region.

Table 5.4: Potential energy parameters for the pore walls

Pore Wall Model	$\sigma_{ff}/\mathring{A}$, $\epsilon_{ww}/(k_BK)$	$\rho_s\sigma_{ww}^3$, $\Delta/\mathring{A}$
Graphite	3.81, 28.0	2.5, 3.3
Silica	2.7, 230.0	0.87, 2.2

5.4 Discussion

The global freezing diagram (figure 5.4) predicts the freezing temperatures of the contact and the inner layers and the confined fluid structure in the different phases for a variety of fluids in slit pores with model parameters to suit silica and graphite interactions. It is clear that the strength of the fluid wall interaction relative to the fluid-fluid interaction (α) plays a very important role in determining the freezing temperature as well as the structure of the confined fluid. The estimates of the freezing temperature for many systems are to be regarded as approximate, because of the simplicity of the pore models and the interaction potentials used to predict the phase diagram. The comparison between simulation and experiment is expected to be in nearly quantitative agreement for the case of simple fluids in graphite pores, for which the pore model and interaction potentials are best suited. In the case of polar and H-bonding fluids, approximating the fluid-fluid potential as LJ can lead to quantitative differences; however we expect qualitative agreement with experiment. For the case of silica based pores, the freezing temperature in figure 5.4 is expected to be an over estimation of the actual experimental values, as most silica based porous materials (CPG, VYCOR, MCM-41 etc.) have cylindrical pore geometry instead of slit pore geometry. The additional confinement due to the cylindrical geometry has

the same effect as reduction in α values, due to additional steric constraints on the formation of the confined crystal phase [105, 102].

Experimental studies have been reported that confirm the predictions of the global freezing diagram. Radhakrishnan et al. [80, 81] studied freezing of CCl_4 in activated carbon fibers using differential scanning calorimetry, and observed a large increase ($57\ K$) in the freezing temperature of the confined fluid compared to the bulk, which is consistent with the predictions of figure 5.4. Other experimental reports on freezing of CCl_4 in CPG and VYCOR pores (silica glasses) using DSC [2] find a depression in the freezing temperature when compared to the bulk. These trends are consistent with the weak potential of interaction experienced by the CCl_4 molecules due to the silica walls, and agree qualitatively with the predictions of the global phase diagram. The authors also studied freezing of nitrobenzene in silica based pores using dielectric relaxation spectroscopy (DS) [2] and found similar trends on the depression of the freezing temperature, that again confirms to the predictions of the global phase diagram. In addition to the freezing temperature, the DS measurements of the rotational relaxation times of the dipolar molecules also showed that the contact layers have different dynamic and structural properties compared to the pore interior. The authors found that the freezing temperature of the contact layers (as measured by the jump in the value of the dielectric relaxation time) was less than that of the inner layers (as measured by the jump in the value of the dielectric constant [102, 106]). This behavior implies that the structure of the confined intermediate phase in the silica based pores is the same as that of the intermediate phase described by figure 5.3(a). Following the study of Sliwinska-Bartkowiak et al. [2], we performed dielectric relaxation spectroscopy studies on the freezing of nitrobenzene in activated carbon fibers. Due to the conducting nature of the pore

material, the electrodes were blocked using a thin film of teflon before studying the frequency response. The experimental procedure is outlined in section 5.2, and in more detail in Ref. [2]. A plot of the dielectric relaxation times as a function of temperature is shown in figure 5.5 for nitrobenzene confined in the micropores of the ACF material. The bulk melting temperature for nitrobenzene is 5.6 Celsius and is denoted by the dashed vertical line. For the confined fluid, the corresponding freezing and melting temperatures are 3 Celsius and 8 Celsius respectively, as seen from the discontinuities in values of the dielectric relaxation times during the freezing and melting runs. We can therefore conclude that the shift in the freezing temperature due to confining the nitrobenzene molecules in ACF is nearly zero in the experiments, which is consistent with the predictions of figure 5.4. Figure 5.4 shows that the nitrobenzene/graphite system lies in the boundary of regions 1 and 2, and is therefore expected to have a very small shift if any in the freezing temperature due to confinement. We note that the relaxation times for the liquid in the confined system is much larger than the typical bulk liquid, because the measured relaxation time is that of the contact layers of nitrobenzene that experience a deep potential energy well due to the pore walls and hence are in a orientationaly ordered hexatic state [83, 107]. The relaxation times for the inner layers in their liquid state are in the range of nano-seconds, are outside the frequency range of our measurements. On freezing, the crystalline phase relaxation in the bulk as well as in the pore are of the order of milli-seconds [2, 102].

Experimental studies performed using the surface force apparatus are the most suited for direct comparison with the predictions of the global phase diagram. The surface force apparatus consists of two parallel plates with mica surfaces in which the spacing between the mica surfaces can be controlled at the scale of an angstrom

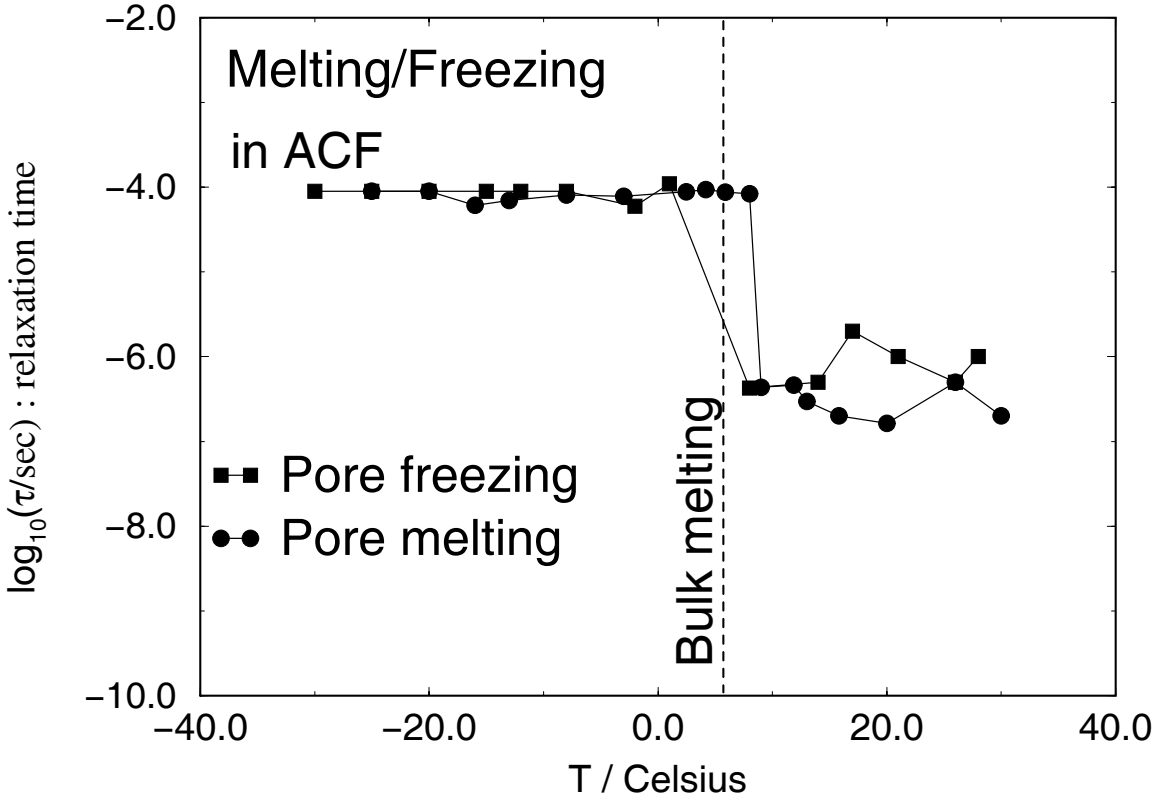

Figure 5.5: Relaxation time as a function of temperature for bulk nitrobenzene and nitrobenzene confined in activated carbon fibers

or less. Such a system can be modeled using the slit pore approximation as we have done in our study. Klein and Kumacheva [44] studied freezing of cyclohexane between parallel mica surfaces (slit shaped geometry) and observed a significant increase in the melting temperature on confinement. There has been contradicting reports on the nature of the shift in the freezing temperature of cyclohexane between parallel mica surfaces in a surface force apparatus [50]. However, a recent simulation study [108] based on the experimental system of Klein and Kumacheva, also predicted an elevation in the freezing temperature. The model parameters used to mimic the mica interaction in the study [108] yielded an α value of 2.47 for cyclohexane confined between the mica surface, which falls in region 1 in the global phase diagram (figure. 5.4), consistent with the elevation in the freezing temperature. A more convincing evidence that supports the verification of the global phase diagram is based on the experimental study of Watanabe et al. [82], which reported an elevation of freezing temperature for benzene confined in activated carbon fibers. The α value for a LJ benzene (fitted to reproduce the melting point of benzene in the bulk) in graphite is 2.15; thus, the freezing temperature elevation is again consistent with the global phase diagram.

In conclusion we comment on the methodology used to calculate the freezing temperature and characterize the phase behavior. The Landau free energy formalism was used to calculate the grand free energy of the fluid and crystalline states as a function of temperature, for LJ CCl_4 confined in slit-shaped pores. The free energy difference between the ordered and the disordered state is directly calculated. In addition to the free energy, a quantitative estimate of the free energy barrier to nucleation is obtained, although such a quantity is sensitive to system size effects. However, the absolute value of the free energy difference is only a weak function

of system size, and is estimated to an accuracy of $1k_BT$, as shown by Lynden-Bell et. al. [60] The exact location of the equilibrium transition temperature by free energy calculation is an improvement over methods that use the jump in the density to locate the freezing/melting points in terms of accuracy, as it is independent of the width of the hysteresis loops. Previously existing methods to calculate the free energy of a confined solid phase in simulations are all based on thermodynamic integration [51, 52]. This method involves a numerical integration of the Gibbs free energy starting from a known reference phase (the Einstein crystal for the solid phase and the ideal gas for the liquid phase) to the state point of interest. It relies on finding a suitable path of integration which is thermodynamically reversible, i.e., the path does not intersect any phase boundary characterized by a first order transition. Thus, the free energy study in Ref. [51] was limited to confined systems with repulsive or weakly attractive wall-fluid potentials (pore models for which $\alpha < 0.48$ so that the intervening intermediate phase is never a thermodynamically stable phase, hence the path of integration does not run into a first order phase transition). For the more ubiquitous case of a wall-fluid potential that is moderately or strongly attractive ($\alpha > 0.48$), this method breaks down. This is because the intermediate phase becomes a thermodynamically stable phase. This makes it impossible to find a reversible path from the ideal gas phase to the fluid phase, since any such path runs into a first order transition leading to the formation of the intervening intermediate phase. Thus one should exercise great caution in using the thermodynamic integration methods in confined systems (or inhomogeneous systems in general) because of the subtle phase transitions driven by the external potential that lead to formations of inhomogeneous phases that are thermodynamically stable. Such problems are circumvented by the use of the order parameter

formulation and the Landau approach.

The level of the Landau theory used in this study is still an approximation as it does not allow the order parameter to be explicitly spatially inhomogeneous. Instead, an average order parameter is used that takes into account the spatial fluctuations at a crude level but does not take into account the orientational fluctuations in the order parameter. In this sense, the field theoretic method used in this study comes under the general class of mean field approximations. This approximation is expected to give reliable and quantitative correct results in studying crystalline phases in which there is a very strong coupling between the phase of the orientational order parameters in different molecular layers, (since the order parameter Φ in equation 2.12 is a complex number it has a magnitude as well as a phase associated with it). This prevents spatial variations in the phase of the orientational order parameter. However, when studying other systems with hexatic order, the level of mean field theory used here fails to capture the spatial variations in the phase of the order parameter. In such cases a more generic form of the order parameter formalism (the Landau-Ginzburg approach) is more appropriate, as the free energy can be calculated as a function of the spatially varying order parameter [58] (see also chapter 6). The other main approximation in the methodology is the use of corresponding states theory in relation to freezing transitions. Although this principle is valid for the LJ model systems that we have used in this study, it should be noted that the global freezing diagram (figure 5.4) is based on equation 5.4, which is derived on the assumption that the Landau free energy function is a weak function of the LJ size parameters. Thus, the global freezing diagram is not expected to work very well for predicting the freezing temperatures of large molecules like butane and higher alkanes (nor for any other functional derivatives of these large molecules like

alcohols, amines etc.).

The corresponding states theory is known not to work as well with freezing transitions as with vapor-liquid transitions in real laboratory systems. The primary reason for the poor performance of the corresponding states theory for freezing transitions is the importance of three body effects in the formation of the crystalline phase; this is not captured by simple two-parameter models like Lennard-Jones [109]. However, the qualitative trends we have obtained from such a principle are still reliable, as the predictions are consistent with numerous experimental studies.

Chapter 6

On the Existence of a Hexatic Phase in Confined Systems

This chapter deals with an important extension of the Landau free energy methodology to rigorously treat spatial variations in the order parameter. This extension leads to the Landau-Ginzburg formalism that has been used to understand hexatic phases in confined systems.

Two- dimensional systems have a special significance for phase transitions in which continuous symmetry is broken (such as freezing transitions). The Mermin-Wagner theorem states that true long range order cannot exist in such systems [72]. Halperin and Nelson proposed the "KTHNY" (Kosterlitz- Thouless- Halperin- Nelson- Young) mechanism for melting of a crystal in two dimensions [70] which involves two transitions of the Kosterlitz-Thouless (KT) kind [73]: the first is a transition between the two- dimensional crystal phase (with quasi-long range positional order and long range orientational order) and a hexatic phase (with positional disorder and quasi-long range orientational order); the second transition is between the hexatic phase

and the liquid phase (having positional and orientational disorder). Each KT transition is accompanied by a non-universal peak in the specific heat above the transition temperature, associated with the entropy liberated by the unbinding of the vortex pairs. The crystal to hexatic transition occurs through the unbinding of dislocation pairs, and the hexatic to liquid transition involves the unbinding of disclination pairs. The hexatic phase was first observed experimentally in an electron diffraction experiment on liquid crystalline thin films [75, 77, 110]. In between the smectic-A phase and the crystal-B phase, a hex-B phase exists that possesses long range orientational order and positional disorder, as a result of which the diffuse electron intensity pattern displays a sixfold symmetry. The intensity pattern for a smectic-A phase is a uniform ring and that of the crystal-B phase has six Bragg peaks corresponding to a two- dimensional hexagonal lattice.

Extensive simulation studies on strictly two- dimensional systems have failed to provide compelling evidence to support the KTHNY melting scenario [74, 111]. Bladon and Frenkel [111] concluded that for almost all the systems studied in the simulations, the defect core energies of the vortices lie in a range such that the two- dimensional crystalline phase melts by a first order mechanism involving the induction and propagation of grain boundaries [74], rather than by the KTHNY mechanism. The authors [111] also showed that for systems that show a solid-solid transition (both the solid phases having the same symmetry and hence a critical point), the KTHNY mechanism would prevail as the mechanism of melting, in a finite region near the critical point. Zangi and Rice [112] argue that for quasi-two- dimensional systems that having a certain degree of out of plane motion, the conclusions of Frenkel and Bladon need modification. In particular, they point out that the presence of a solid-solid transition is not a necessity for observing the

KTHNY mechanism. Their simulation study shows strong evidence of a first order liquid to hexatic and a first order hexatic to crystal transition in a system without a solid-solid transition. The study by Zangi and Rice [112] has cast some light on the role of the *out of plane* motion (as in the case of a quasi-two- dimensional system as opposed to a strictly two- dimensional system) in stabilizing the hexatic phase.

Activated carbon fibers posses domains of micro-crystallites (made up of graphene sheets) that tend to align in similar directions, with slit shaped voids between the microcrystals. The spontaneous ordering of the molecules adsorbed in these voids into distinct two- dimensional molecular layers (analogous to the structure of a smectic-A phase in liquid crystals) makes the adsorbed phase a quasi-two- dimensional system with room for out of plane motions. Radhakrishnan and Gubbins [83] have studied freezing of Lennard Jones methane in slit-shaped carbon pores, and have reported the possibility of the existence of a confined hexatic phase of methane. The authors calculated the heat capacity of the system as a function of temperature and found KT-like peaks. Further, the two- dimensional in-plane structure factor $I(k_x, k_y)$ (equivalent to the intensity pattern in the electron diffraction experiment) showed a six-fold symmetry in the diffuse intensity pattern for the temperature range in which the peak in the heat capacity occurred, indicating the the onset of the hexatic transition.

In this article, we adopt a free energy approach to investigate the occurrence of the hexatic phase for Lennard Jones (LJ) CCl_4 confined in regular slit-shaped pores. Carbon tetrachloride is chosen as the adsorbate to make contact with recent experimental studies of this system. The fluid-wall potential was modeled to be of the form of the "10-4-3" Steele Potential, with parameters chosen to represent the

strongly attractive graphite pore [53]. The parameters for LJ CCl_4 were chosen to reproduce the bulk freezing temperature of CCl_4 at 1 atm. pressure ($\sigma_{ff} = 0.514$ nm, $\epsilon_{ff}/k_B = 366.1$ K). The carbon-CCl_4 unlike pair parameters were determined using the Lorentz-Berthlot mixing rules. The pore width $H = 2\sigma_{ff} + \sigma_{fw} = 1.41$nm, (where H represents the shortest distance between the planes passing through the carbon nuclei on the surface of the opposing pore walls) was chosen so that the adsorbed phase had 2 molecular layers of CCl_4. This choice of pore width was made to enable direct comparison with DSC measurements (that are described later) for CCl_4 confined in porous activated carbon fiber ACF A-10, of mean pore width $H = 1.4$ nm. The extent of the rectilinear simulation cell was $60\sigma_{ff} \times 60\sigma_{ff}$ (31 nm $\times$ 31 nm) in the xy plane so that correlations up to $30\sigma_{ff}$ can be captured in the simulations (the z coordinate is perpendicular to the plane of the pore walls). Periodic boundary conditions were used in the x and y dimensions. We expect the approximation of a structureless graphite wall to be a good one here, since the diameter of the LJ molecule (0.514 nm) is much larger than the C-C bond length in graphite (0.14 nm), so that CCl_4 molecules only feel a mild corrugation in the fluid-wall potential in passing along the surface. We extend the Landau free energy approach used in earlier studies [83, 60, 59] to incorporate *spatial inhomogeneity* in the order parameter, and develop the generalized Landau-Ginzburg approach to calculate the free energy surface of inhomogeneous fluids.

The Landau-Ginzburg formalism

The Landau-Ginzburg formalism involves choosing a spatially varying order parameter $\Phi(\vec{r}\,)$, that is strongly dependent on the phase of the system. The Landau free energy can be computed by a histogram method combined with umbrella sampling

that calculates the probability distribution of the system in the order parameter space. The probability distribution function $P[\Phi(\vec{r}\,)]$ is calculated during a simulation run by collecting statistics of the number of occurrences of a particular form of $\Phi(\vec{r}\,)$. This is accomplished by constructing a histogram with respect to Φ values in different domains obtained by discretizing the spatial coordinates. For the general case of a spatially varying order parameter $\Phi(\vec{r}\,)$, the probability $P[\tilde{\Phi}(\vec{r}\,)]$ is defined as,

$$P[\tilde{\Phi}(\vec{r}\,)] \;=\; \frac{1}{\Xi}\sum_{N=1}^{\infty}\frac{\exp\left(\beta\mu N\right)}{N!\lambda^{3N}}\int D_N[\Phi(\vec{r}\,)]\,\delta(\tilde{\Phi}(\vec{r}\,)-\Phi(\vec{r}\,))\,\exp(-\beta H_N) \qquad (6.1)$$

Ξ is the partition function in the grand canonical ensemble, N the number of molecules in the system, $\beta = 1/k_BT$, λ is the de Broglie wavelength and H_N is the Hamiltonian of the system. The path integral notation $D_N[\Phi(\tilde{\vec{r}}\,)]$ should be interpreted as [58],

$$\int D_N[\Phi(\vec{r}\,)] \;\equiv\; \lim_{v_o\to 0}\,\Pi_\alpha\int d\Phi_\alpha \;=\; \int_{\vec{r}^{\;N}} d\vec{r}^{\;N} \qquad (6.2)$$

Equation (6.2) defines the path integral in terms of a trace over a discrete number of sites α, and v_o represents the volume per site. The Landau free energy $\Lambda[\tilde{\Phi}(\vec{r}\,)]$ is then defined as,

$$\exp(-\beta\Lambda[\tilde{\Phi}(\vec{r}\,)]) \;=\; \sum_{N=1}^{\infty}\frac{\exp\left(\beta\mu N\right)}{N!\lambda^{3N}}\int D_N[\Phi(\vec{r}\,)]\,\delta(\tilde{\Phi}(\vec{r}\,)-\Phi(\vec{r}\,))\,\exp(-\beta H_N) \qquad (6.3)$$

From this definition it follows that,

$$\Lambda[\Phi(\vec{r}\,)] \;=\; -k_BT\,\ln(P[\Phi(\vec{r}\,)]) \;+\; \text{Constant} \qquad (6.4)$$

The grand free energy, $\Omega = -k_BT\,\ln(\Xi)$, is then related to the Landau free energy by,

$$\exp(-\beta\Omega) \;=\; \int D_N[\Phi(\vec{r}\,)]\,\exp(-\beta\Lambda[\Phi(\vec{r}\,)]) \qquad (6.5)$$

We use a two- dimensional bond orientational order parameter to characterize the orientational order in each of the molecular layers defined as follows:

$$\Psi_{6,j}(\vec{\rho}\,) \;=\; \frac{1}{N_b}\sum_{k=1}^{N_b}\exp(i6\theta_k)$$

$\Psi_{6,j}(\vec{\rho}\,)$ measures the hexagonal bond order at position $\vec{\rho}$ in the xy plane, within each layer j. The orientation of the nearest neighbor bond is fixed by the θ co-ordinate. The index k runs over the total number of nearest neighbor bonds N_b at position $\vec{\rho}$, in layer j. The order parameter $\overline{\Psi}_{6,j}$ in layer j is given by $\overline{\Psi}_{6,j} \;=\; |\int d\vec{\rho}\,\Psi_{6,j}(\vec{\rho}\,)|$. The positional pair correlation function is the same as the familiar radial distribution function. The orientational pair correlation function is given by $G_{6,j}(\rho) =< \Psi^*_{6,j}(0)\Psi_{6,j}(\rho) >$. For the case of LJ CCl_4 in slit-shaped pores, where there is significant ordering into distinct molecular layers, the order parameter $\Phi(\vec{r}\,)$ can be reduced to $\Phi(z)$ and can be represented by,

$$\Phi(z) \;=\; \sum_{j=1}^{n}\overline{\Psi}_{6,j}\,\delta(z-\hat{z}_j) \tag{6.6}$$

In equation (6.6), the sum is over the number of adsorbed molecular layers and $\hat{z}_j$ is the z coordinate of the plane in which the coordinates of the center of mass of the adsorbed molecules in layer j are most likely to lie on. It must be recognized that each of the $\overline{\Psi}_{6,j}$'s are variables that can take values in the range $[0,1]$. The histograms can be collected to evaluate the probability $P[\overline{\Psi}_{6,1},\overline{\Psi}_{6,2},...,\overline{\Psi}_{6,n}]$ as a function of the order parameters $\overline{\Psi}_{6,1},\overline{\Psi}_{6,2},...,\overline{\Psi}_{6,n}$. The grand free energy is then calculated using the equation,

$$\exp(-\beta\Omega) \;=\; \Pi_{\mathrm{j}=1}^{n}\int_j d\overline{\Psi}_{6,j}\,P[\overline{\Psi}_{6,1},\overline{\Psi}_{6,2},...,\overline{\Psi}_{6,n}] \tag{6.7}$$

Grand Canonical Monte Carlo simulations were used to study the freezing behavior of LJ CCl_4 in our model graphite pore. The number of molecules in the system

varied between 6000 and 7000. The state conditions in the simulations were chosen such that the confined phase was in equilibrium with bulk LJ CCl_4 at 1 atm. pressure. The simulations were started from a well equilibrated confined liquid phase at $T = 400$ K, and in successive simulation runs, the temperature was reduced. The two- dimensional, in-plane positional and orientational correlation functions ($g_j(r)$ and $G_{6,j}(r)$ of layer j), were monitored to keep track of the nature of the confined phase.

Results

Our results for the positional and orientational pair correlation functions for the two confined molecular layers of CCl_4 at three different temperatures are given in figure 6.1. It is evident from figure 6.1 that the high temperature phase at $T = 360$ K (isotropic $g(r)$ and exponentially decaying $G_{6,j}(r)$) is a liquid phase with short-range positional order and short-ranged orientational order. The confined phase at $T = 340$ K is characterized by an isotropic positional pair correlation function and an algebraically decaying orientational correlation function; this is a clear signature of the hexatic phase with short range positional order and quasi-long ranged orientational order. At $T = 290$ K the confined phase is a two- dimensional hexagonal crystal, with long-range positional order and long range orientational order.

The Landau free energy surface for this system is a function of two variables, $\Lambda/k_BT = \Lambda[\overline{\Psi}_{6,1}, \overline{\Psi}_{6,2}]/k_BT$. This function was calculated at two different temperatures, $T = 335$ K and $T = 290$ K, from which the grand free energies of the liquid (L), hexatic (H) and crystal (C) phases at these different temperatures were

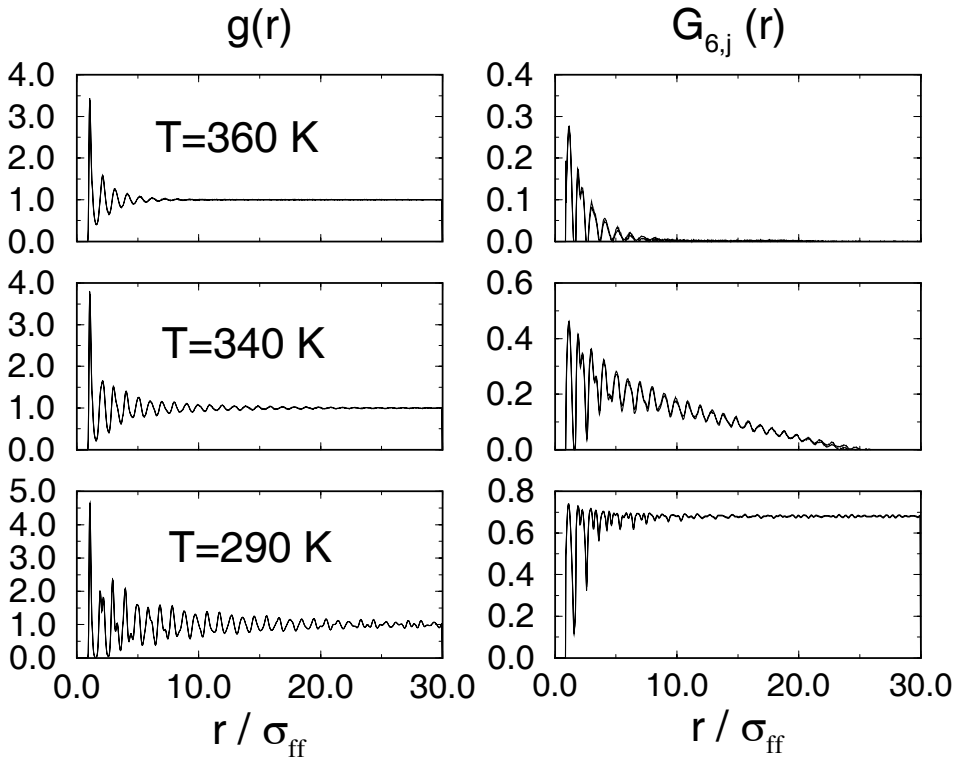

Figure 6.1: The positional pair correlation function $g(r)$ and the orientational pair correlation function $G_6(r)$ in the two molecular layers of CCl_4 confined in a graphite pore of width $H = 3\sigma_{ff}$ at three different temperatures, (a) liquid phase at $T =$ 360 K; (b) hexatic phase at $T = 340$ K; (c) Crystalline phase at $T = 290$ K.

calculated using equation (6.7). The grand free energy of the three phases at other temperatures were further calculated using thermodynamic integration [113], using the temperatures $T = 335$ K and $T = 290$ K as reference. The two grand free energy functions that were calculated using the two different reference temperatures were identical, which provided a test for self consistency of this procedure. The first order distribution function of the Landau free energy function for the first molecular (layer 1), $\Lambda^{(1)}[\overline{\Psi}_{6,1}]$ (which is obtained by the taking the functional derivative of equation (6.7) with respect to the order parameter $\overline{\Psi}_{6,1}$ in layer 1), at $T = 335$ K and $T = 290$ K is shown in figure 6.2.

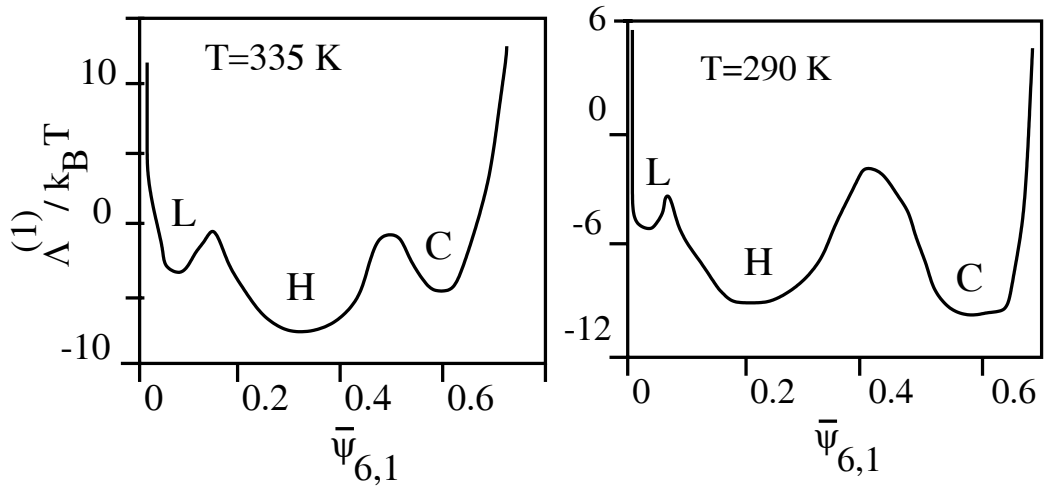

Figure 6.2: The first order distribution functions of the Landau free energy for layer 1 at $T = 335$ K and $T = 290$ K.

The distribution functions in figure 6.2 are good representations of the three dimensional Landau free energy surface for the system considered here because the fluid-wall potential energy is symmetric with respect to the two confined molecular layers of CCl_4, causing the matrix $\Lambda[\overline{\Psi}_{6,1}, \overline{\Psi}_{6,2}]$ to be symmetric. Further, the lowest free energy state points that govern the equilibrium thermodynamics of the system are given by the diagonal elements and the elements near the diagonal of the matrix.

The presence of the three phases ('L', 'H' & 'C') of the system is clearly seen in figure 6.2, along with their relative thermodynamic stabilities. It is clear from figure 6.2 that the hexatic phase is the thermodynamically stable phase at $T = 335$ K, while $T = 290$ K is close to the temperature at which the hexatic and crystalline phases coexist. The grand free energy function for the three phases ('L', 'H' & 'C') are given in figure 6.3. The cross-over of the free energy functions at $T = 347$ K and $T = 290$ K provide the transition temperatures of the liquid-hexatic and the hexatic-crystal transitions. The cross-over of the free energy of the different

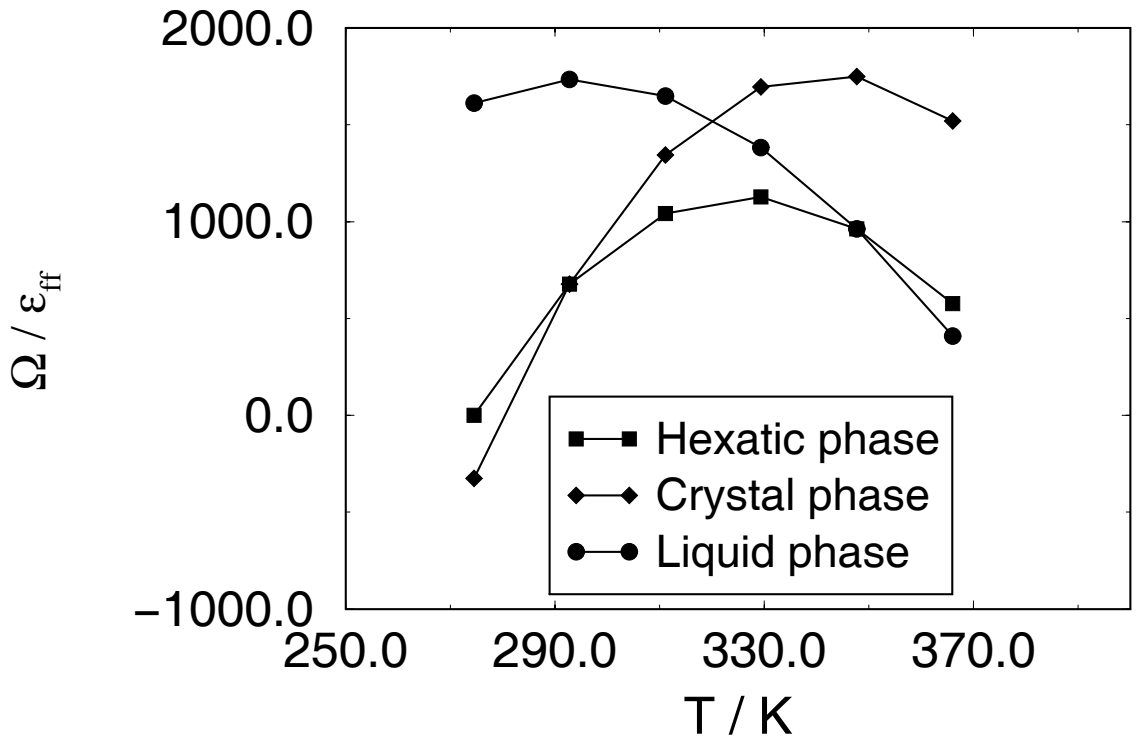

Figure 6.3: The Grand free energy as a function of temperature for liquid, hexatic and crystalline phases.

phases at different slopes at the transition temperatures imply that both transitions are first order for this particular system size. However, a system size study will be required in order to predict the order of these transitions in the thermodynamic limit.

In order to seek experimental evidence for a confined hexatic phase, we performed DSC measurements for CCl_4 confined in an activated carbon fiber (ACF A-10) porous material having a mean pore width of $H = 1.4$ nm. This carbon material is known to have slit-shaped pores having a narrow pore size distribution [80]. The CCl_4 was adsorbed in the porous medium at 1 atm. pressure. Figure 6.4 depicts such a DSC scan when the system was cooled; two peaks are present, the high temperature peak at $T = 345$ K is consistent with a liquid to hexatic transition in the confined

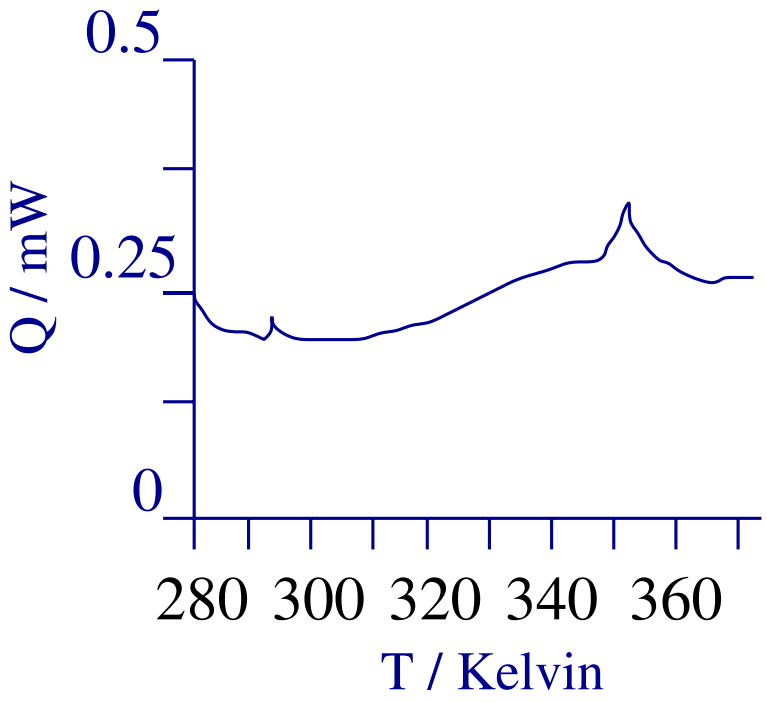

Figure 6.4: DSC scan for CCl_4 confined in activated carbon fiber ACF A-10 at a temperature scanning rate of 0.1 K/min.

phase and the smaller peak at $T = 290$ K is consistent with the hexatic to crystalline transition in the confined phase of CCl_4. Both the transition temperatures found in the DSC experiment lie within 3% of the simulation values. It must be remarked that the hexatic to crystalline phase transitions has a lower latent heat of transition when compared to the liquid-hexatic transition because much of the entropy is lost in the latter transition, which involves the pairing of free disclinations. The hexatic phase is a low entropy phase with a high degree of orientational ordering. Thus, a transition to the crystalline phase is accompanied only by a small change in entropy. Recently, Sliwinska-Bartkowiak has reported a similar behavior for the case of aniline confined in activated carbon fibers [114]. The DSC results are similar to figure 6.4, showing evidence of a liquid-hexatic and a hexatic-crystal transition. In addition, the dielectric permittivity measurements show two anomalies in the behavior of the dielectric constant vs. temperature at the same temperature range in which the peaks in the DSC spectrum are found. In conclusion, our simulation and experimental results are consistent with the KTHNY mechanism of melting. A final remark about the Landau-Ginzburg formalism is noteworthy. Although this is a rigorous approach for dealing with inhomogeneous systems, the results are only valid for a finite system size. Although we have verified that our results do not change for three system sizes, viz., $(10\sigma \times 10\sigma \times H)$, $(30\sigma \times 30\sigma \times H)$, $(60\sigma \times 60\sigma \times H)$, the largest system that we have studied contained up to 12000 molecules. Since the molecules are correlated over large length scales in the hexatic and crystalline phases, the finite extent of our simulation cell makes this study a mean field theory. In order to extrapolate our results to the thermodynamic limit requires systematic system size scaling analysis [78]. The self-consistency of our study can be established by estimating the Ginzburg parameter [58].

Chapter 7

Melting/freezing behavior in porous glasses and MCM-41

Sliwinska-Bartkowiak and co-workers [2] attempted to characterize the melting/freezing transition for a dipolar fluid, nitrobenzene confined in controlled pore glass of different pore sizes, using DSC and dielectric relaxation spectroscopy (DS). The depression in the melting temperature followed the Gibbs-Thomson equation for pore diameters larger than 7.5 nm; however, significant deviation was observed for a smaller pore width. The results from both experiments were in good agreement. The authors also made a quantitative estimate of the rotational relaxation time in the fluid and crystal phases by fitting the complex valued relative permittivity $\kappa^* = \kappa'(\omega) - i\kappa''(\omega)$ measurements to the Debye dispersion equation. In addition to the liquid and crystal phase relaxation, a third relaxation component was observed, that supported the existence of a contact layer with dynamic properties that were liquid-like but different from that of the inner layers; in particular the rotational relaxation times of molecules in the contact layer were about four orders of magnitude slower than molecules in the capillary condensed phase. Slower dynamics

of molecules in the contact layer were also reported by Takahara et. al. [115], in a neutron scattering study of water confined in MCM-41.

In an other study, Sliwinska-Bartkowiak et. al. [106] found evidence of a pre-freezing transition in nitrobenzene confined in a 7.5 nm CPG material that occurs before the confined fluid freezes into a single crystalline structure. The pre-freezing produces an intermediate phase, which we term the "contact layer phase", that is characterized by a positionally disordered contact layer but crystalline inner layers. For the system of nitrobenzene in CPG, the contact layer phase is only metastable because the melting occurs in a single step. This was also theoretically established by a study of Landau free energy surfaces using molecular simulation [106]. Recently Morishige and Kawano [116] found evidence of such a pre-freezing transition for methanol confined in MCM-41, using x-ray diffraction measurements. In a separate simulation study, Radhakrishnan et. al. [107] examined the thermodynamic stability of the contact layer phase as a function of the relative strength of the fluid-wall interaction to the fluid-fluid interaction. The authors concluded that the contact layer phase is metastable for repulsive and weakly attractive pore walls, and is a thermodynamically stable phase for strongly attracting pore walls.

The experimental and simulation studies, suggest that there is a need to characterize the structure of confined phases when studying freezing. Experimental studies involving x-ray diffraction and NMR methods, and the simulation studies involving free energies, establish the presence of stable inhomogeneous confined phases that bear important consequences for the nature of the phase transition as well as for the shift in the freezing temperatures. Although this effect has been understood in the case of simple fluids freezing in slit shaped pores, the nature of the confined phases

in the more complicated cases of sub-nanometer size cylindrical pores, and highly networked pores such as CPG and Vycor are still unknown.

This chapter primarily deals with the experimental measurements. The experimental studies are for carbon tetrachloride and nitrobenzene in controlled pore glass (CPG), VYCOR, zeolite MCM-41 and microporous activated carbon fibers ACF. Differential scanning calorimetry (DSC) was used to determine the melting point in the porous materials. Dielectric spectroscopy was also used to determine melting points. Structural information about the different confined phases was obtained by measuring the dielectric relaxation times using dielectric spectroscopy. Monte Carlo simulations, together with the Landau free energy method, are used to determine the melting point and fluid structure inside cylindrical pores modeled on silica. Qualitative comparison between experiment and simulation are made with respect to the shift in the freezing temperatures and the structure of confined phases. From the experiments as well as the simulations, it is found that, the confined fluid freezes into a single crystalline structure for average pore diameters greater than 15σ, where σ is the diameter of the fluid molecule. For average pore sizes less than 15σ, part of the confined fluid freezes into a frustrated crystal structure with the rest forming an amorphous region. The measurements and calculations show clear evidence of a novel intermediate "contact layer" phase lying between liquid and crystal; contact layer is the confined molecular layer adjacent to the pore wall and experiences a deeper fluid-wall potential energy compared to the inner layers. In addition, there is a strong evidence of a liquid to "hexatic" transition at high temperatures, in such a quasi-two-dimensional contact layer.

7.1 Methods

Liquid nitrobenzene and the CPG [117] and VYCOR [118] samples were treated by the same method as described in chapter 4. The MCM-41 samples were synthesized at A. Mickiewicz University at Poznan, Poland and were characterized using x-ray diffraction and nitrogen adsorption measurements [119]. The characterization results for the MCM-41 material showed that these crystalline materials consisted of uniform pores in a hexagonal arrangement with a narrow pore size distribution (less than 5%) [119].

7.1.1 Dielectric relaxation spectroscopy (DS)

The complex dielectric permittivity $\kappa^* = \kappa' - i\kappa''$, is measured as a function of temperature and frequency as described in chapter 4. In addition, the rotational relaxation times of the molecules were determined using the dispersion spectrum (equation 4.3)

7.1.2 Differential scanning calorimetry (DSC)

A Perkin-Elmer DSC7 (differential scanning calorimeter) was used to determine the melting temperatures and latent heats of fusion, by measuring the heat released in the melting of nitrobenzene. The temperature scale of the DSC machine was calibrated using the melting temperature of pure nitrobenzene from the literature. The temperature scanning rates used for the melting and freezing runs varied from 0.2K/min to 0.5K/min. The background of each raw DSC spectrum was subtracted, based on a second-order polynomial fit to the measured heat flow away from the signals of interest. The melting temperatures in the bulk and confined systems were

determined from the position of the peaks of the heat flow signals, and the latent heats were determined based on the scaled area under these signals. The melting temperature was reproducible to within 0.5 Celsius for larger pores ($\geq$25 nm); uncertainties were larger for the smaller pores. These uncertainties are a result of the width of the DSC peaks, which derives in part from variations in pore size, and geometry, and from the existence of metastable states. The latent heats were reproducible to within 5%.

7.1.3 Simulation

We performed grand canonical Monte Carlo (GCMC) simulations of Lennard-Jones CCl_4 adsorbed in straight cylindrical pores of different pore diameters. The interaction between the adsorbed fluid molecules is modeled using the Lennard-Jones (12,6) potential with size and energy parameters chosen to describe CCl_4 ($\sigma_{ff} = 0.514$ nm, $\epsilon_{ff}/k_B = 366.4$ K). The pore walls are modeled as a smooth LJ continuum [120] (the cylindrical equivalent of the"10-4-3" Steele potential). The fluid-wall interaction energy parameters corresponding to a silica pore were taken from Gelb and Gubbins [121].

The simulation runs were performed in the grand canonical ensemble, fixing the chemical potential μ, the volume V of the pore and the temperature T. The system typically consisted of 600-2000 adsorbed molecules. Periodic boundary conditions were employed in the axial dimension of the pore. The simulation was set up such that insertion, deletion and displacement moves were attempted with equal probability, and the displacement step was adjusted to have a 50% probability of acceptance. Thermodynamic properties were averaged over 100-1000 million individual Monte

Carlo moves. The length of the simulation was adjusted such that a minimum of fifty times the average number of particles in the system would be inserted and deleted during a single simulation run.

The method used to calculate the free energy relies on the calculation of the Landau free energy as a function of an effective bond orientational order parameter Φ, using GCMC simulations as described in chapter 2. Three dimensional bond orientational order parameters [65] that can differentiate between the isotropic liquid phase and common crystalline lattices are employed. These order parameters are defined in chapter 2.

7.2 Experimental results

7.2.1 Dielectric relaxation

The capacitance C and tangent loss $\tan(\delta)$ were measured as a function of frequency and temperature for bulk nitrobenzene and for nitrobenzene adsorbed in CPG, VYCOR and MCM-41 materials of different pore sizes, ranging from 50 nm to 2.4 nm, from which the dielectric constant $\kappa'(T,\omega)$ and the loss factor $\kappa''(T,\omega)$ were calculated. The dielectric constant is a natural choice of order parameter to study freezing of dipolar liquids, because of the large change in the orientational polarizability between the liquid and solid phases. The melting point can be taken to be the temperature at which there is a large increase in the permittivity, as the solid phase is heated. The measurements of κ' as a function of T are shown in figure 7.1(a) for bulk nitrobenzene. There is a sharp increase in κ' at $T = 5.6\ ^{\circ}\mathrm{C}$, corresponding to the melting point of the pure substance. The spectrum of the

complex permittivity (κ', κ'' vs. ω) is fit to the dispersion relation (equation (4.3)), to determine the dielectric relaxation time τ. The frequency range in this study (100 Hz to 10 MHz) is expected to encompass the resonant frequencies corresponding to the dielectric relaxation in the solid phases and glass-like phases. According to equation (4.3), the κ' function shows a point of inflection and the κ'' function goes through a maximum at the resonant frequency. Therefore, from a spectrum plot of κ', κ'' vs. $\log_{10}(\omega)$, the relaxation time can be calculated as the reciprocal of the frequency corresponding to a saddle point of the κ' function or a maximum of the κ'' function. An alternative graphical representation of the Debye dispersion equation is the Cole-Cole diagram [93], in the complex κ^* plane. The Cole-Cole diagram falls on a semi-circle for each relaxation mechanism. From a plot of κ'' vs. κ', τ is given by the reciprocal of the frequency at which κ'' goes through a maximum.

Figure 7.1(b) depicts the variation of the relaxation time with temperature for bulk nitrobenzene, obtained from fitting the dispersion spectrum to equation (4.3). The liquid branch of the plot (above 6 $^{\circ}$C) has rotational relaxation times of the order of nano-seconds. This branch lies outside the range of our measurements and is reproduced from ref. [122]. The relaxation time shows a sharp increase at the melting temperature and is of the order of 10^{-3} s in the crystal phase.

For nitrobenzene confined in CPG, the sample is introduced between the capacitor plates as a suspension of nitrobenzene filled CPG particles in pure nitrobenzene. Therefore, the capacitance measurement yields an effective relative permittivity of the suspension of CPG in pure nitrobenzene. For a CPG sample with average pore diameter of 25 nm, κ' shows two sudden changes (figure 7.2). The sharp increase at 2 $^{\circ}$C is attributed to melting in the pores, while that at 5.6 $^{\circ}$C corresponds to the bulk melting. The frequency spectrum at a particular temperature is used to obtain

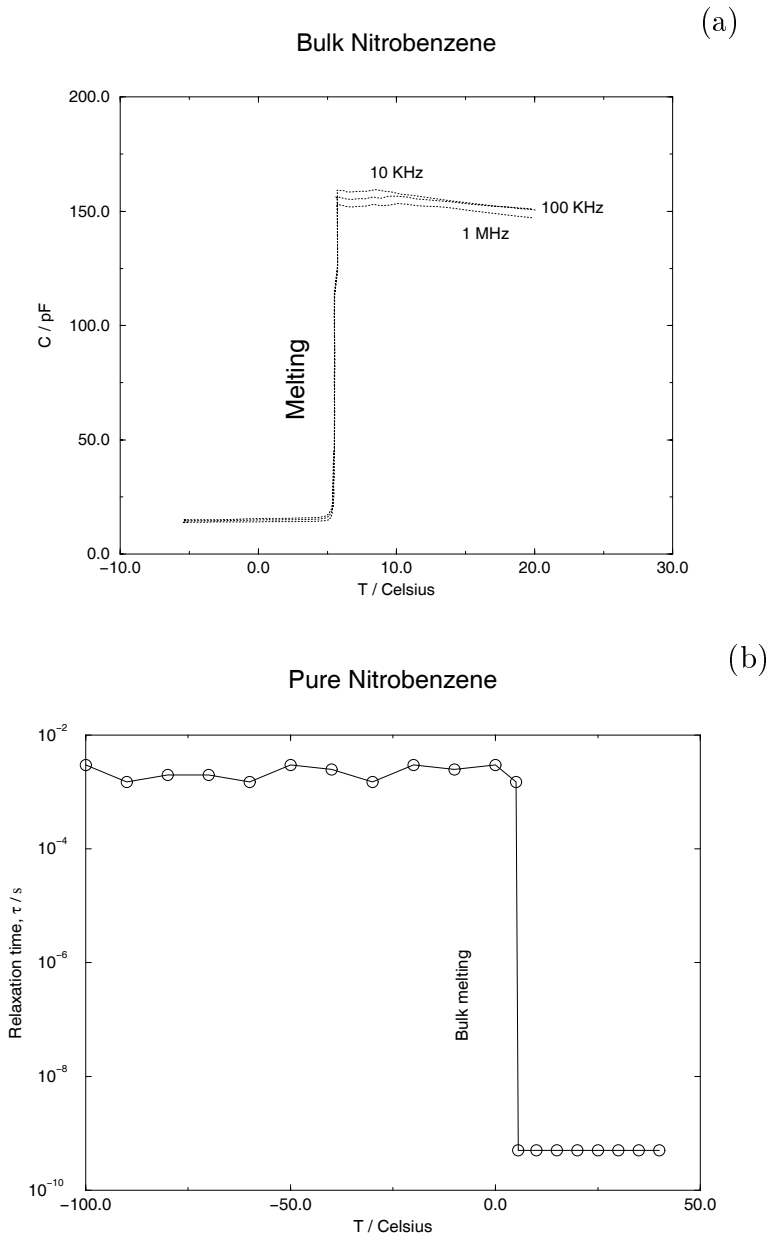

Figure 7.1: (a) The behavior of κ' vs. T for bulk nitrobenzene. The sharp increase at 5.6 $^{\mathrm{o}}$C corresponds to bulk melting. (b) Relaxation time vs. temperature for the bulk. At each temperature τ is estimated by fitting the dispersion spectrum to the Debye dispersion equation.

the orientational relaxation times in the different phases of the system as described before. For example, in figure 7.3 the spectrum plot (κ', κ'' vs. ω) is shown for nitrobenzene confined in the 25 nm CPG material at two different temperatures. The spectrum in figure 7.3(a) at 20 ^{O}C shows two relaxation mechanisms (as seen by the two inflection points in κ') with relaxation times of the order of 10^{-3} s (which we refer to as "millisecond relaxation") and 10^{-5} s (which we refer to "microsecond relaxation"). A similar spectrum at -10 ^{O}C (figure 7.3(b)) produces just one relaxation mechanism with a time scale of 10^{-3} s. The corresponding Cole-Cole diagrams are shown in figure 7.4. The response to each relaxation mechanism falls on a semi-circle in the Cole-Cole diagram. Therefore figure 7.4(a) confirms the two relaxation mechanisms at the higher temperature (20 ^{O}C) and the single relaxation mechanism at the lower temperature (-10 ^{O}C) is evident from figure 7.4(b).

7.2.2 Maxwell-Wagner Effect

The behavior of the relaxation times as a function of temperature for nitrobenzene in CPG of 25 nm pore size are depicted in figure 7.5. For temperatures greater than 2 ^{O}C (melting point inside the pores), there are two different relaxations similar to figure 7.3(a); they manifest themselves as a double inflection behavior in κ' vs. ω, and a double maximum in κ'' vs. ω. The longer component of the relaxation that is of the order of 5×10^{-3} s is because of Maxwell-Wagner-Sillars polarization. For a heterogeneous system there occurs a relaxation mechanism due to interfacial polarization, when a slightly conducting liquid is enclosed in an insulating material. This effect, called the Maxwell-Wagner-Sillars (MWS) polarization [99], is known to have a relaxation time of the order of 10^{-3} s [98, 100]. The CPG and Vycor samples used in this study were dielectrically neutral, in the sense that, in the temperature

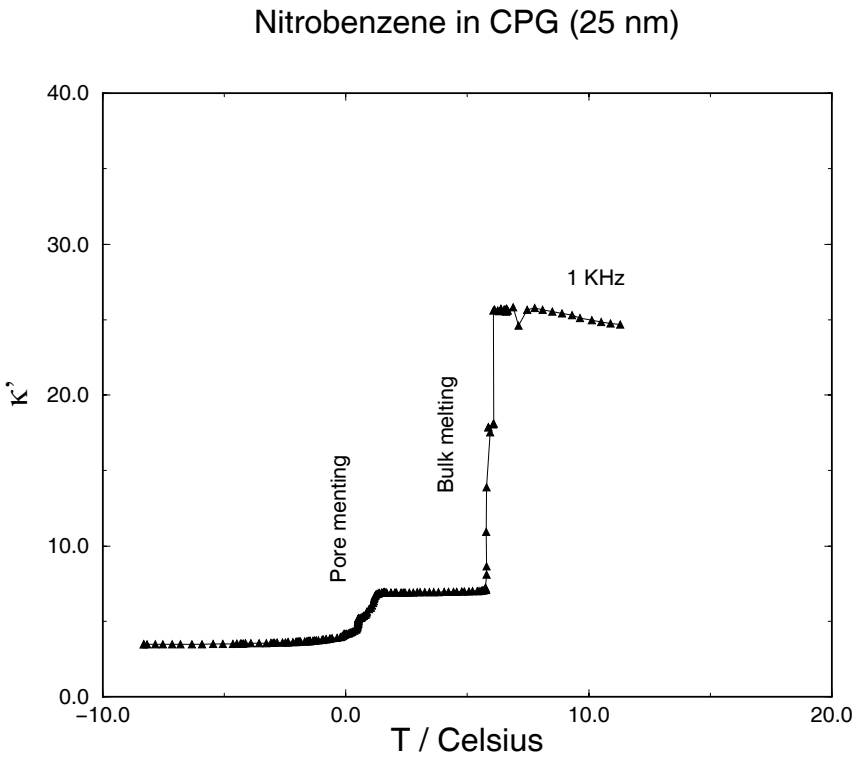

Figure 7.2: The behavior of κ' vs. T for nitrobenzene in a CPG material of average pore diameter of 25 nm. The sample is introduced as a suspension of porous glass particles in bulk nitrobenzene. Thus, the signals are for both bulk and confined nitrobenzene.

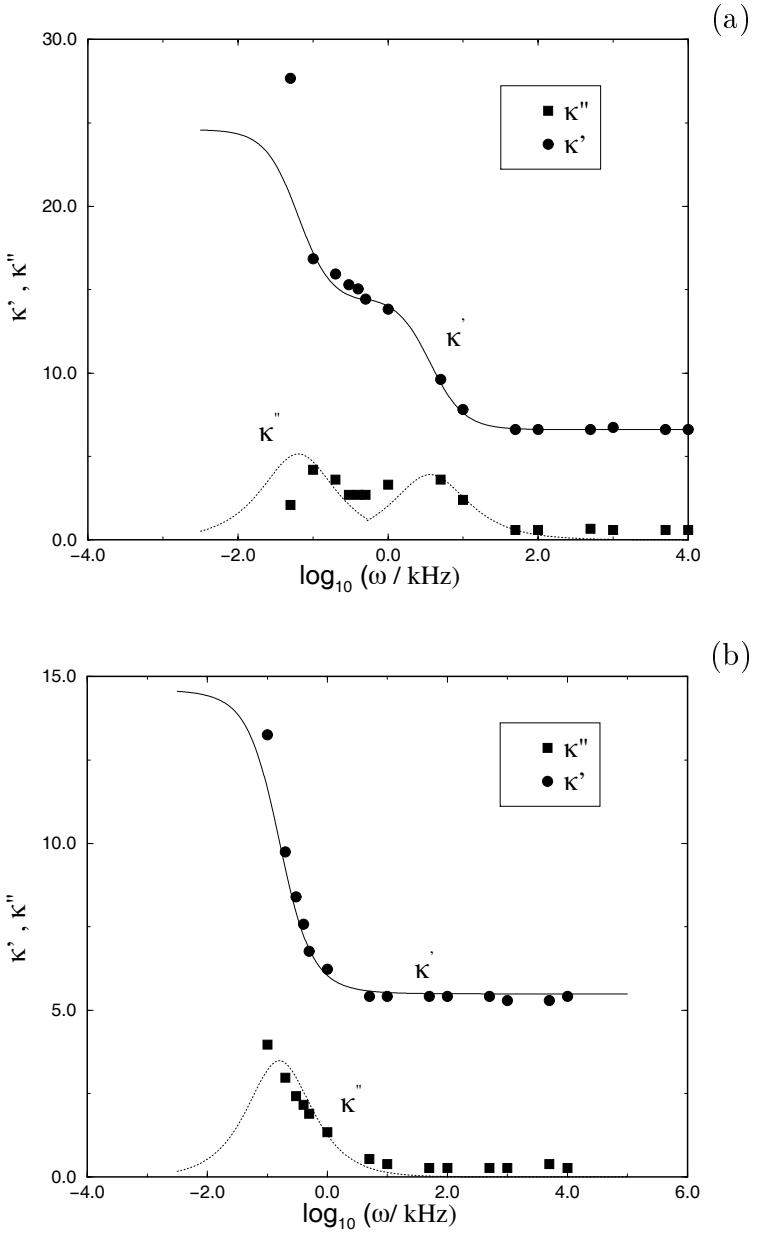

Figure 7.3: Spectrum plot for nitrobenzene in a 25 nm pore (a) at 20 ^{O}C, (b) at -10 ^{O}C. The symbols correspond to experimental measurements and the solid and the dashed curves are fits to the real and imaginary parts of equation 4.3 respectively.

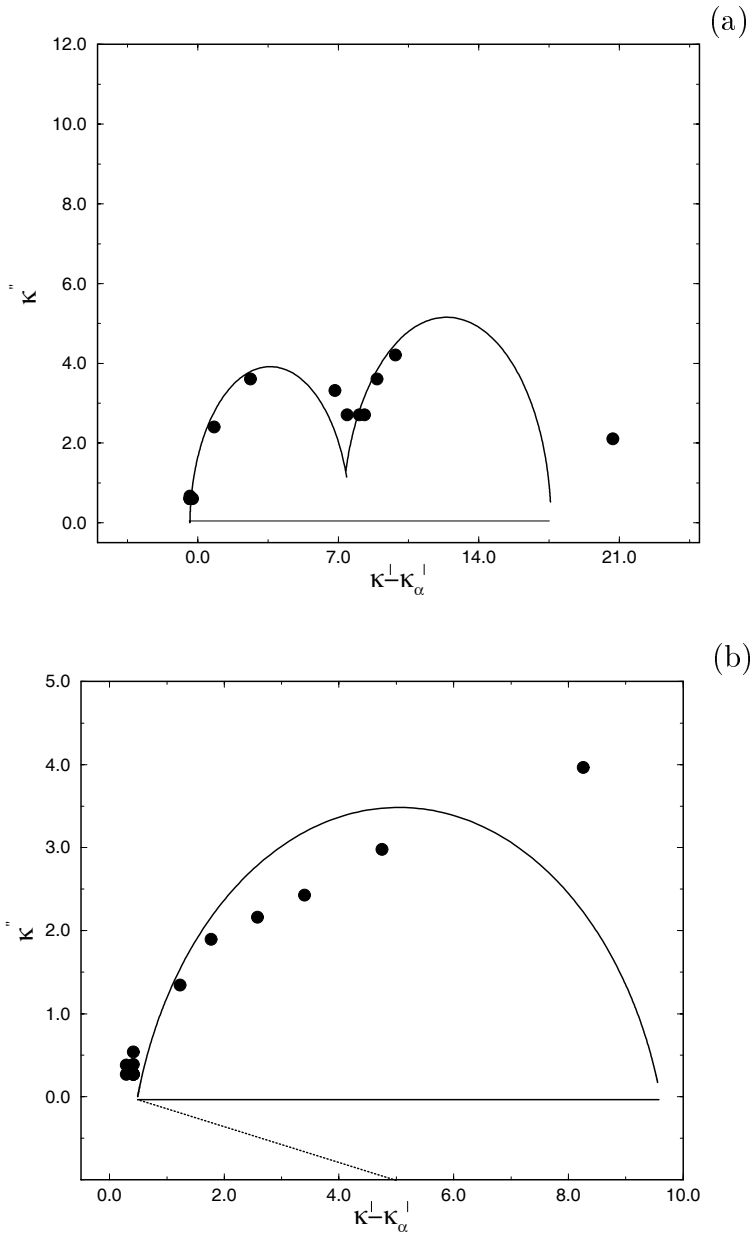

Figure 7.4: Representation of the spectrum plots in the form of a Cole-Cole diagram: (a) at T =20 $^{\mathrm{O}}$C, at $T = -10$ $^{\mathrm{O}}$C

and frequency range of our measurements, the dielectric loss (proportional to κ'') of the empty pores was negligible compared to that for the liquid-filled samples. Therefore, there is no background noise due to the motion of silica molecules. The shorter relaxation component, of the order of 50×10^{-6} s, is too slow to represent the liquid phase relaxation in the pore. However, it is known that for dipolar liquids confined in nano-scale pores, the molecules in the contact layer show a slower dynamics, with a relaxation time of the order of 10^{-5} s [98, 100, 101]. Thus, the shorter relaxation component is consistent with such a behavior of the contact layer. The Landau free energy calculation for methane and CCl_4 in graphite [83, 81] and for CCl_4 in silica [107], and the NMR study by Overloop and Van Gerven [38] dealing with water in porous silica also support the view that the molecules in the contact layer behave differently than the those in the pore interior. Thus, the 50×10^{-6} s branch of the relaxation time that occurs for temperature above 2 ^{O}C (figure 7.5), corresponds to the response of the contact layer. The response of the liquid phase in the bulk and the inner layers of the pore are not accessible in our experiments as sub-nanosecond relaxation times are not affected by the frequency range we use in our experiments. The disappearance of the 50×10^{-6} s branch of the relaxation time and the appearance of the 10^{-3} s branch at 2 ^{O}C, points to the freezing of the liquid in the pores. Below this temperature, the millisecond relaxation time (similar to figure 7.3(b) at -10 ^{O}C) corresponds to the crystal phase relaxation in the bulk and in the pore. The MWS effect disappears because the CPG particles are arrested in the crystalline matrix of bulk nitrobenzene, thereby preventing interfacial dispersion. Thus, from figure 7.2 and figure 7.5, the melting temperature of the fluid inside the pore is determined to be 2 ^{O}C.

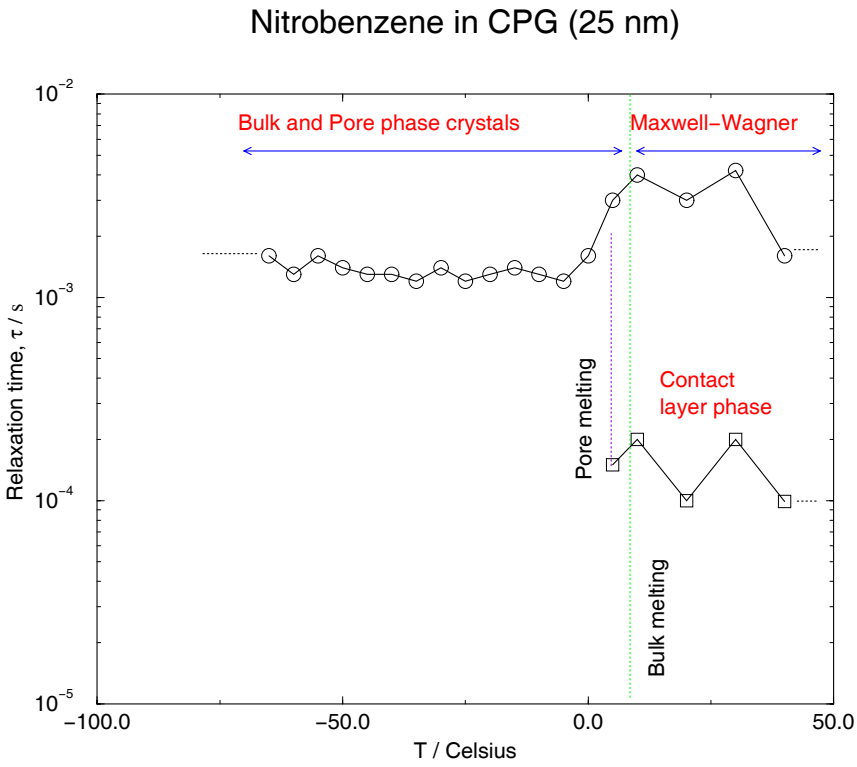

Figure 7.5: The behavior of κ' vs. T for nitrobenzene in a CPG material of average pore diameter of 25 nm. The sample is introduced as a suspension of porous glass particles in bulk nitrobenzene. Thus, the signals are for both bulk and confined nitrobenzene.

7.2.3 Contact Layer Phase

For fluid molecules such as nitrobenzene that wet the pore walls, the adsorbate molecules in the contact layer, layer next to the pore walls, feel a large attractive potential energy due to the combined interactions with all the molecules of the porous material. The density of the adsorbed molecules in the contact layer, is much higher than the bulk liquid density or the average density of the confined fluid phase. In addition, the locus of the surface defining this attractive potential energy is approximately a cylindrical shell, as the pores in CPG, Vycor and MCM-41 have a cylindrical shape. Such a cylindrical shell is quasi-two-dimensional in nature, (a cylindrical shell of radius R and length L, that is cut along a single line parallel to the axis, forms a rectangular two-dimensional plane of dimensions $2 \times \pi \times R$ by L). Due to the high density of the adsorbed nitrobenzene molecules in the quasi-two-dimensional contact layer, there is a possibility that the contact layer exists as a hexatic phase with a high degree of orientational ordering. In two-dimensional systems such a hexatic phase lies in between the disordered liquid phase and ordered crystalline phase. The hexatic phase is a manifestation of the fact that, in a continuous symmetry breaking transition such as the freezing transition, the translational symmetry and the rotational symmetry can break at two different temperatures [75]. Thus, in the liquid to hexatic phase transition, the rotational symmetry is broken and in the hexatic to crystalline transition the translational symmetry is broken. According to theory [69, 123, 70, 124], the hexatic phase occurs only for an infinite two-dimensional system, but finite systems such as the contact layer phase can show behavior reminiscent of infinite systems. The slower dynamics of the contact layer phase (with τ of the order of 10×10^{-6} s can be an attribute of its hexatic nature. Such a hexatic phase is predicted by computer simulation for

fluids confined in graphitic micropores such as activated carbon fibers, and verified by experiments [107, 83, 81]. For nitrobenzene confined in activated carbon fibers, Radhakrishnan et. al. [107] found that the nitrobenzene molecules in the hexatic phase have a dielectric relaxation time of the order of 1×10^{-6} s.

Surface heterogeneity can also play a significant role in governing the dynamics of the contact layer. Surface characterization studies of CPG, Vycor and MCM-41 [101, 125, 126] have reported that the silica surface is energetically heterogeneous in such materials. In particular, there is a large concentration of silanol (Si-O-H) on the pore surface, as large as 3 groups per nm^2 in silicious MCM materials [125]. This implies that among the nitrobenzene molecules that are present in the contact layer, a large fraction (as large as 75 %) can be weakly hydrogen bonded to the surface silanol groups. The difference in the dielectric relaxation times of the contact layer phase in the ACF micro pores ($\tau \sim 1 \times 10^{-6}$ s) and that of the contact layer phase in CPG, Vycor and MCM-41 ($\tau \sim 10 \times 10^{-6}$ s) is one order of magnitude. The additional H-bonding with the surface silanol groups in the silica based pores (CPG, Vycor and MCM-41) can explain the slower dynamics of the contact layer when compared to the ACF micropores, in which H-bonding is absent.

7.2.4 Effect of Pore-Size

In figure 7.6 is shown κ' and τ for the freezing of nitrobenzene in a 8.5 nm CPG material. The trends are qualitatively similar to that observed for the 25 nm pore. Figure 7.6(a) shows that the increase in κ' corresponding to the melting of nitrobenzene in the pores is much more rounded and occurs at a lower temperature compared to the bigger pores. From the relaxation time behavior in figure 7.6(b), we estimate

the melting temperature inside the pores to be -23 ^{o}C (the temperature below which the microsecond relaxation disappears). The 10^{-3} s branch of the relaxation time in figure 7.6(b) is divided into three regions. The response in the region, $T > 6$ ^{o}C is due to MWS polarization; $-23 < T < 6$ ^{o}C corresponds to the relaxation of the bulk crystal and $T < -23$ ^{o}C is due to the combined relaxation of the bulk crystal and the crystal inside the pores.

For average pore diameter $H \geq 8.5$ nm, the behavior of the relaxation time with temperature suggests that the crystalline phase in the pore is a homogeneous phase; i.e., molecules have a single relaxation component throughout the confined crystalline phase. For smaller pores however, e.g. Vycor with $H = 4.5$ nm, the behavior is quite different. Figure 7.7(a) shows that the increase in κ' with temperature is much more gradual and rounded for the melting of nitrobenzene in the pores. The bulk signal shows the usual sharp increase at 5.6 ^{o}C and is outside the range of the plot in figure 7.7(a). In figure 7.7(b) is plotted the corresponding relaxation times for nitrobenzene melting in Vycor glass. The microsecond branch of the relaxation time shows a sharp increase at $T = -40$ ^{o}C, which can be taken to be the melting temperature inside the pores. The millisecond branch is again divided into three regions, $T > 5.6$ ^{o}C (MWS polarization), $-40 < T < 5.6$ ^{o}C (bulk crystal phase) and $T < -40$ ^{o}C corresponding to the crystalline phase relaxations in the bulk and in the pore. However, there is a new branch of relaxation times of the order of a few hundred nanoseconds which occurs below the melting temperature of nitrobenzene in the pores ($T < -40$ ^{o}C). This strongly suggests that the confined crystalline phase in not homogeneous, but that there are regions that are glass-like (amorphous), having a relaxation component of the order of a few hundred nanoseconds. Thus for pore diameters as small as 4.5 nm, the confinement poses a serious

constraint on the formation of a homogeneous crystalline phase in the pore. The exact structure of the confined crystalline phase cannot be determined from dielectric relaxation spectroscopy experiments alone. One would need to resort to more direct methods, such as x-ray diffraction or molecular simulation, in order to obtain the fluid structure of the inhomogeneous crystalline phase.

In figures 7.8(a) and 7.8(b) the melting behavior of nitrobenzene in a MCM-41 porous material having an average pore diameter of 2.8 nm are shown. The qualitative behavior is different from the behavior in Vycor. The freezing transition at low temperature is absent as the microsecond branch of the relaxation time does not show any discontinuity. Once again there is a branch of relaxation times of the order of a few hundred nanoseconds, suggesting the presence of amorphous regions. We conclude that the pore size of 2.8 nm is too small so that partial crystallization does not occur. The contact layer remains in the orientationaly ordered "hexatic" phase, while the inner region undergoes a glass transition. A very similar behavior is observed for the case of nitrobenzene inside an MCM-41 material of pore diameter 2.4 nm. Table 7.1 summarizes the melting behavior of nitrobenzene for a range of pore sizes in various silica-based pores. Nitrobenzene freezes to a crystalline structure when confined in pore sizes $H \geq 8.5$ nm ($H \geq 17\sigma_{ff}$). For a pore size of 4.5 nm, only part of the fluid freezes, with the rest forming an amorphous phase. Morishige and Kawano [127] reached similar conclusions in their x-ray diffraction study of freezing of N_2, CO and Kr in MCM-41 materials of varying pore diameter. For these fluids, the x-ray structure indicated a homogeneous crystalline phase for pore diameters greater than 6 nm ($H \geq 16\sigma_{ff}$). For smaller pore sizes, the x-ray diffraction patterns were consistent with a partially crystalline confined phase coexisting with an amorphous phase. For pore sizes smaller than 2.8 nm, the confined

(a)

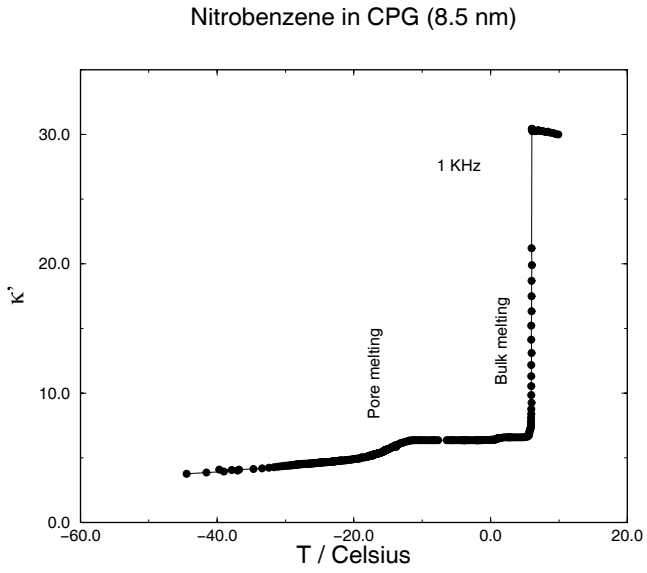

(b)

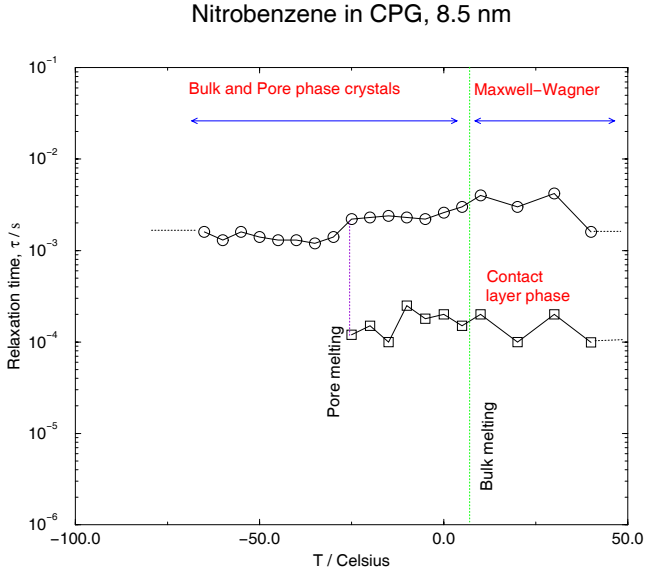

Figure 7.6: (a) κ' vs. T for nitrobenzene in CPG with average pore size of 8.5 nm. (b) τ vs. T for nitrobenzene in CPG with average pore size of 8.5 nm.

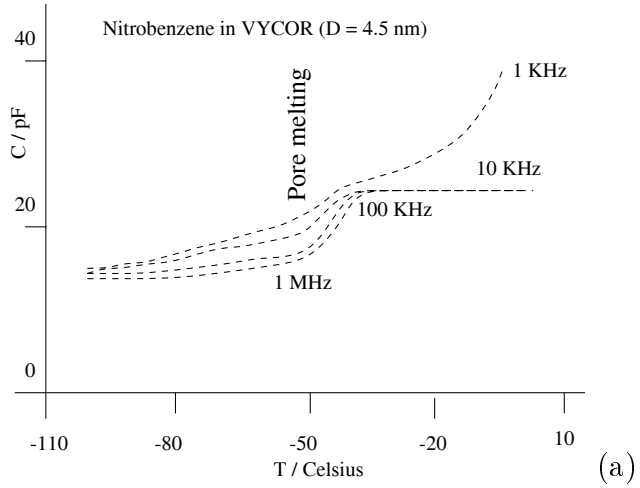

(b)

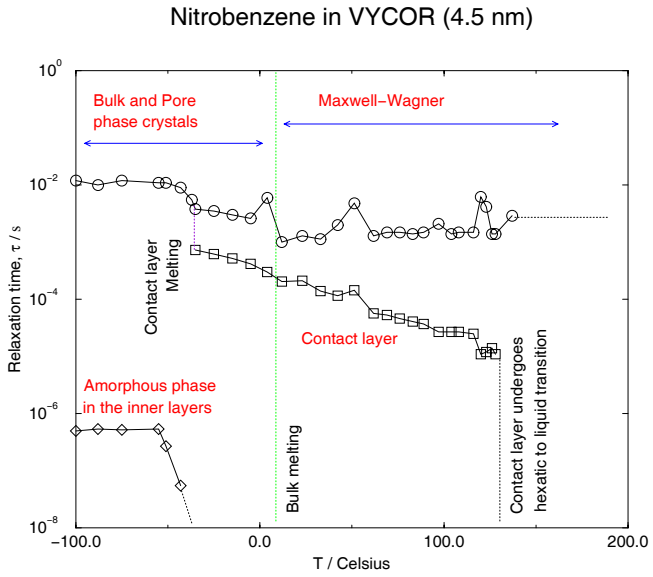

Figure 7.7: (a) κ' vs. T for nitrobenzene in Vycor with average pore size of 4.5 nm. (b) τ vs. T for nitrobenzene in Vycor with average pore size of 4.5 nm.

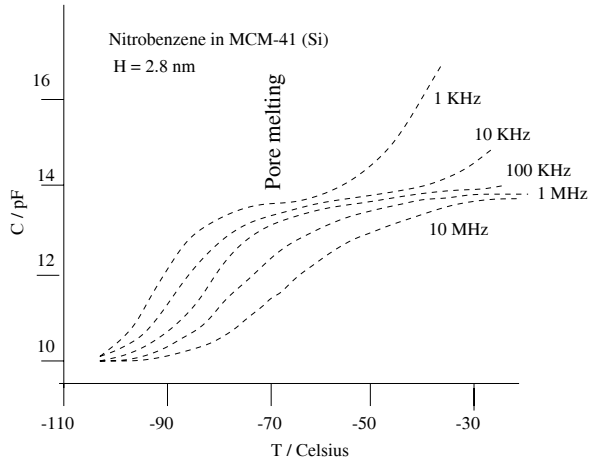

(a)

(b)

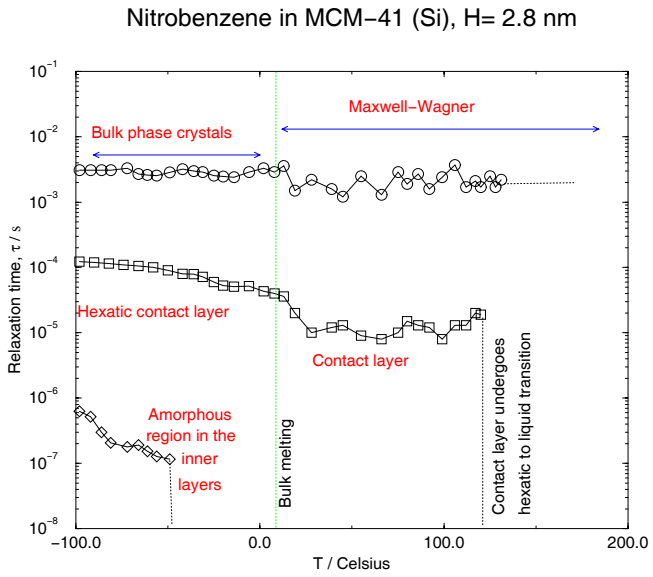

Figure 7.8: (a) κ' vs. T for nitrobenzene MCM-41 with average pore size of 2.8 nm. (b) τ vs. T for nitrobenzene in MCM-41 with average pore size of 2.8 nm.

Table 7.1: Freezing Temperatures: experimental measurement

H/nm	H/σ_{ff}	$T/$ ^{o}C	ordered phase
Bulk	-	5.8	crystal
25 (CPG)	50	2.0	crystal
8.5 (CPG)	17	-25	crystal
4.5 (Vycor)	9	-40	crystal + glass
2.8 (MCM-41, Si)	5.6	-50	hexatic + glass
2.8 (MCM-41, Al)	5.6	-65	hexatic + glass
2.4 (MCM-41, Si)	4.8	-65	hexatic + glass

fluid does not undergo a freezing transition, however a glass transition is observed.

7.2.5 The Hexatic Transition

The proposition that the quasi-two dimensional contact layer exists as a hexatic phase implies that at higher temperatures, the "hexatic" contact layer can undergo a transition to a orientationaly disordered, liquid-like contact layer. In figures 7.7(b) and 7.8(b), the disappearance of the microsecond branch of the relaxation time at high temperatures (100 ^{o}C), strongly suggests such a transition from a hexatic contact layer phase with a relaxation time $\tau = 10 \times 10^{-6}$ s to a liquid-like contact layer with nanosecond relaxation time. The transition from hexatic to liquid phase is a Kosterlitz-Thouless (KT) type transition [73, 128], and involves a large entropy change. In two-dimensions, the specific heat shows a non-universal peak at the KT transition. We performed DSC measurements for the case of nitrobenzene adsorbed in Vycor and MCM-41 (figures 7.9(a) and 7.9(b)). The DSC scan in figure 7.9(a0

shows a large peak at 5.6 ^{o}C corresponding to the melting of bulk nitrobenzene. In addition, there is a small peak at lower temperature (-35 ^{o}C) corresponding to melting of nitrobenzene confined inside the pores of Vycor. A magnified view of the high temperature region (70–100 ^{o}C) shows an additional peak which is consistent with the KT behavior (i.e., hexatic to liquid transition). This peak occurs at a temperature that is well below the capillary condensation transition; capillary condensation occurs above 250 ^{o}C for nitrobenzene in Vycor at 1 atm. pressure. Nitrobenzene in MCM-41 (figure 7.9(b)) shows a similar evidence of the hexatic to liquid transition about 100 ^{o}C.

Thus, for nitrobenzene in Vycor and MCM-41 materials, there is strong evidence that the contact layer phase exists as a hexatic phase until a temperature of 100 ^{o}C, above which it transforms into a liquid phase. This transition could either be a transition between an orientationaly ordered phase of dipoles (see cartoon in figure 7.10(a)), to a phase with random orientation of dipoles, or a transition between a phase in which the centers of the molecules (or the nearest neighbor bonds) are orientationaly ordered (see cartoon in figure 7.10(b)) to a disordered liquid like phase. Figure 7.10(a) represents a hexatic phase of dipole orientations (the dipole orientations for a vortex pattern) and figure 7.10 representations a hexatic phase of nearest neighbor bonds (bound pairs of five and seven coordinations are found as depicted by the dashed bonds) and a hexatic to liquid transition for both cases is expected to show a peak in the heat capacity. Conclusive evidence on the nature of the transition can only be obtained by careful study of the specific heat and x-ray diffraction coupled with molecular simulations.

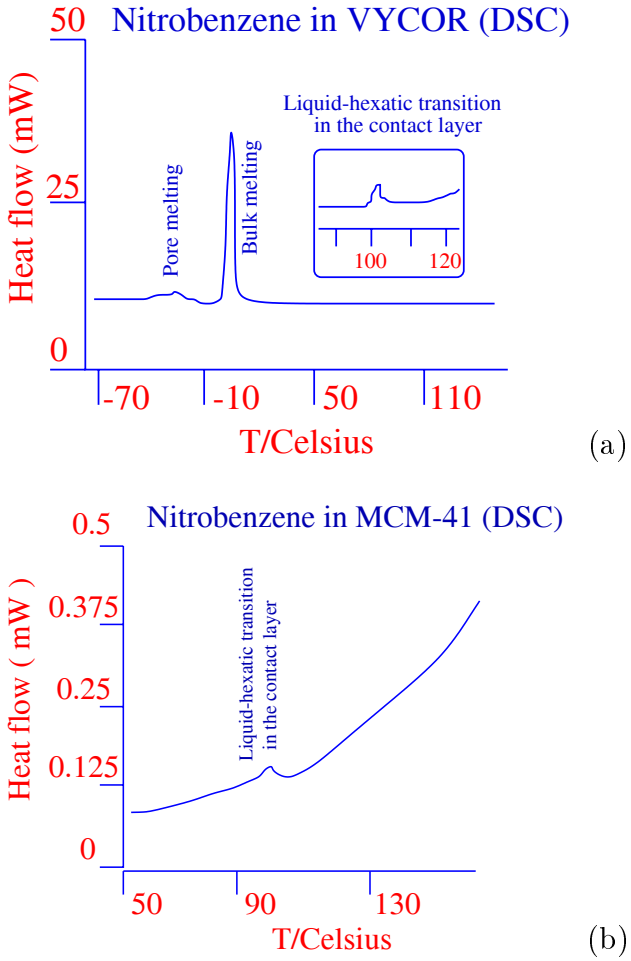

Figure 7.9: (a) DSC scan for nitrobenzene confined in Vycor glass. The inset is magnified 100 times compared to the original scan. (b) DSC scan for nitrobenzene confined in MCM-41.

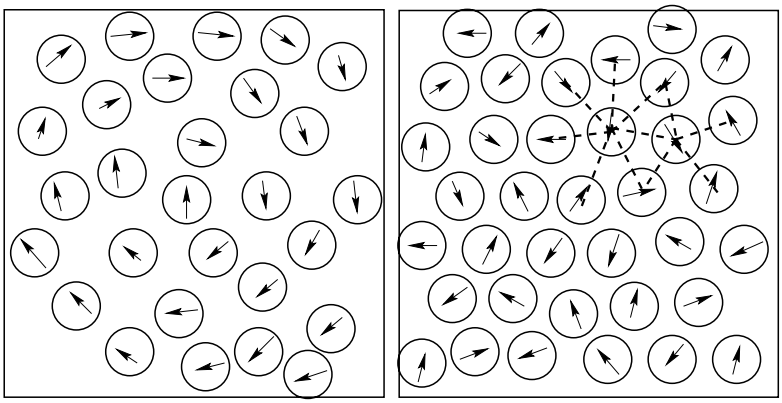

Figure 7.10: Cartoon showing the possible hexatic phases in the "unwrapped", quasi two dimensional contact layer. (a) Hexatic phase involving dipole orientations; the configuration corresponds to a vortex with its core at the center of the box. (b) Hexatic phase involving the orientation of nearest-neighbor bonds; the nearest neighbor bonds are orientationaly ordered, there is a coordination of six nearest neighbors for every molecule, with an ocassional five-seven bound pair indicated by the dashed bonds.

7.3 Simulation

The molecular simulations were performed for a spherical LJ fluid (with parameters chosen to mimic CCl_4) freezing in smooth silica cylinders of different pore diameters. Qualitative comparison is made with the DS and DSC experiments. Such a simplified model is expected to capture the high temperature hexatic to liquid transition and to elucidate the effect of varying pore diameter on the structure of the confined fluid and crystalline phases. Four different pore diameters ($H = 9\sigma_{ff}, 12\sigma_{ff}, 15\sigma_{ff}, \&20\sigma_{ff}$) were chosen to model the pores in MCM-41, Vycor, CPG (7.5 nm) and CPG (10 nm) respectively. The confined fluid structure was monitored by calculating the local density profile and pair correlation functions and by viewing snapshots of molecular configurations. The freezing temperature was calculated by using the Landau free energy methodology as outlined in section 7.1.3. We also calculated the two-dimensional, in-plane pair correlation function (2-d $g(r)$) and the two-point orientational correlation functions in the unwrapped contact layer to look for the possibility of a hexatic to liquid transition in the contact layer at high temperatures.

In order to calculate the two-point orientational correlation function, we invoked the hexatic order parameter [69] defined as

$$\Psi_6 \;=\; \frac{1}{N_b}\sum_{k=1}^{N_b} \exp(i6\theta_k) \;=\; \langle \exp(i6\theta_k) \rangle \tag{7.1}$$

Ψ_6 measures the hexagonal bond order in the unwrapped contact layer. Each nearest neighbor bond (as defined in section 7.1.3) has a particular orientation in the plane of the unwrapped contact layer, with respect to a reference axis, and is described by the polar coordinate θ. The index k runs over the total number of nearest neighbor bonds N_b in the contact layer. We expect $\Psi_6 = 0$ when the contact layer has the

structure of a two-dimensional liquid, $\Psi_6 = 1$ in the crystalline phase and $0 < \Psi_6 < 1$ in the orientationaly ordered hexatic phase. The two-point orientational correlation function in the unwrapped contact layer is defined as $< \Psi_6^*(0)\Psi_6(r) >$. The decay of the $< \Psi_6^*(0)\Psi_6(r) >$ function with increasing r is different in liquid, hexatic and crystalline phases; the correlation function shows an exponential decay in the isotropic liquid phase, algebraic decay ($1/r$ behavior) in the hexatic phase, and is a constant in the crystalline phase. The liquid to hexatic transition temperature in the contact layer is estimated by monitoring the change in behavior of the two-point orientational correlation function with temperature.

7.3.1 Freezing of the Confined Phase

The Landau free energy function for LJ CCl_4 in a cylindrical silica pore of diameter $20\sigma_{ff}$ at $k_BT/\epsilon_{ff} = 0.4$ is shown in figure 7.11. The order parameter Φ is equal to Q_6 defined in equation 2.10. The minimum centered around $\Phi = 0$ corresponds to liquid phase and that centered around $\Phi = 0.35$ corresponds to an fcc crystalline phase. The grand free energy of the liquid and crystalline phases at $T^* = 0.38$ using equation 2.7 are equal; therefore the freezing temperature for this system is $T^* = 0.38$. A snapshot from the simulation of the fcc crystalline phase at $T^* = 0.38$ is shown in figure 7.12(a). It is evident from the simulations that for a pore diameter of $20\sigma_{ff}$ the fluid freezes into a fcc crystalline phase inside the cylinder. For pore diameters smaller than $20\sigma_{ff}$, the minimum in the landau free energy function corresponding to the fcc crystalline phase did not exist. The pair correlation functions and the snapshots from the molecular simulations strongly indicate a glass transition instead. A snapshot from the simulations for LJ CCl_4 in a cylindrical pore of diameter $H = 12\sigma_{ff}$ is shown in figure 7.12(b); the temperature corresponds to

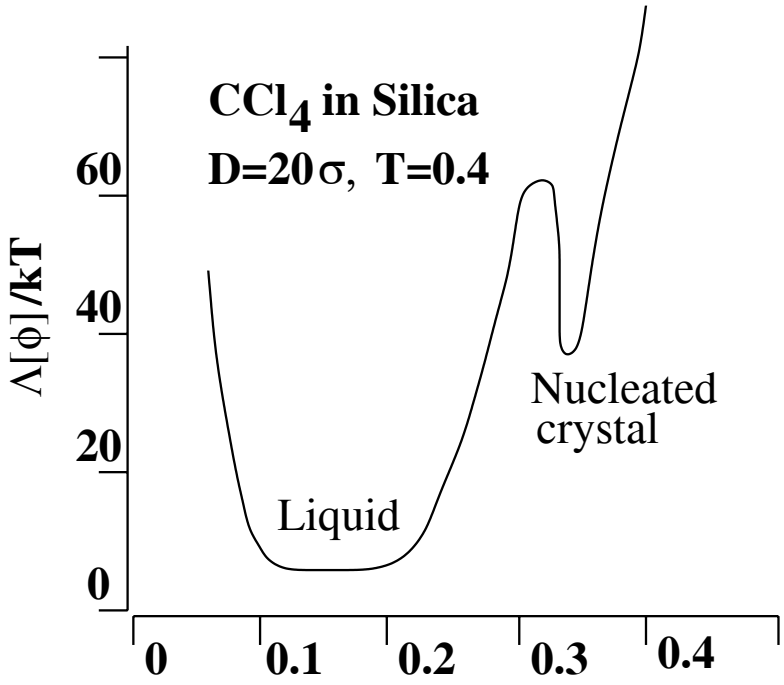

Figure 7.11: The Landau free energy function as a function of the order parameter $\Phi = Q_6$ at $T^* = 0.4$ showing two minima; The minimum corresponding to the liquid phase is close to $\Phi = 0$ and the fcc crystalline phase is represented by the minimum centered around $\Phi = 0.35$.

$T^* = 0.34$ and the snapshot is consistent with the amorphous nature of the confined phase.

7.3.2 Hexatic Transition in the Contact Layer

The two-dimensional, in-plane pair correlation functions (positional pair correlation function, $g(r)$ and orientational correlation function $< \Psi_6^*(0)\Psi_6(r) >$ where $\Psi_6(r)$ is given by equation 7.1) were monitored as a function temperature in the unwrapped contact layer shell. The correlation functions for the contact layer shell confined in a cylinder of diameter $15\sigma_{ff}$ are shown in figure 7.13 at three different temperatures. At a high temperature of $T^* = 0.64$, the pair correlation is isotropic and the ori-

(a)

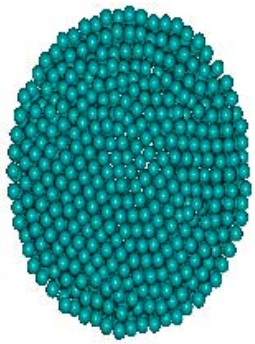

(b)

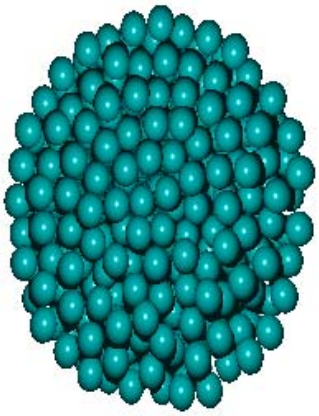

Figure 7.12: Snapshot from molecular simulation showing the confined fcc crystalline phase of LJ CCl_4 in a silica cylinder. (a) Confined crystalline (fcc) phase in a pore of diameter $20\sigma_{ff}$ at temperature, $T^* = 0.38$. (b) The confined phase consists of a hexatic contact layer and an amorphous inner region in a pore of diameter $12\sigma_{ff}$ at temperature, $T^* = 0.34$.

entational correlation function decays to zero exponentially, suggesting a liquid like contact layer. As the temperature is lowered to $T^* = 0.52$, the pair correlation function is isotropic but displays long range correlations. The orientational correlation function decays algebraically ($1/r$ behavior), which is a clear signature of a hexatic (orientationaly ordered) contact layer phase. On further reducing the temperature to $T^* = 0.48$, the contact layers freezes to a hexagonal crystal. This is manifested as split peaks in the pair correlation function and no decay in the orientational correlation function. On further lowering the temperature, there is partial crystallization in the inner regions of the confined fluid phase with the rest forming an amorphous phase, as discussed in section 7.3.1. It is clear from the simulations that the hexatic transition in the contact layer is a transition involving nearest neighbor bonds as spherical LJ molecules are orientationaly isotropic.

The behavior of the contact layer phase in a smaller cylinder ($H = 12\sigma_{ff}$, figure 7.14) is significantly different. At high temperature, $T^* = 0.64$, the contact layer correlation functions are typical of the liquid phase, and at $T^* = 0.48$, there is a clear signature of a hexatic phase behavior (compare with figure 7.13 at $T^* = 0.52$). There is a significant difference in the behavior of the contact layer phase at low temperature. The correlation functions at $T^* = 0.38$ indicate that even at such a low temperature, the contact layer does not undergo a freezing transition. This is consistent with the fact that, the Landau free energy functions as well as the pair correlation functions and the snapshots, did not support any evidence of a crystalline or a partially crystalline confined phase for cylinders with diameters smaller than $12\sigma_{ff}$, (see section 7.3.1). The simulation results of the freezing behavior of LJ CCl_4 in silica-based cylinders are summarized in table 7.2.

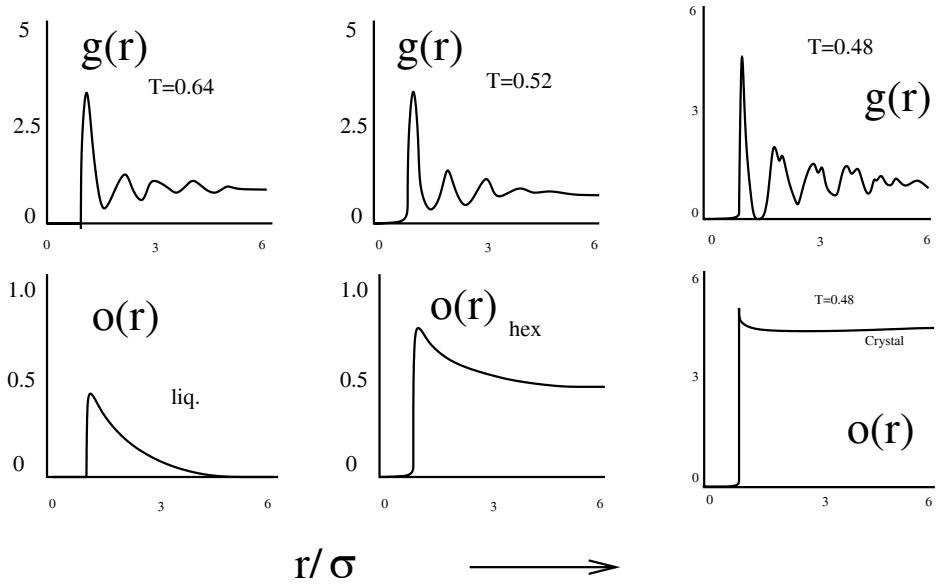

Figure 7.13: Two-dimensional, in-plane positional correlation functions ($g(r)$) and orientational correlation functions ($o(r) =< \Psi_6^*(0)\Psi_6(r) >$) for three different temperatures in the unwrapped contact layer shell. The plots are for LJ CCl_4 in a silica cylinder of diameter $15\sigma_{ff}$, showing the liquid, hexatic and crystalline phases in the contact layer at $T^* = 0.64$, $T^* = 0.52$ and $T^* = 0.48$ respectively.

Table 7.2: Freezing Temperatures: molecular simulation

H/σ_{ff}	k_BT/ϵ_{ff}	ordered phase
≥ 20 (large pores)	†	crystal
20	0.4	crystal
15	0.38	crystal + glass
12	0.36	hexatic + glass
9	0.35	hexatic + glass

† Gibbs-Thomson equation is valid

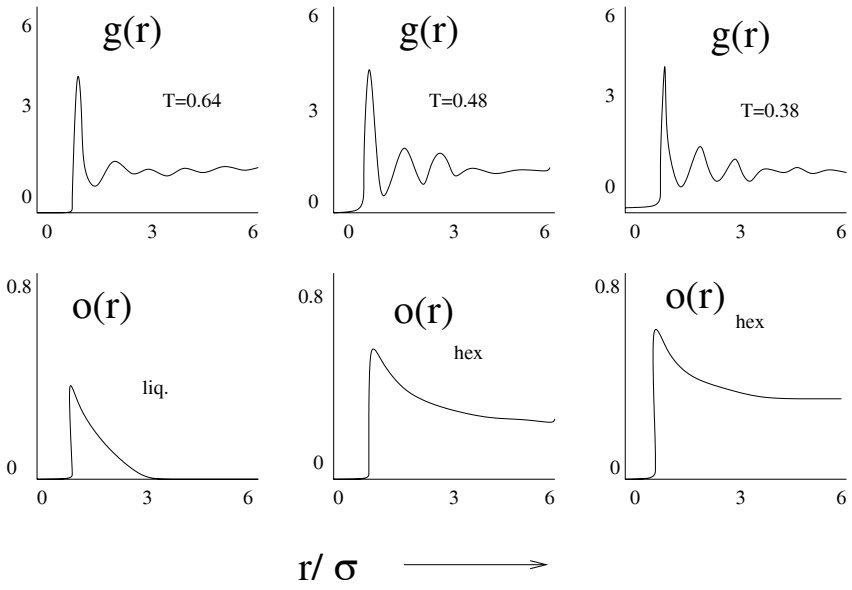

Figure 7.14: Two-dimensional, in-plane positional correlation functions ($g(r)$) and orientational correlation functions ($o(r) =< \Psi_6^*(0)\Psi_6(r) >$) for three different temperatures in the unwrapped contact layer shell. The plots are for LJ CCl_4 in a silica cylinder of diameter $12\sigma_{ff}$, showing the liquid and hexatic phases in the contact layer at $T^* = 0.64$, $T^* = 0.48$ and $T^* = 0.38$.

7.4 Conclusion

Recently, the freezing behavior in slit shaped pores have been understood in considerable detail [107]. In the case of freezing in cylindrical geometry, the qualitative behavior is similar to that of slit-shaped pores. However, there are two important differences. Firstly, the freezing temperatures in a cylindrical pore are in general lower than a slit pore of the same porous material and pore size [105]. Secondly, a freezing transition is observed (resulting in a homogeneous crystalline confined phase) in the case of slit pores for all pore sizes up to the smallest pore size, that accommodates only one molecular layer of adsorbed molecules [83, 81]. In the case of cylinders, however, our experiments as well as simulations clearly show that, a homogeneous crystalline confined phase results only for cylindrical pores with average diameters larger than $20\sigma_{ff}$. For cylindrical pores with diameters in the range $12 < H/\sigma_{ff} < 20$, the confined phase at low temperature is an inhomogeneous phase with partially crystalline domains interspersed with amorphous regions. For cylindrical pores with $H \leq 12\sigma_{ff}$, the confined phase at low temperature consists of a hexatic contact layer and an amorphous inner region.

Our experiments and simulations provide a very clear evidence of a contact layer hexatic phase that undergoes a hexatic to liquid transition at higher temperatures (the presence of a hexatic contact layer phase is established in the case of slit-shaped pores [83, 129]). It is also clear from the simulations that the hexatic transition is a transition involving nearest neighbor bonds. In addition, for cylinders with diameters $H \geq 15\sigma_{ff}$, the contact layer hexatic phase undergo a freezing transition at lower temperature. For the case of the large cylinders, it is clear from our simulations that the freezing transition of the contact layer is different from the

freezing transition in the inner layers. Thus, for a narrow range of temperatures $T_{f,inner\,region} < T < T_{f,contact\,layer}$, the confined phase consists of crystalline contact layers with liquid-like inner region (the presence of such a frozen contact layer phase is very well established in strongly attractive slit-pores [107]). Although, it is not apparent from our experimental measurements that the contact layers freeze at a temperature different from the inner layers, some earlier experimental studies have reported "pre-freezing" of the contact layer phase that results in a metastable phase characterized by crystalline contact layer and liquid-like inner region [106, 127]. Theoretical justification of the metastable contact layer phase was provided by Sliwinska-Bartkowiak et al., using Landau free energy surfaces [106].

Chapter 8

Conclusions and future direction

Amidst the controversy over the nature of the shift nature of the freezing point in the experiments [44, 2], the study by Miyahara and Gubbins [47] provided the first clear picture on the nature of the shift in the freezing temperature on confinement using molecular simulation of the confined phases. Attempts to verify the results of Miyahara and Gubbins, using free energy calculations (based on thermodynamic integration methods [130]) were faced with serious constraints [51]. Therefore, we invoked the Landau free energy method (chapter 2) to circumvent the obstacles in calculating the free energy change across a phase boundary, for confined systems. This methodology was successfully used to understand the freezing behavior in slit-shaped pores. The free energy results clearly established a first order phase transition despite the absence of a sharp change in the density across the solid-fluid phase boundary. True long range order exists in the confined crystalline phase, and was verified by calculating the positional and orientational pair correlation functions over large length scales (see figure 6.1 in chapter 6). A spectrum of freezing behavior was observed as the relative strength of the fluid-wall interaction to the fluid-fluid interaction was varied, i.e., by adjusting the value of the parameter α (see figure 5.4

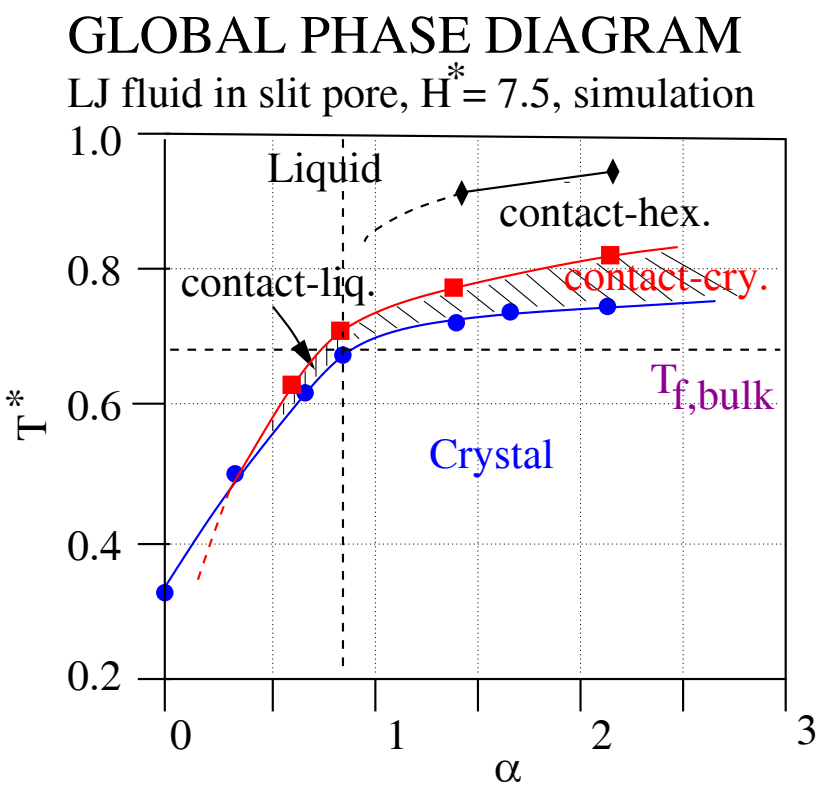

Figure 8.1: Global phase diagram for a Lennard-Jones fluid in a slit shaped pore of width $H = 7.5\sigma_{ff}$. Five different phases are observed: liquid, contact-hexatic, contact-crystal, contact-liquid and crystalline. The different phases are characterized by the positional and orientational correlation functions as depicted in figure 8.2.

in chapter 5). The existence of the contact layer phase and the hexatic phase was established established in the simulations. A summary of the phase behavior of a Lennard-Jones fluid in slit shaped pores is given in figure 8.1.

The reduced freezing temperature of bulk Lennard-Jones fluid (under ambient pressures) is 0.682 as depicted by the horizontal dashed line in figure 8.1 The freezing temperature shifts upwards on confinement for values of α greater than 0.9 (strongly attractive pores), and shifts downwards for values of α less than 0.8. The contact layers (layers adjacent to the pore walls) freeze at a different temperature compared to the inner layers. For strongly attractive pores, the freezing of the contact layers

occur at a temperature higher than the inner layers, while for weakly attractive walls the freezing of the contact layers occur at a temperature lower than the inner layers; this leads to the formation of two new phases that we term as contact-crystalline and contact-liquid phases respectively. The hatched regions in figure 8.2 are the regions where the two contact layer phases are thermodynamically stable. For strongly attractive pores, the contact layers undergo a liquid-hexatic phase transition, that leads to the formation of another new phase that we term "contact-hexatic". The stable regions of the contact-hexatic phase are between the lines marked by the diamonds and the squares in figure 8.2. The crystal phase boundary is marked by the circles, below which the crystalline phase is stable. The different phases are distinguished on the basis of the behavior of the two-dimensional, in-plane pair correlation function ($g(r)$) and orientational correlation function, $G_{6,j}(\rho) =< \Psi^*_{6,j}(0)\Psi_{6,j}(\rho) >$ (see chapter 6) in the confined molecular layers, a summary is provided in figure 8.2: In the figure, the pair correlation functions in the liquid phase are isotropic and those in the crystalline phase correspond to a 2-d hexagonal crystal, in each of the confined layers. In addition, the behavior of the orientational correlation functions in the liquid phase show an exponential decay. The contact-crystalline phase consists of a crystalline contact layer and liquid like inner layers, while the contact-liquid phase consists of a liquid-like contact layer and crystalline inner layers. The 2-d $g(r)$ in the contact-hexatic phase is liquid like in all the confined layers, however the orientaional correlation function in the contact layer shows an algebraic $(1/r)$ decay while those in the inner layers show an exponential decay.

The global phase diagram for a different pore width ($H = 3\sigma_{ff}$) is shown in figure 8.3. For this choice of pore width, there are no "contact" phases as only

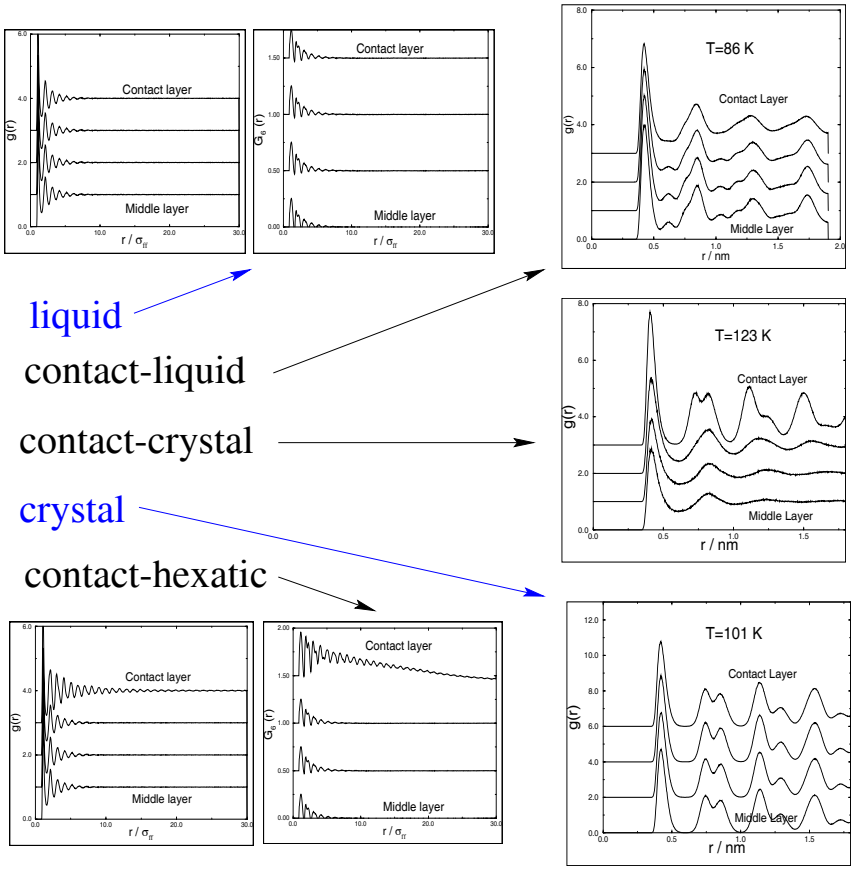

Figure 8.2: The 2-d, in-plane positional and orientational pair correlation functions in the confined molecular layers of a LJ molecule in a slit shaped pore of width $H = 7.5\sigma_{ff}$

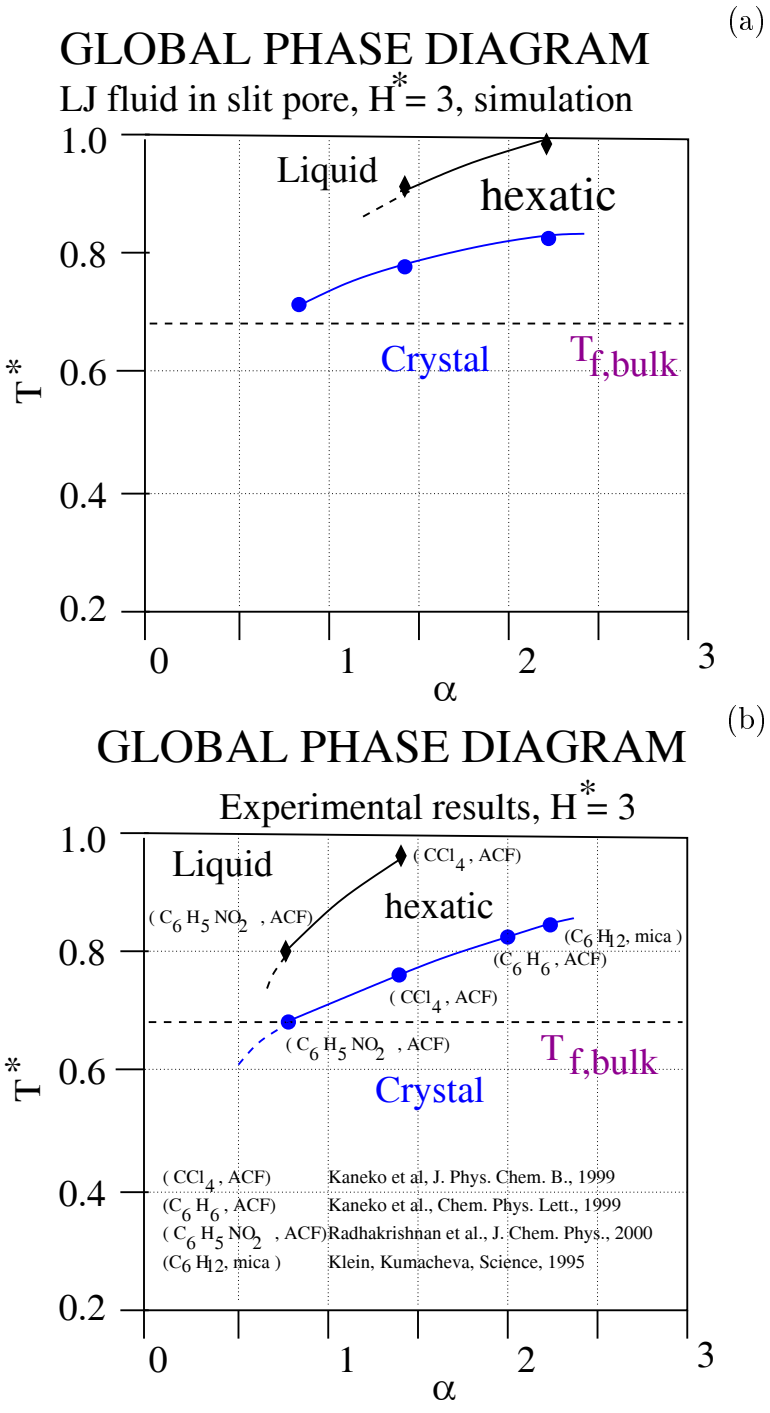

Figure 8.3: Global phase diagram of a fluid in slit pore of width $H = 3\sigma_{ff}$: (a) from simulation, (b) from experiment.

two confined molecular layers are present, both of which are contact layers. The phase boundaries from the simulations and experiments for this system are in excellent agreement (to within 10 %) despite the simplicity of the model used in the simulations.

The effect of pore width on the freezing temperature was understood in the slit shaped activated carbon fibers and cylindrical shaped pores of porous glasses and MCM-41 using simulation and experiment (chapters 3,4,7). The macroscopic equations like the Gibbs-Thomson equation (equation 1.1) were found to be valid in the large pore limit ($H > 6\sigma_{ff}$ for slits-shaped pores and $H > 20\sigma_{ff}$ for cylindrical pores). For smaller pores, the deviation from the classical behavior are primarily caused by the spatial inhomogeneity in the fluid structure (chapters 3,7).

There are two important differences in the freezing behavior of fluids confined in slit pores when compared to that in cylindrical pores. Firstly, the freezing temperatures in a cylindrical pore are in general lower than a slit pore of the same porous material and pore size [105]. Secondly, a freezing transition is observed (resulting in a homogeneous crystalline confined phase) in the case of slit pores for all pore sizes up to the smallest pore size, that accommodates only one molecular layer of adsorbed molecules, (chapters 3,6). In the case of cylinders, however, our experiments as well as simulations (chapter 7) clearly show that, a homogeneous crystalline confined phase results only for cylindrical pores with average diameters larger than $20\sigma_{ff}$. For cylindrical pores with diameters in the range $12 < H/\sigma_{ff} < 20$, the confined phase at low temperature is an inhomogeneous phase with partially crystalline domains interspersed with amorphous regions. For cylindrical pores with $H \leq 12\sigma_{ff}$, the confined phase at low temperature consists of a hexatic contact layer and an

amorphous inner region.

Numerous extensions to these studies can prove to be effective. Fluid behavior in complex pore geometries from a free energy perspective can provide more accurate predictions so that a quantitative comparison with experimental measurements are feasible. Recently more realistic models of porous glasses and activated carbon fibers have been developed [121, 131], that include dispersions in pore size, networking and connectivity found in the real porous materials. Some of the possibilities were described in Chapters 3 and 4. In addition, the use of more realistic interaction potentials would be a necessity.

The effect of pressure on the freezing behavior in confined systems have on been dealt with in our study. There have been some experimental studies by Duffy et al [32, 132] that deal with a P-T diagram of CO_2 confined in Vycor glass. More recently, Morishige and Kawano [127] have also studied the P-T diagram of methanol confined in MCM-41 using neutron scattering experiments. Miyahara et al. have constructed the P-T diagram of methane in a graphite slit prore using molecular dynamics [133]. An interesting attribute of their study is that the slope of the solid-liquid co-existence line near the triple point of the P-T diagram of the confined system is not a constant, which is very unlike the scenario in the bulk. The effect of confinement on the triple point in confined systems still remains an open question. On the experimental front, more sophisticated measurements involving x-ray diffraction, neutron scattering and EXAFS can lead to a better understanding of the structure of the confined phases.

Finally, I wish to bring to consideration a close but different class of phase transitions which are glass transitions. In general, one must exercise care in interpreting freezing inside pores. Experiments such as differential scanning calorimetry do not give any information on the structure of the confined phase. It is also difficult to use diffraction methods to characterize the structure of the confined phase, because of the presence of the additional signal due to the adsorbent molecules. Spectroscopic methods such as NMR and dielectric relaxation spectroscopy are useful under these circumstances, as they yield information about the translational and orientational relaxation time of the molecules in the confined phase. For example, in the study of freezing of O_2 in sol-gel glasses [25], the orientational relaxation time τ of molecules was measured as a function of T and a sharp drop in τ (about four orders of magnitude) was observed at the transition. A similar measurement for a glass transition would show a continuous change from liquid phase to glass phase relaxation times.

In computer simulation studies of freezing in confined geometries, it is possible to directly measure the pair correlation function to monitor the freezing process. However, for finite system size even a glassy phase can display extended positional correlations [134]. An additional measure of the self-diffusion coefficient often provides a distinction between a freezing transition and a glass transition. Free energy calculations are very useful, as the nature of the phase transition can be inferred directly. The order parameter provides a direct measure of the difference in bond orientational order between the ordered and disordered phase. Thus, for the case of a glass transition, the minimum in the Landau free energy curve at the value of the order parameter corresponding to the crystalline phase would be absent. In addition the calculations of the positional and orientational correlation functions over a large length scale (e.g., see chapter 6) often provides the distinction between ordered

crystalline and glassy phases in a computer simulation. The long range behavior of the orientational correlation functions of the crystal phase are very different from that of the glass phase.

The glass transition in a porous medium is an interesting topic in its own right. There have been a number of studies that have investigated the effect of confinement on glass-forming organic liquids [97, 100, 135, 98]. It is well established that the glass transition temperature T_g of a liquid inside a porous glass is shifted by ΔT_g, the sign and extent of which is material-specific, just as for the case of freezing. Dielectric relaxation studies have indicated a slower relaxation process in the confined liquid as compared to the bulk, and the appearance of an additional relaxation component due to the contact layer, consistent with the studies on freezing. However, unlike freezing, there seems to be no general basis to explain the nature of the shift in ΔT_g.

Although the effectiveness of the Landau free energy approach to study phase behavior in confined systems was described in the previous chapters, I wish to remark that the approach is generic and can be used to study a large class of problems. For example, the key to understanding many biological phenomena hinges on a clear understanding of the crystalline phase of water. Water has a very complex phase diagram in the solid region, in that it has eleven known crystalline phases and also some amorphous phases. The time scales needed to nucleate the ice phase is not currently accessible by computer simulations. There has been some success in freezing the water by applying strong homogeneous electric field, a process known as electro-freezing [136]. One can use the order parameter formulation to calculate the free energy change across the phase transition. The Landau free energy formulation allows for calculation of the free energies in the zero electric field limit through

Legendre transformation and a clever choice of the field variables. The Landau free energy method is not limited to electro-freezing that only accesses the highly polarized cubic ice form. The more common hexagonal ice form can be studied by choosing a different order parameter and field variables.

On a larger perspective, a different class of problems involving chemical reactions can be tackled by the Landau free energy formalism, by drawing a parallel between the order parameter and the reaction coordinate. The definite advantage of this approach in combination with path integral simulations [137] or Car-Parrinello molecular dynamics [138] over transition state theories is that, the entropic effects are taken into account accurately; for instance, the effect of pressure on a chemical reaction can be estimated precisely. Such methods can then be applied to problems involving homogeneous and heterogeneous catalysis, that are widespread in the chemical industry. The Landau free energy formalism also provides a natural framework in constructing the free energy surfaces of the molecular conformations of proteins. A better understanding of the folding mechanisms of protein molecules key to finding a cure for many genetic disorders.

Bibliography

[1] K. Kaneko. In A. Dobrowski, editor, *Adsorption and its Application to Industry and Environmental Protection: Surface Science and Catalysis 120B*, volume II. Elsevier, Amsterdam, 1998.

[2] M. Sliwinska-Bartkowiak, J. Gras, R. Sikorski, R. Radhakrishnan, L. D. Gelb, and K. E. Gubbins. Phase transition in pores: experimental and simulation studies of melting and freezing. *Langmuir*, 15(18):6060, 1999.

[3] W. M. Meier and D. H. Olson. *Atlas of Zeolite Structure Types*. Butterworth-Henemann, London, 1992.

[4] J. S. Beck, J. C. Vartuli, W. J. Roth, M. E. Lenonowicz, C .T. Kresge, K. D. Schmitt, C. T. W. Chu, D. H. Olson, E. W. Sheppard, S. B. McCullen, J. B. Higgins, and J. L Schlenker. *J. Amer. Chem. Soc.*, 114:10834, 1992.

[5] T. W. Ebbesen. *Carbon Nanotubes*. CRC Press, Boca Raton, New York, ed., 1997.

[6] G. S. Attard, J. C. Glyde, and C. G. Göltner. *Nature*, 378:366, 1995.

[7] C. G. Göltner and M. Antonietti. *Adv. Mater.*, 9:431, 1997.

[8] M. C. Weissenberger, C. G. Göltner, and M. Antonietti. *Ber. Bunsenges. Phys. Chem.*, 101:1679, 1997.

[9] W. Haller. Application of controlled pore glass in solid phase biochemistry. In W. H. Scouten, editor, *Solid Phase Biochemistry*, chapter 11, pages 535–597. John Wiley and Sons, New York, 1983.

[10] R. K. Iler. *The Chemistry of Silica*. John Wiley, New York, 1979.

[11] R. W. Pekala, C. T. Alviso, F. M. Kong, and S. S Hulsey. *J. Non-Crystalline Solids*, 145:90–98, 1992.

[12] R. W. Pekala and C. T. Alviso. *Mat. Res. Soc. Symp. Proc.*, 270:3–14, 1992.

[13] Y. Hanzawa, K. Kaneko, R. W. Pekala, and M. S. Dresselhaus. *Langmuir*, 12:6167–6169, 1996.

[14] Y. Hanzawa, T. Yoshizawa, and K. Kaneko. *private communication*, 1998.

[15] J. S. Mattson and H. B. Mark. *Activated Carbon, Surface Chemistry and Adsorption from Solution.* Marcel Dekker, New York, 1971.

[16] IUPAC. *International Committee for Characterization and Terminology of Carbon*, 20:445; ibid. 21, 517; ibid. 23, 601, 1985.

[17] R. C. Bansal, J. B. Donnet, , and H. F. Stoeckli. *Active Carbon.* Marcel Dekker, New York, 1988.

[18] B. McEnaney and T. M. Mays. *Introduction to Carbon Science.* Butterworths, London, 1989.

[19] J. W. Patrick. *Porosity in Carbons: Characterization and Applications.* Halsted Press, New York, 1995.

[20] M Biggs and P. Agarwal. *Phys. Rev. A*, 46:3312, 1992.

[21] M Biggs and P. Agarwal. *Phys. Rev. E*, 49:531–537, 1995.

[22] R. Evans. Fluids adsorbed in narrow pores: phase equilibria and structure. *J. Phys.: Condens. Matter*, 2(46):8989–9007, 1990.

[23] K. E. Gubbins, M. Sliwinska-Bartkowiak, and S-H. Suh. *Molecular Simulation*, 17:333–367, 1996.

[24] C. Eyraud, J.F. Quinson, and M. Brun. Characterization of porous solids. page 307, Amsterdam, 1988. Elsevier.

[25] J. Warnock, D. D. Awschalom, and M. W. Shafer. Geometrical supercooling of liquids. *Phys. Rev. Letts.*, 57(14):1753, 1986.

[26] J. L. Tell, H. J. Maris, and G. M. Seidel. *Phys. Rev. B*, 28:5122, 1983.

[27] R. H. Torii, H. J. Maris, and G. M. Seidel. *Phys. Rev.B*, 41:7167, 1990.

[28] P. E. Sokol, W. J. Ma, K. E. Herwig, W. M. Soon, Y. Wang, J. Koplik, and J. R. Banavar. *Appl. Phys. Lett.*, 61:777, 1992.

[29] J. H. Strange, M. Rahman, and E. G. Smith. *Phys. Rev. Letts.*, 71:3589, 1993.

[30] E. Molz, A. P. Y. Wong, M. H. W. Chan, and J. R. Beamish. Freezing and melting of fluids in porous glasses. *Phys. Rev. B*, 48(9):5741, 1993.

[31] K. M. Unruh, T. E. Huber, and C. A. Huber. Melting and freezing behavior of indium metal in porous glasses. *Phys. Rev. B*, 48(12):9021, 1993.

[32] J. A. Duffy, N. J. Wilkinson, H. M. Fretwell, M. A. Alam, and R. Evans. Phase transitions of CO_2 confined in nanometer pores as revealed by positronium annihilation. *J. Phys. Cond. Mat.*, 7:L713, 1995.

[33] E. W. Hansen, M. Stöker, and R. Schmidt. *J. Phys. Chem.*, 100:2195, 1996.

[34] K. J. Elder, P. A. Reynolds, F. Trouw, and J. W. White. *J. Chem. Soc. Chem. Comm.*, page 155, 1996.

[35] J. Krim, J. P. Coulomb, and J. Bouzidi. *Phys. Rev. Letts.*, 58:583–586, 1987.

[36] K. Morishige, H. Fujii, M. Uga, and D. Kinukawa. Capillary critical point of argon, nitrogen, oxygen, ethylene, and carbon dioxide in mcm-41. *Langmuir*, 13:3494–3498, 1997.

[37] K. Morishige and K. Kawano. *J. Chem. Phys.*, 110:4867–4872, 1998.

[38] K. Overloop and L. Van Gerven. Freezing phenomena in adsorbed water as studied by nmr. *J. Magnetic Resonance A*, 101:179, 1993.

[39] H. F. Booth and J. H. Strange. Organic nanocrystals: an nmr study of cyclohexane in porous silica. *Mol. Phys.*, 93(2):263, 1998.

[40] R. Evans and U. Marini Bettolo Marconi. *J. Chem. Phys*, 86:7138–7148, 1987.

[41] J. M. Baker, J. C. Dore, and P. Behrens. *J. Phys. Chem. B*, 101:6226, 1997.

[42] K. Morishige and K. Kawano. *Japenese Journal*, submitted, 1999.

[43] A. J. Brown, C. G. V. Burgess, D. H. Everett, and S. Nuttall. In T. J. McEnaney, J. Mays, F. Rouquerol, Rodriguez-Reinoso, K. S. W. Sing, and K. K. Unger, editors, *Characterization of Porous Solids IV*, pages 1–8. Royal Society of Chemistry, Cambridge, 1997.

[44] J. Klein and E. Kumacheva. onfinement-induced phase transitions in simple liquids. *Science*, 269:816, 1995.

[45] H.W. Hu, G.A. Carson, and S. Granick. *Phys. Rev. Lett.*, 66, 1991.

[46] S. Granick. *Science*, 253, 1991.

[47] M. Miyahara and K. E. Gubbins. Freezing/melting phenomena for lennard-jones methane in slit pores: a monte carlo study. *J. Chem. Phys.*, 106(7):2865, 1997.

[48] M. Maddox and K. E. Gubbins. Gubbins, a molecular simulation study of freezing/melting phenomena for lennard-jones methane in cylindrical nanoscale pores. *J. Chem. Phys.*, 107:9659, 1997.

[49] M. A. Castro, S. M. Clarke, A. Inaba, and R. K. Thomas. Solid monolayers adsorbed at the solid-liquid interface by incoherent elastic neutron scattering. *J. Phys. Chem. B*, 101:8878, 1997.

[50] H.K. Christenson. *Colloid Surface A*, 123, 1997.

[51] H. Dominguez, M. P. Allen, and R. Evans. Monte carlo studies of the freezing and condensation transitions of confined fluids. *Mol. Phys.*, 96:209–229, 1998.

[52] D. Frenkel and A. J. C. Ladd. Ladd, a new monte carlo method to compute the free energy of arbitrary solids. application to the fcc and hcp phases of hard spheres. *J. Chem. Phys.*, 81(7):3188, 1984.

[53] W. A. Steele. The physical interactions of gases with crystalline solids. i. gas-solid energies and properties of isolated adsorbed atoms. *Surf. Sci.*, 36:317–352, 1973.

[54] W. A. Steele. *The interaction of gases with solid surfaces.* Pergamon press, Oxford, 1974.

[55] S. Jiang, C. L. Rhykerd, and K. E. Gubbins. *Mol. Phys.*, 79:373–391, 1993.

[56] G.B. Woods and J.S. Rowlinson. *Faraday Trans. 2*, 85, 1989.

[57] L. D. Landau and E. M. Lifshitz. *Statistical Physics.* Pergamon Press, London, 3 edition, 1980.

[58] P.M. Chaikin and T.C. Lubensky. *Principles of Condensed matter Physics.* Cambridge University Press, Cambridge, 1995.

[59] J. S. Van Duijneveldt and D. Frenkel. Computer simulation study of free energy barriers in crystal nucleation. *J. Chem. Phys.*, 96(6):4655, 1992.

[60] R. M. Lynden-Bell, J. S. van Duijneveldt, and D. Frenkel. Free energy changes on freezing and melting ductile metals. *Mol. Phys.*, 80(4):801–814, 1993.

[61] G.M. Torrie and J.P. Valleau. *Chem. Phys. Lett.*, 28, 1974.

[62] J.K. Johnson, J.A. Zollweg, and K.E. Gubbins. *Mol. Phys.*, 78(3):591, 1993.

[63] D. A. Kofke. Direct evaluation of phase coexistence by molecular simulation via integration along the saturation line. *J. Chem. Phys.*, 98(5):4149–4162, 1993.

[64] R. Agrawal and D.A. Kofke. *Mol. Phys.*, 85, 1995.

[65] P.J. Steinhardt, D.R. Nelson, and M. Ronchetti. *Phys. Rev. B*, 28, 1983.

[66] C. G. Gray and K. E. Gubbins. *Theory of Molecular Fluids*, volume Ch. 2 and App. C. Clarendon Press, Oxford, 1984.

[67] L.D. Landau and E.M. Lifshitz. *Quantum Mechanics*. Pergamon Press, New York, 1965.

[68] J. P. Hansen and L. Verlet. *Phys. Rev.*, 184:151, 1969.

[69] N.D. Mermin. *Phys. Rev.*, 176, 1968.

[70] D.R. Nelson and B.I. Halperin. *Phys. Rev. B*, 19, 1979.

[71] N. Goldenfeld. *Phase Transitions and the Renormalization group*. Addison-Wesley, New York, 1992.

[72] N.D. Mermin and H. Wagner. *Phys. Rev. Lett.*, 17, 1966.

[73] J.M. Kosterlitz and D.J. Thouless. *J. Phys. C,*, 5, 1972.

[74] K.J. Strandburg. *Rev. Mod. Phys.*, 60, 1988.

[75] J.D. Brock, R.J. Birgeneau, J.D. Lister, and A. Aharony. *Phys. Today*, July, 1989.

[76] R.J. Birgeneau and J.D. Lister. *J. de Physique Letters*, 39:L399, 1978.

[77] C.Y. Chao, C.F. Chou, J.T. Ho, S.W. Hui, A. Jin, and C.C. Huang. *Phys. Rev. Lett.*, 77(13):2750, 1996.

[78] J. Lee and J.M. Kosterlitz. *Phys. Rev. Lett.*, 65(2):137, 1990.

[79] V. Privman (editor). *Finite Size Scaling and Numerical Simulation of Statistical Systems*. World Scientific, New York, 1990.

[80] A. Watanabe, T. Iiyama, K. Kaneko, R. Radhakrishnan, and K. E. Gubbins. *J. Phys. Chem. B.*, 103(34):7061, 1999.

[81] R. Radhakrishnan, K.E. Gubbins, A. Watanabe, and K. Kaneko. *J. Chem. Phys.*, 111(19):9058, 1999.

[82] A. Watanabe and K. Kaneko. *Chem. Phys. Lett.*, 305:71, 1999.

[83] R. Radhakrishnan and K. E. Gubbins. Free-energy studies of freezing in slit pores: an order parameter approach using monte carlo simulation. *Mol. Phys.*, 96:1249–1267, 1999.

[84] C.L. Rhykerd, M. Schoen, D.J. Diestler, and J.H. Cushman. *Nature*, 330(3):461–463, 1987.

[85] L.S. Bartell and J. Chen. *J. Phys. Chem.*, 96:8801, 1992.

[86] W.L. Jorgensen and J. Tirado-Rives. *J. Am. Chem. Soc.*, 110(6):3469, 1988.

[87] A. Vishnyakov, E. M. Piotrovskaya, and E. N. Brodskaya. *Adsorption*, 4:207–224, 1998.

[88] T. Iiyama, K. Nishikawa, T. Otowa, and K. Kaneko. *J. Phys. Chem.*, 99:10075, 1995.

[89] T. Iiyama, K. Nishikawa, T. Suzuki, and K. Kaneko. *Chem. Phys. Letts.*, 274:152, 1997.

[90] J. E. Curry, F. Zhang, J. H. Cushman, M. Schoen, and D. J. Diestler. *J. Chem. Phys.*, 101:10824–10832, 1994.

[91] A. Chelkowski. *Dielectric Physics*. Elsevier, North-Holland Inc., New York, 1980.

[92] P. Debye. *Polar Molecules*. Chemical Catalog Co., New York, 1929.

[93] K.S. Cole and R.H. Cole. *J. Chem. Phys.*, 9:341, 1941.

[94] N.G. Parsonage and L.A.K. Staveley. *Disorder in Crystals, Int. Series of Monographs in Chemistry*. Claderon Press, Oxford, 1978.

[95] J.D.H. Donnay and H.M. Ondik. Crystal data determinative tables. *National Bureau of Standards*, Vol. 1, 3rd. Edn., 1978.

[96] H. Frölich. *Theory of Dielectrics*. Claderon Press, Oxford, 1949.

[97] J. Schüller, Yu.B. Mel'nichenko, R. Richert, and E.W. Fischer. *Phys. Rev. Lett.*, 73(16):2224, 1994.

[98] P. Pissis, A. Kyritsis, D. Daoukaki, B. Barut, R. Pelster, and G. Nimtz. *J. Phys.: Cond. Matter*, 10, 1998.

[99] G. Bánhegyi. *J. Coll. Int. Sci.*, 264, 1986.

[100] J. Schüller, R. Richert, and E.W. Fischer. *Phys. Rev. B*, 52(21):15232, 1995.

[101] M. Urbakh and J. Klafter. *J. Phys. Chem.*, 97, 1993.

[102] R. Radhakrishnan, K.E. Gubbins, M. Sliwinska-Bartkowiak, G. Dydziak, and R. Sikorski. *J. Chem. Phys.*, submitted, 2000.

[103] T.M. Reed and K.E. Gubbins. Applied statistical physics. 1973.

[104] J.O. Hirshfelder, C.F. Curtiss, and B. Bird. *Molecular theory of gases and liquids*.

[105] M. W. Maddox, J. P. Olivier, and K. E. Gubbins. Characterization of MCM-41 using molecular simulation: Heterogeneity effects. *Langmuir*, 13(6):1737–1745, 1997.

[106] K.K. Unger, G. Kreysa, and J.P. Baselt, editors. *Characterization of Porous Solids V*, Amsterdam, 1999. Elsevier.

[107] R. Radhakrishnan, K.E. Gubbins, and M. Sliwinska-Bartkowiak. *J. Chem. Phys.*, 112(21), 2000.

[108] H.D. Cochran S.T. Cui, P.T. Cummings. *Science*, submitted, 1999.

[109] D.O. Oxtoby. *Nature*, 347, 1990.

[110] C.F. Chou, A.J. Jin, S.W. Huang, and J.T. Ho. *Science*, 280, 1998.

[111] P. Bladon and D. Frenkel. *Phys. Rev. Lett.*, 74, 1995.

[112] R. Zangi and S.A. Rice. *Phys. Rev. E*, 58, 1998.

[113] B.K. Peterson and K.E. Gubbins. *Mol. Phys.*, 62, 1987.

[114] M. Sliwinska-Bartkowiak. Private communication. 2000.

[115] S. Takahara, M. Nakano, S. Kittaka, Y. Kurodo, T. Mori, and H. Hamano. *J. Phys. Chem. B*, 103:5814, 1999.

[116] K. Morishige and K. Kawano. *Dynamics in confinement, Workshop in Grenoble*, January, 2000.

[117] W.J. Haller. *J. Chem. Phys.*, 42:686, 1965.

[118] T.H. Elmer. Asm engineered materials handbook. page 427, Ohio, 1991. ASM: Materials Park.

[119] I. Nowak and M. Ziolek. page 161, Torun, 1998. Nicholas Copernicus University Press.

[120] B. K. Peterson and K. E. Gubbins. Phase transitions in a cylindrical pore: Grand canonical monte carlo, mean field theory and the kelvin equation. *Mol. Phys.*, 62(1):215–226, 1987.

[121] L. D. Gelb and K. E. Gubbins. *Langmuir*, 14:2097–2111, 1998.

[122] Landolt-Boltzstein Tables. 1960.

[123] B.I Halperin and D.R. Nelson. *Phys. Rev. Lett.*, 41, 1978.

[124] A.P. Young. *Phys Ṙev. B*, 19, 1979.

[125] X.S. Zhao, G.Q. Lu, A.K. Whittaker, G.J. Millar, and H.Y. Zhu. *J. Phys. Chem. B*, 101, 1997.

[126] J. Klafter and J.M. Drake. *Molecular Dynamics in Restricted Geometries.* John Wiley, New York, 1989.

[127] K. Morishige and K. Kawano. *J. Phys. Chem. B*, submitted, 2000.

[128] J.M. Kosterlitz and D.J. Thouless. *J. Phys. C,*, 6, 1973.

[129] R. Radhakrishnan, K. E. Gubbins, and M. Sliwinska-Bartkowiak. *Phys. Rev. Lett.*, 2000. submitted.

[130] D. Frenkel and J.P. McTague. *Ann. Rev. Phys. Chem.*, 31:491, 1980.

[131] K.T. Thomson and K.E. Gubbins. *Langmuir*, in press, 1999.

[132] D. W. Brown, P. E. Sokol, A. P. Clarke, M. A. Alam, and W. J. Nuttall. *J. Phys.: Condens. matter*, 9:7317–7325, 1997.

[133] M. Miyahara, H. Kanda, M. Shibao, and K. Higashitani. *J. Chem. Phys.*, 112(22):9909, 2000.

[134] D. K. Chokappa and P. Clancy. A computer simulation study of the melting and freezing properties of a system of lennard-jones particles ii. cooling the liquid. *Mol. Phys.*, 61(3):617, 1987.

[135] P. Pissis, D. Daoukaki-Diamanti, L. Apekis, and C. Christodoulides. The glass transition in confined fluids. *J. Phys. Cond. Mat.*, 6:L325, 1994.

[136] I.M. Svishchev and P.G. Kusalik. *Phys. Rev. Lett.*, 73:975, 1994.

[137] D.M. Ceperley and L. Mitas. *Adv. Chem. Phys.*, 93:1, 1996.

[138] R. Car and M. Parrinello. *Phys. Rev. Lett.*, 55:2471, 1985.